

UNIVERSITÀ DEGLI STUDI DI BOLOGNA

FACOLTÀ DI SCIENZE MATEMATICHE, FISICHE E NATURALI

Dottorato di Ricerca in Fisica: XX ciclo

Simulations and interpretation
of holographic TEM images
of biased and unbiased electronic devices

Tesi di Dottorato

Presentata da:

Dott. Filippo Ubaldi

Tutore:

Chiar.mo Prof. Giulio Pozzi

Coordinatore:

Chiar.mo Prof. Fabio Ortolani

Bologna, Marzo 2009

Contents

Introduction	5
1 Phase contrast techniques	7
1.0.1 Out of focus	7
1.0.2 Interferometry	9
1.0.3 Overview of the experimental images.	13
1.0.4 Electron Holography	17
1.1 Effects of spherical illumination	20
2 Two-dimensional models for reverse biased p-n junctions	25
2.0.1 Device used in experiments.	26
2.1 Numerical simulations of the Electrostatic Potential	27
2.1.1 PDE's discretization	28
2.1.2 Boundary conditions	29
2.1.3 Validation of the 2D numerical computations	30
2.1.4 Mathematica and the ISE-tCad	33
2.2 2D mixed numerical-analytical computations for the interpretation of the TEM images far from the edge.	33
2.2.1 Dopant implantation simulation	34
2.2.2 Potential and phase computation.	34
2.2.3 Experimental results	35
2.2.4 Interpretation of experimental images.	39
3 Three-Dimensional Field Models for Reverse Biased p-n Junctions.	47
3.1 Full three-dimensional model	48
3.1.1 Validation of the 3D numerical computations	49
3.2 The CPAC Model for the semiconductor junction	51
3.2.1 Further considerations on 3D simulations - CPAC versus full 3D	53
3.3 Interpretation of the Experimental results in out-of-focus and in- terferometry.	54
3.3.1 Out-of-focus	54
3.3.2 Interferometry	55

3.3.3	Holography	58
4	Electron Holography of a Metal-Oxide-Semiconductor specimen.	63
4.1	Specimen description and experimental results	63
4.2	Geometry and boundary conditions of the numerical model	65
4.3	Interpretation of the experimental images	65
4.3.1	Image simulations	67
5	3D field simulations of phase contrast images of field emitting	
CNTs.		71
5.1	Specimen description and experimental results	71
5.2	Linear charge analytical model	72
5.3	Numerical computation of the electrostatic potential	76
5.4	Charge density	77
5.5	Image simulations	78
5.5.1	Holography	78
5.5.2	Out-of-focus	81
Conclusions		83
A	Beam-specimen interaction	85
A.1	Phase object approximation	85
A.1.1	The Möllenstedt-Düker biprism	87
Acronyms		89
Bibliography		91

Introduction

The aim of this thesis is to discuss the interpretation of the transmission electron microscope (TEM) images of biased and unbiased electronic devices observed by means of holography, interferometry and out of focus techniques. The images used in the thesis have been mainly recorded at the IMM section of the CNR of Bologna by P. F. Fazzini, and at the Old Cavendish Laboratory by the HREM group of the University of Cambridge (R. E. Dunin-Borkowski, T. Kasama).

Our attention primarily focuses on electrostatic fields generated by charge distribution of specimens, that are related to their properties as doping concentration (pn-junctions), induced beam charging of oxides (P-N junction and metal-oxide-semiconductor MOS), and peculiar shapes (biased carbon-nanotube CNT). The TEM observation of electrostatic fields by means of phase contrast techniques allows us to retrieve information on the specimen by comparing experimental and simulated images.

Dopant profile investigation is an important issue for the semiconductor industry, as the spatial distribution and the concentration of the dopant atoms are key factors in understanding device operation and validating device simulations. The Semiconductor Industry Association SIA Roadmap and the International Technology Roadmap of Semiconductors ITRS presuppose to achieve nanoscale control of the distribution of dopants as device dimensions shrink beyond the 100 nm node. Consequently there is a pressing need for the development of a reliable, high spatial resolution technique that can be used to obtain quantitative information about dopant distributions in semiconductors, for both the evaluation of process parameters and to provide input to simulations of dopant diffusion. Off-axis electron holography and other phase contrast techniques in the TEM offer the potential to provide such information. It must be noticed that these techniques do not give information about the dopant concentration directly, but about the electrostatic field projected orthogonally to the electron beam direction. Thus the only way to obtain quantitative information about the doped specimen is to simulate numerically its electrical behavior, by using the equations of the semiconductors and reproducing its geometry. In this way it is possible to compute the phase by starting from semiconductor physics equations, so that the distribution of dopants can be deduced from the comparison between experimental and simulated images.

Electron Holography and other medium-low resolution phase contrast techniques as interferometry and out of focus, are able to provide information not only on pn-junctions, but on other kinds of specimens such as carbon nanotube bundles used as field emission tips under a suitable bias and MOS oxides.

- In chapter 1 the techniques used to obtain the images interpreted in this thesis will be discussed from the theoretical point of view. The derivation of the basic equations used for images simulations in out-of-focus, interferometry and holography will be given.
- In chapter 2 the two-dimensional (2D) simulations used for the interpretation of the TEM images of P-N junctions (power diodes) prepared and observed at the IMM in Bologna, will be presented.
- In chapter 3 the reasons that have brought about the development of Three-Dimensional models of electronic devices are explained, and the interpretation of interferometry and holography images of biased p-n junction by Three-Dimensional models is discussed. Particular attention will be paid to the development of a mixed analytical-numerical model that uses 2D numerical simulations to obtain 3D electrostatic potentials. Such a model saves considerable machine time and increases the precision, but its limits of validity require an assessment based on full 3D simulations.
- In chapter 4 electrostatic field 3D numerical computation, which is obtained thanks to the experience acquired on the full 3D model for p-n junctions, will be used to interpret holography images of a MOS. This is a very interesting specimen because of the richness of its images that carry unmistakable information about the amount of the charging of the oxide under the action of the electron beam.
- In chapter 5 the full 3D model will be adapted to carbon nanotube geometries. The computed electrostatic potential will be used for holography and out-of-focus image simulations in order to study the free charge distribution and the electrostatic field topography, which is useful to understand the field emission effect conditions.

1. Phase contrast techniques

At the mesoscopic scale, in the phase object approximation (POA) (Eq. A.12), in focus images provide no information, as the transmission function of the specimen is modeled by a pure imaginary quantity, whose square modulus gives a constant intensity image. A conventional in-focus image shows no contrast, except for extinction contours due to the Bragg diffraction, and other phenomena due to impurities (Fig.1.6). Moreover, the intensity transmitted by the specimen is lower than 1, i.e. the intensity transmitted in the vacuum, since electrons can either be stopped by the thicker specimen regions or scattered at large angles and subsequently intercepted by the microscope apertures. However, at the mesoscopic scale, amplitude contrast does not carry useful information: phase recovery is necessary to obtain electrical information, as the phase shift in the wave front is produced by the electric field generated by the charge distribution. Such a charge distribution depends on the structure and properties of the specimen we are interested in. (see appendix A.1).

It is then necessary to produce in the image a contrast, which is dependent on the phase. Such a contrast will be characterized by interference and diffraction phenomena, which are due to the wave behavior of the electron beam. The first phase contrast techniques, as holography, were originally developed in Light Optics. Nowadays Electron Microscopy uses phase-contrast techniques that directly stem from optical ones. Three of these techniques, out-of-focus, interferometry, and holography will be widely modeled in this thesis to interpret the experimental images.

1.0.1 Out of focus

The simplest technique to obtain phase information on electric fields of a specimen at the mesoscopic scale, in the range of the POA approximation, is to take an out of focus image. In fact, since the specimen is uniformly transparent, in focus observations give uniform contrast, but if electrons are deflected by an electric field of the specimen, that is not uniform, the intensity distribution will not be uniform after the specimen. A contrasted image is obtained even if an object plane before the specimen is chosen, due to the virtual prolongation of the wave front. In this case the contrast will be opposite compared to the former case (Fig 1.1).

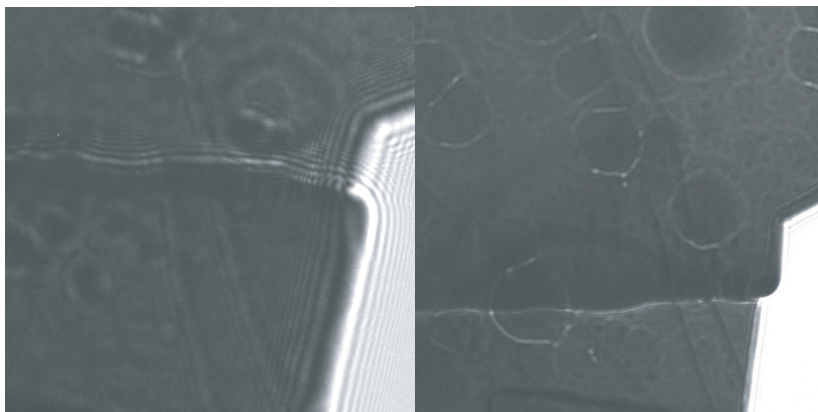


Fig. 1.1. Two images of the same junction recorded at the IMM of Bologna by P. F. Fazzini with opposite sign out-of-focus distance. The trend of the Fresnel fringes and the edge deformation result inverted when passing from over to under focus and vice-versa. Out-of-focus observations have been used by the microscopy group of the University of Bologna to distinguish two different models for P-N junctions that give qualitatively different predictions over a range of defocuses and reverse biases [1].

Let us consider the phase-object approximation (eq. A.11). If the Kirchhoff-Fresnel (K-F) propagator [2] is applied to the outgoing wave, the wave function for any (arbitrary) z (note: also for $z < z_o$, i.e. in the case of over focus observations)

$$\psi(\mathbf{r}, z) = \frac{1}{i\lambda z} \int_{\mathbf{R}^2} e^{i\phi(\mathbf{r})} \cdot e^{\frac{i\pi}{\lambda z}(\mathbf{r}-\mathbf{r}_o)^2} d\mathbf{r}_o \quad (1.1)$$

Since Eq. 1.1 is a convolution product between a complex exponential function and a Gaussian-Fresnel function, it can be conveniently treated in Fourier space:

$$\begin{aligned} F.T.[\Psi(\mathbf{r}, z)](\mathbf{k}) &= F.T. \left[\frac{1}{i\lambda z} \int_{\mathbf{R}^2} e^{i\phi(\mathbf{r})} \cdot e^{\frac{i\pi}{\lambda z}(\mathbf{r}-\mathbf{r}_o)^2} d\mathbf{r}_o \right] (\mathbf{k}) \\ &= F.T. [e^{i\phi(\mathbf{r})}] (\mathbf{k}) \cdot F.T. \left[\frac{1}{i\lambda z} e^{\frac{i\pi}{\lambda z}(\mathbf{r})^2} \right] (\mathbf{k}) \\ &= F.T. [e^{i\phi(\mathbf{r})}] (\mathbf{k}) \cdot e^{-i\pi\lambda z k^2}. \end{aligned} \quad (1.2)$$

Returning to the real space, the following expression for the defocused wave is obtained:

$$\Psi(\mathbf{r}, z) = \int_{\mathbf{R}^2} F.T. [e^{i\phi(\mathbf{r})}] (\mathbf{k}) \cdot e^{-i\pi\lambda z k^2} e^{2\pi i \mathbf{k} \cdot \mathbf{r}} d\mathbf{k} \quad (1.3)$$

where z is the distance from the object plane. When $z = 0$ the specimen is in focus. Finally, it must be noticed that (Eq. 1.3) can be rewritten as

$$\Psi(\mathbf{r}, z) = F.T.^{-1} \left[F.T. [e^{i\phi(\mathbf{r})}] (\mathbf{k}) \cdot e^{-i\pi\lambda z k^2} \right]. \quad (1.4)$$

Such a formulation may seem quite complicated, but it is useful from the numerical computation point of view, as the discrete Fast Fourier Transform (FFT) algorithm is more efficient than the real space computation of the Fr enel integral (1.1).

The defocus values z indicated by modern instruments, which are optimized for high resolution set-up, are not reliable in the non-standard conditions useful for out-of-focus observations. An independent calibration is necessary [3] to find the effective value for z , in order to achieve the agreement between image simulations and experimental findings.

1.0.2 Interferometry

Interference electron microscopy observations of one-dimensional phase-objects like magnetic domain walls [4, 5, 6] and reverse biased pn junctions [7], [8] show that electron interferometry can be used to gather reliable information from the analysis of interferograms. In this particular and interesting case, the phase difference between interfering points is directly displayed in the profile of the fringes [9], making their interpretation easier and more quantitative than that obtainable from classical Lorentz microscopy observations, as for example from out-of-focus techniques (sec.1.0.1). The subject of this section is mainly the wave-optical analysis of the image formation in the interference mode, which is applicable not only to one-dimensional phase-objects, but also to any kind of phase-objects, in particular to P-N junctions when an edge is present (sec. 1.0.3). For the sake of simplicity, the treatment is developed assuming plane wave illumination, which is the hypothesis usually adopted in Electron Microscopy. However a treatment which includes the spherical illumination is essential in order to obtain the correct values for the experimental parameters. It will be developed in section 1.1.

In figure (1.2), the basic elements of a TEM set up for interferometry observations are outlined. The electronic wave transmitted by the specimen is focused by the lens Ob , impinges on a M ollenstedt-D uker biprism, whose task is to split the wavefront in two parts making them interfere through partial superimposition. The interferogram, which forms on the image plane IP , is magnified on the conjugate recording plane RP by the projection system PS .

The wave function image perturbed by the biprism can be calculated, using the paraxial theory developed by Glaser [10], in two steps: propagation from the specimen to the biprism, multiplication by the transmission function of the biprism and propagation from the biprism plane to the image plane.

$$z_o \rightarrow z_b; T_b; z_b \rightarrow z_i \quad (1.5)$$

where $z_o \rightarrow z_b$ and $z_b \rightarrow z_i$ refer to the K-F propagation [2] of the wave function from the object plane to the biprism plane, T_b indicates the multiplication by the biprism transmission function (sec.A.1), and $z_b \rightarrow z_i$ the wave propagation from the biprism to the image plane. However, according to the principle of optical reversibility [11], it is perfectly equivalent to follow a different procedure

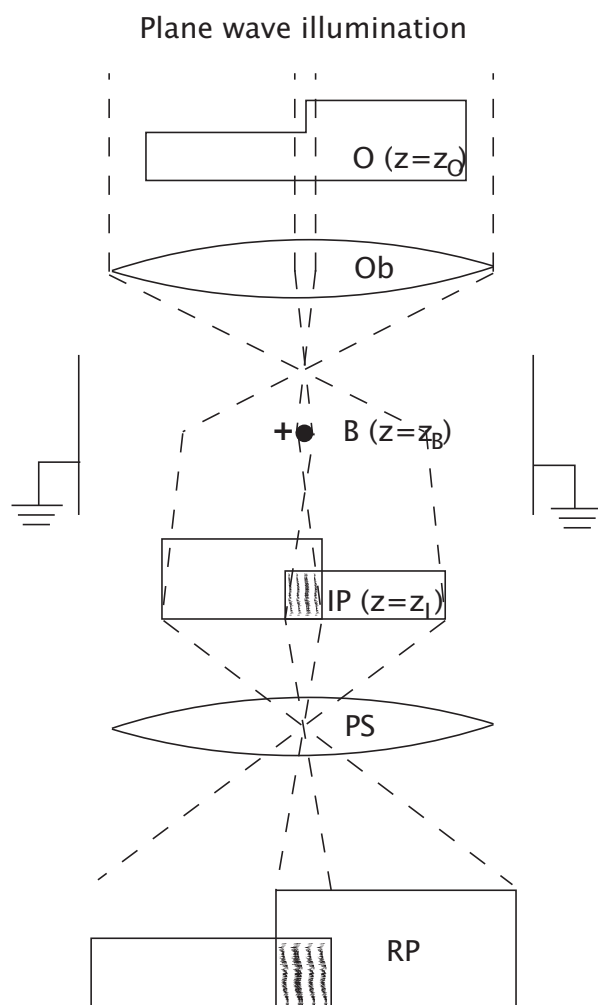


Fig. 1.2. Geometric optical set-up of Interference electron microscopy: plane-wave illumination. O , specimen; Ob , objective lens; B , wire of the Möllenstedt-Düker biprism; IP , image plane; PS , projector system; RP , recording plane.

[12] (which highlights the perturbation effect of the biprism in relation to the unperturbed wave):

$$z_o \rightarrow z_i; \quad z_i \rightarrow z_b; \quad T_b; \quad z_b \rightarrow z_i \quad (1.6)$$

Where the first implication ($z_o \rightarrow z_i$) can be omitted as it is the propagation between conjugate planes without biprism, and its only effect is the scaling of the image. Again, since the image and object plane are conjugate, for our simulations, we can use for simulations, instead of the scheme (Eq. 1.6), the following

$$z_o \rightarrow z_b; \quad T_b; \quad z_b \rightarrow z_o \quad (1.7)$$

where z_i has been replaced with z_o , meaning that we are referring our set-up to the object space. This treatment, which leads to equation 1.7 starting from equation 1.5, presupposes an ideal behaviour of lenses, that allows conjugate planes to be considered interchangeable. In fact, in interferometry as in out-of-focus, aberrations are usually neglected because of the low-magnification conditions (the objective lens is usually switched off).

In any case, the procedure (1.7) (or equivalently the procedure (1.5)) allows us to calculate the wave function on the image plane. It is necessary however to have expressions for the transmission function of the biprism. For this purpose the equation (A.16) is used. The electrostatic potential generated by the specimen is provided by numerical simulations (chapter 2, 3), and its contribution to the phase $\phi(\mathbf{r}_o)$ for equation 1.8 is given by Eq. A.12. Finally, the simulated intensity for the image plane is given by the square modulus of the wave function, calculated in order to compare it with the experimental results.

It is convenient, as in the case of the out-of-focus images, to make computations in the Fourier's space, where the formula used for numerical image simulations is as follows:

$$\begin{aligned} \Psi(\mathbf{r}_o, z_o) &= \\ &= \mathcal{F}^{-1} \left[\mathcal{F} \left[\mathcal{F}^{-1} \left[\mathcal{F} \left[e^{i\phi(\mathbf{r}_o)} \right] (\mathbf{k}_b) e^{i\pi\lambda(z_b-z_o)k_b^2} \right] T_b(\mathbf{r}_b) \right] (\mathbf{k}_o) e^{i\pi\lambda(z_o-z_b)k_o^2} \right] (\mathbf{r}_o). \end{aligned} \quad (1.8)$$

where the subscripts o and b refer to the object plane and to the biprism plane respectively. The K-F propagation from the object to the biprism plane is computed by means of two Fourier transforms, according to the equation 1.4. Then, the wave is multiplied by the transmission function of the biprism (Eq. A.16). Finally, the K-F back propagation to the object plane (equivalent to its conjugate, the image plane) is performed by other two Fourier transforms.

It is here pointed out again that the Eq. 1.8 is derived by adopting the assumption of plane-wave illumination. Such an assumption is usual in Electron Microscopy, but a derivation that takes into account the spherical-wave illumination is necessary to obtain the correct values to insert in simulations. It turns out that the spherical illuminating wave set-up can be reduced to the plane wave case by suitable scaling (sec. 1.1), so that Eq. 1.8 can be kept provided that the various parameters are substituted by their effective values.

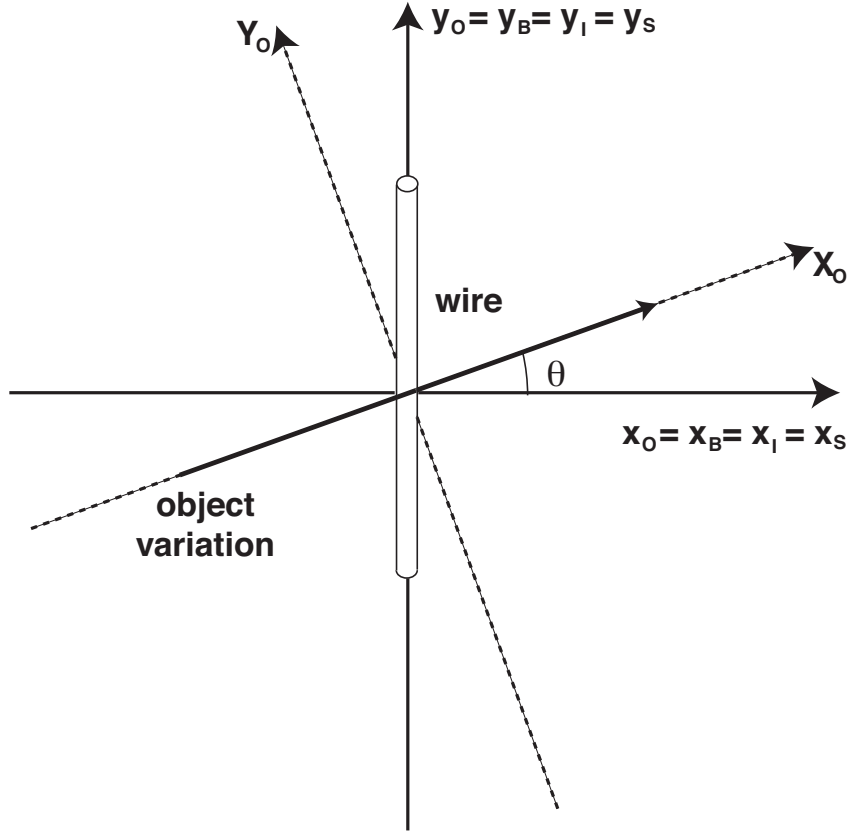


Fig. 1.3. Schematic set-up of the reference systems used in calculations. (x_O, y_O) and (X_O, Y_O) are the coordinates of the biprism and the phase object respectively. θ is the angle between the two systems.

1.0.2.1 Geometric optical interpretation for one-dimensional electron-optical phase objects

Electron interferometry of one-dimensional phase-objects is a particular and interesting case, where the phase difference between interfering points is directly displayed in the profile of the fringes. Figure 1.3 shows the set-up of the reference system of the phase-object with respect to the biprism.

Provided the geometric optical equations are valid, the interpretation requires only a one-dimensional best fit between experimental fringe profiles and calculated ones. The following equation, calculated by means of an asymptotic approximation [12, 13] gives the parametric equation of the interference fringe of order n , $n = 0, n = \pm 1, n = \pm 2 \dots$ [9], which is expressed in the object coordinate system (X_O, Y_O) :

$$Y_O(X_O) = \frac{n\lambda}{2\alpha \sin \theta} + X_O \cot \theta + \frac{\lambda}{4\pi\alpha \sin \theta} [\Phi(X_O + z\alpha \cos \theta) - \Phi(X_O - z\alpha \cos \theta)] \quad (1.9)$$

This equation displays the phase difference between the points brought to interfere by the electron biprism. α , the deflection angle of the electron beam due to the biprism, must be corrected to the value $\alpha\gamma$ to take into account the effect of spherical illumination (section 1.1). θ is the angle between the direction of the phase-object variation and the direction of the biprism phase variation.

In addition, inasmuch as interferometric experiments are carried out with a narrow interference field and relatively low number of fringes, it turns out that also the shadow effects on the biprism edges, which is linked to the derivative of the phase shift, are playing a relevant role. Again by means of the asymptotic approximation [12], the parametric equation for the left shadow edge [9] is obtained. It results

$$Y_O(X_O) = (X_O + z\alpha \cos \theta) \cot \theta + \frac{R}{\sin \theta} + \frac{\lambda z}{2\pi} \quad (1.10)$$

$$\frac{d\Phi}{dX_O}(X_O + z\alpha \cos \theta) \cot \theta + z\alpha \sin \theta$$

which clearly shows the direct dependence of the profile of the edge on the first derivative of the phase. In equation 1.11, R is the radius of the biprism wire, α is the deflection angle of the electron beam due to the biprism, and z is the distance between the object and the biprism. (These values must be replaced by their effective values to take into account the effect of spherical illumination (section 1.1).)

Eq. 1.10 and eq. 1.11 can be used to compare the results of the geometrical vs. the wave-optical analysis (sec.1.0.2), in order to assess the range of validity of the geometric optical approximation. It turns out that such an approximation is not always in agreement with the full two-dimensional wave optical model. The reasons for this discrepancy have not been thoroughly investigated, although it can be surmised that when the object dimensions are of the order of or below the Fresnel diffraction length (roughly given by width of the first Fresnel diffraction fringe) the edge diffraction waves have a stronger influence on the image (Fig. 1.4). The geometric optical equation is valid for a p-n junction with a depletion layer width $d = 0.1\mu m$, but it is not valid for a depletion layer width of $d = 0.05\mu m$ (Fig. 1.4). The contribution to the phase of the depletion layer (inner field) and of the fringing field can be ascertained by comparison between simulation and experiment.

1.0.3 Overview of the experimental images.

In this section an overview of interferometric and out-of-focus experimental images of a straight p-n junction in the presence of an edge is considered. These results, where the junction is nearly orthogonal to the edge and the biprism crosses the junction with a tilt angle of 45° , will be interpreted in the following two chapters.

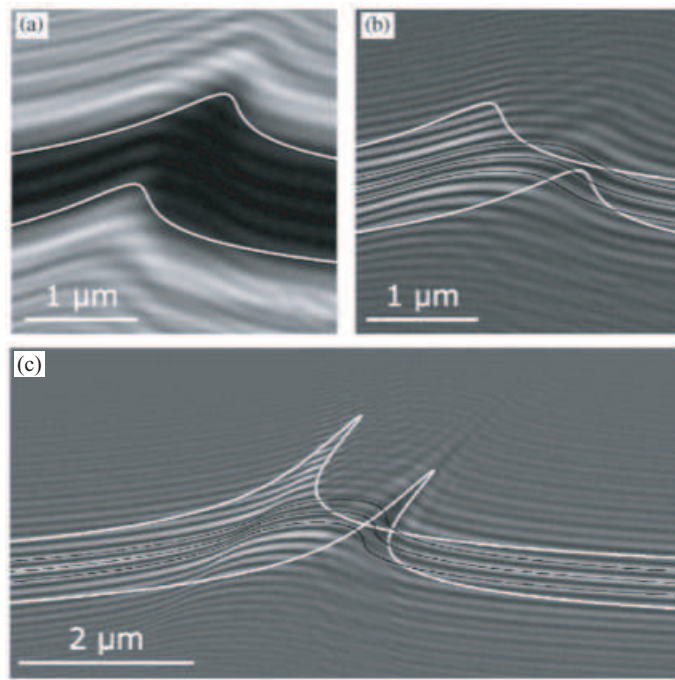


Fig. 1.4. Image simulations using the Spivak model [14] for the electrostatic potential. (a,b) Close ups of the junction regions of with superimposed geometrica-optical profiles. In (a) the biprism deflection angle is $a_{eff} = 0$ rad, while in (b) is $a_{eff} = -1 \times 10^{-5}$ rad. The white lines represent the biprism edges in geometric-optic approximation, while the thin lines in image (b) are the interference fringes of order $k = 0, \pm 1$. (c) Wave-optical simulation with superimposed geometric-optical profiles of an interference image of a pn junction calculated for the same conditions of (a) and (b), but with a depletion layer half-width $d = 0.05 \mu m$. In this second case the geometric-optical approximation is no more valid as across the junction the parametric fringes do not follow the numerical ones.

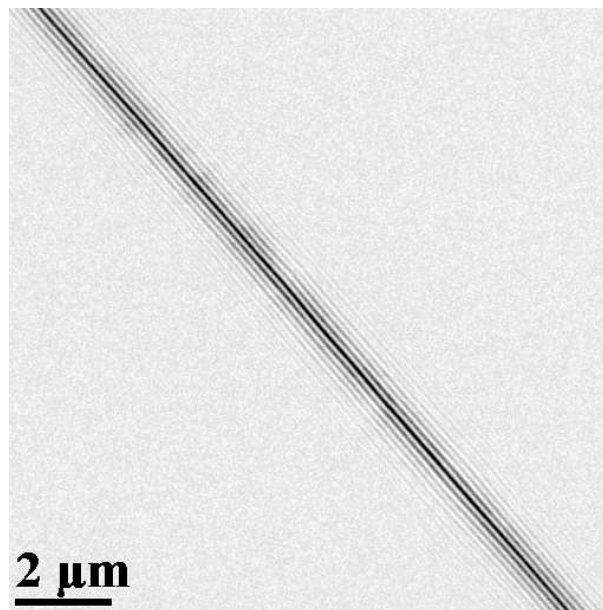


Fig. 1.5. Image of the $V_b = 5V$ biased biprism. The contrast has been inverted for a better visualization.

In the absence of specimen, the fringes produced by the biprism run parallel to the biprism itself. It is possible to vary the fringe spacing and the extent of the interference field by varying the potential applied to the wire. Figure (1.5) shows such a fringe pattern for a $5V$ potential applied between the wire and the conducting plates kept at ground potential, i.e. equipotential with the TEM column.

When the specimen is superimposed on the fringe system, the image shown in figure (1.6) is obtained: because of the superimposition between the object semi-planes on the left and on the right of the wire caused by a translation, perpendicular to the axis due to the potential applied to the wire, the edge which was originally straight (see also following figure (1.7)) is broken at the interference field (arrow (a)). The fringes that were originally straight are deformed both entering and inside the specimen: in particular the change in direction (deflection) reaches its maximum at the junction, indicated with the letter (b).

When the specimen is in-focus the junction is not identifiable. In order to identify it, it is necessary to put it slightly out-of-focus allowing the creation of a thin contrast line at the junction position itself as shown in figure (1.7) by the arrows (g), where the shadow of the wire of the biprism B kept at potential zero is visible. The other contrast phenomena are extinction contours and impurities resulting from the thinning process.

The out-of-focus contrast effect identified in figure (1.7) and its association with the junction can be amplified by the increase of the reverse bias and the defocalization distance as shown in figure (1.8) where the thin black and white

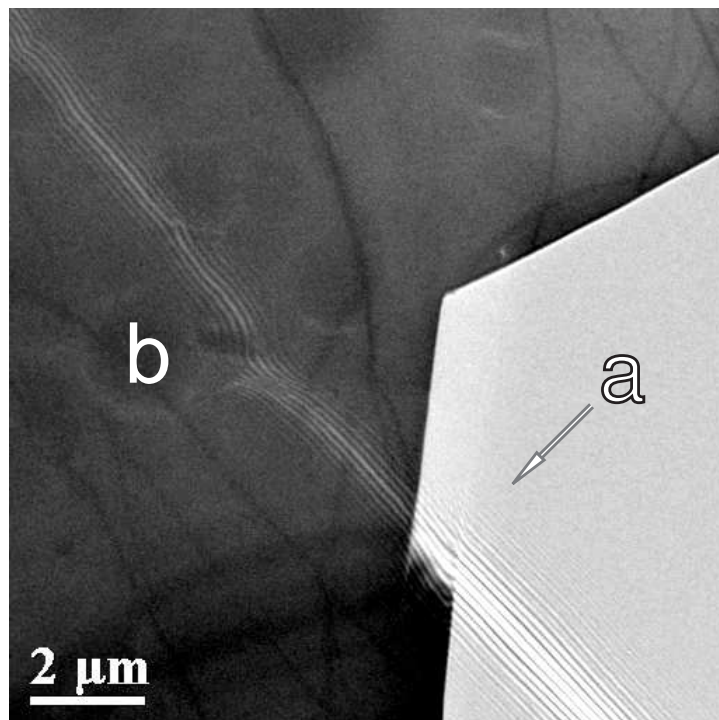


Fig. 1.6. Large field image of the junction in interferometry: $V_b = 5V$, $V_{bias} = (3 \pm 0.1)V$

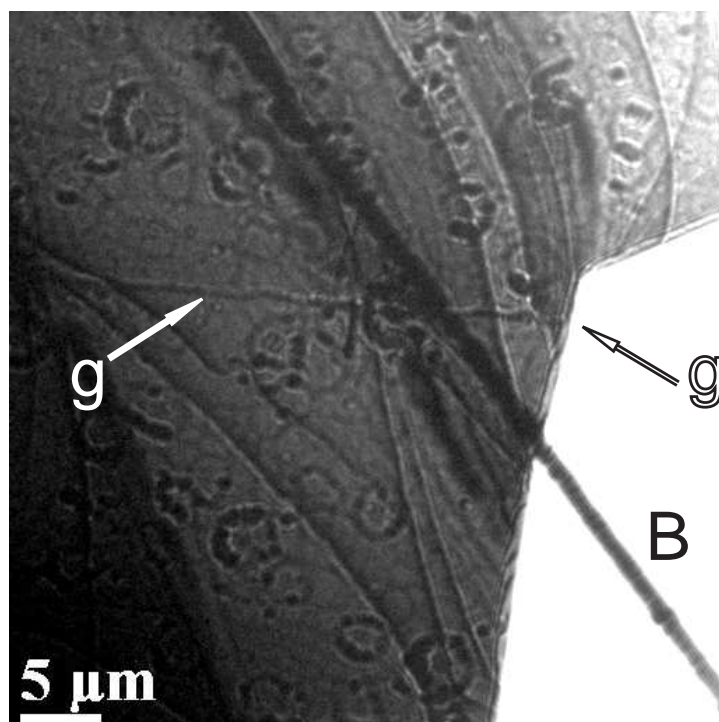


Fig. 1.7. Large field image of the junction in interferometry: $V_b = 0V$, $V_{bias} = 0V$

line has changed its structure showing a system of fringes due to the diffraction of electrons caused by the electrostatic field associated with it.

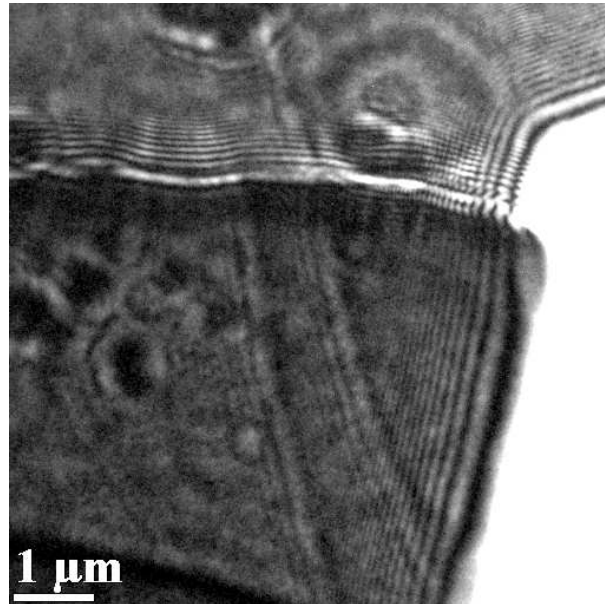


Fig. 1.8. Out-of-focus image of the junction at the edge: $\Delta z = (40 \pm 2)mm$, $V_{bias} = (5.0 \pm 0.1)V$

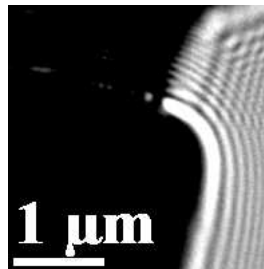


Fig. 1.9. Out-of-focus image of the edge: $\Delta z = (40 \pm 2)mm$, $V_{bias} = (5.0 \pm 0.1)V$

Another interesting feature from the electro-optical point of view is the distortion of the edge of the specimen (shadow edge effect), which is more evident in the following image (fig. 1.9) which is actually the previous image reproduced with a different contrast. Image simulations concerning this feature are shown in chapter 3, where the 3D model is discussed.

1.0.4 Electron Holography

Electron holography [15] was invented by Gabor during a research intended to improve resolution by correcting the spherical aberration of the transmission

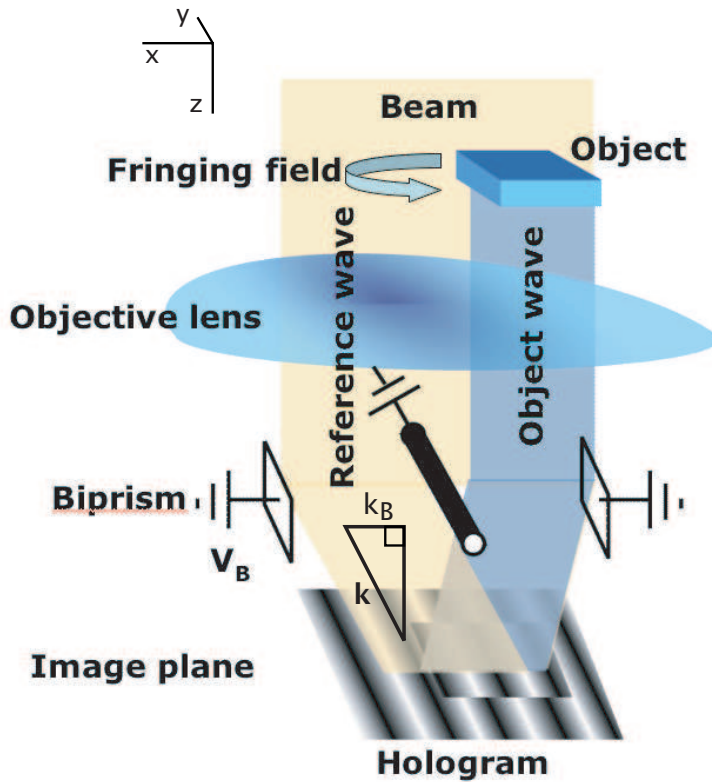


Fig. 1.10. “Off-axis” electron holography setup. The reference wave, that may be perturbed by the fringing field of the object, is brought to interfere with the object wave. At the image plane the hologram is recorded. The carrier frequency is the x projection of the momentum of the electron beam deflected by the biprism.

electron microscope. This method is able to extract both amplitude and phase of the object wave-function, thus recovering all the information from the elastic interaction between the electron beam and the specimen. This task is performed by superimposing the object wave-function, emerging from the sample, with a reference wave, coherent with the former, usually assumed not to be perturbed by the fringing field generated by the sample itself. The phase shift can finally be recovered from the obtained image, called hologram, by optical or numerical reconstruction.

In the original configuration proposed by Gabor, where the unscattered wave-front is used as reference wave (“in line” holography), serious limitations in phase recovery are represented by the generation of twin images [2].

Nowadays, the set-up most widely used in electron microscopy is off-axis electron holography, which takes advantage of a Möllenstedt-Düker electron biprism (sec. A.1.1) to split the electron beam (Fig. 1.10). The part of the electron wave chosen as the reference wave is not transmitted by the specimen, but travels in the vacuum so that the twin image problem is not present. Since the biprism produces a deflection of the form $\arccos(\frac{k_B}{k})$ on the electron beam of momentum \mathbf{k} , the hologram intensity recorded in the image plane is:

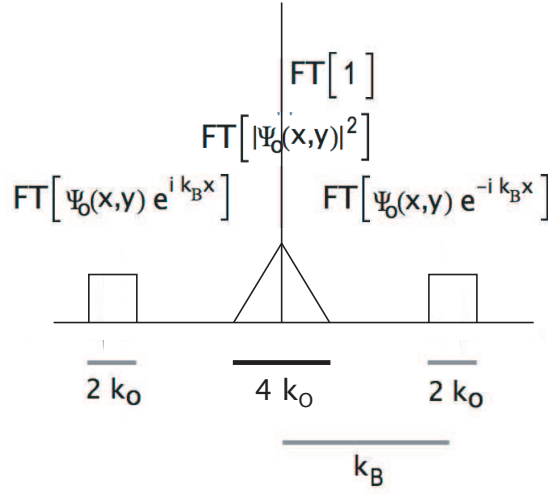


Fig. 1.11. Spectrum of the hologram. If the carrier frequency k_B is sufficiently larger than the half frequency domain k_o of the object wave, the Fourier Transform of the object wave is separated from other contributions and the phase recovering is possible.

$$\begin{aligned}
 I_H(x, y) &= |\Psi_o(x, y) + e^{ik_Bx}|^2 = \\
 &= 1 + e^{-ik_Bx}\Psi_o(x, y) + e^{ik_Bx}\Psi_o^*(x, y) + |\Psi_o(x, y)|^2. \quad (1.11)
 \end{aligned}$$

The Fourier Transform of the hologram (which is computed numerically by software that works on line during image recording) is used to recover the phase of the object wave. In fact, if the carrier frequency k_B is sufficiently larger than the spatial frequency range $2k_o$ of the object wave, the contribution of the object wave (apart from a multiplicative plane wave e^{ik_Bx}) to the hologram Fourier Transform is separated from the other contributions (Fig. 1.11).

Hence the next step of phase recovery is performed by operating the Inverse Fourier Transform of such a contribution. The function $\Psi_o(x, y)e^{ik_Bx}$ obtained, must be further manipulated as shown in equation 1.12. When on-line software manipulation of recorded images was not yet possible, this task was performed in an optical bench by illuminating the part of the hologram containing the object wave with a plane wave with a transverse frequency k_{opt} . The obtained image shows the intensity

$$I_R(x, y) = |e^{ik_Bx}\Psi_o(x, y) + e^{ik_{opt}x}|^2, \quad (1.12)$$

that, if $k_{opt} = k_B$ is chosen, i.e. in contour map condition, becomes

$$I_R(x, y) = |1 + \Psi_o(x, y)|^2. \quad (1.13)$$

If the phase object approximation is adopted, $\Psi_o(x, y) = e^{i\phi_o(x, y)}$, then we have

$$I_R(x, y) = |1 + e^{i\phi_o(x, y)}|^2 = 2 + 2 \cos(\phi_o(x, y)), \quad (1.14)$$

and the object phase is thus recovered as a cosine argument.

If the perturbation $\Pi(x, y)$ in the phase of the reference wave by the fringing field is considered, the hologram intensity (Eq. 1.11) becomes

$$\begin{aligned} I_H(x, y) &= |\Psi_o(x, y) + e^{i(k_B x + \Pi(x, y))}|^2 = |e^{i\phi_o(x, y)} + e^{i(k_B x + \Pi(x, y))}|^2 = \\ &= |e^{i(\phi_o(x, y) - \Pi(x, y))} + e^{ik_B x}|^2 \end{aligned} \quad (1.15)$$

and the contour map reconstruction leads to the expression:

$$I_R(x, y) = 2 + 2 \cos[\phi_o(x, y) - \Pi(x, y)], \quad (1.16)$$

so that the quantity useful for simulations is the difference between the object phase and the phase perturbation of the reference wave, i.e. the contribution $\Pi(x, y)$ of the fringing field to the phase shift in the vacuum besides the specimen.

1.1 Effects of spherical illumination

It is essential to know the defocus distance for the out-of-focus method, as well as the effective distance between the object and the biprism for the interferometry, in order to obtain reliable simulations of the image that can be compared to the experimental findings. Unfortunately, in the non-standard conditions useful for interferometry and out-of-focus, the defocus values indicated by modern instruments, optimized for the needs of high resolution, are not reliable. Thus an independent calibration is necessary [3]. Several methods, for instance low-angle electron diffraction [16], diffractogram [17] and edge diffraction fringe analysis [18], can be used to accomplish this task.

Moreover, the effects of a spherical illumination are not negligible, resulting in a substantial disagreement with theoretical predictions made in the illuminating plane wave approximation.

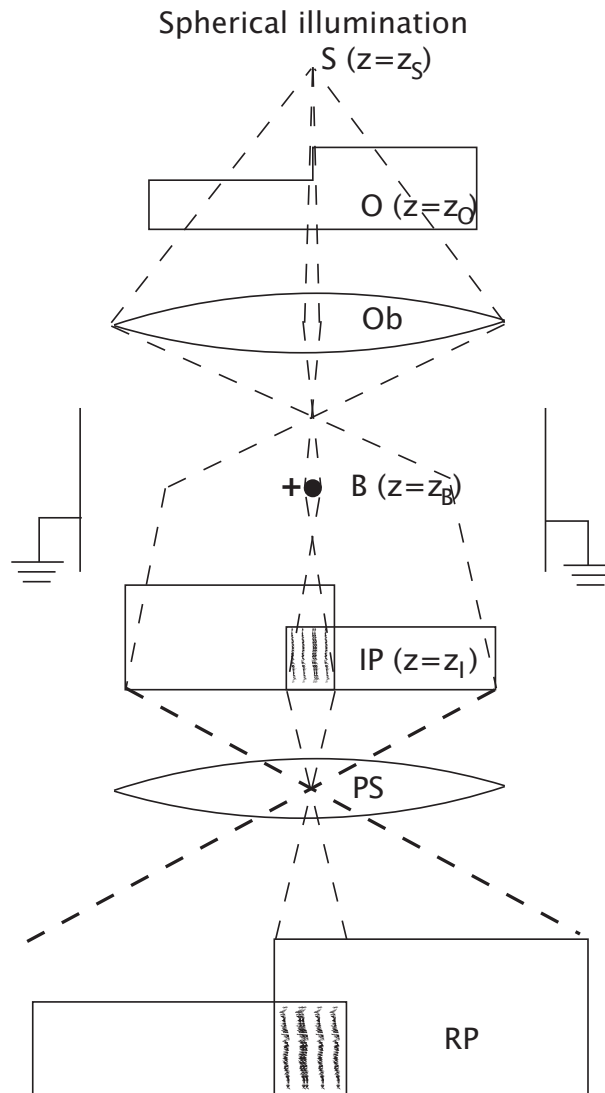


Fig. 1.12. Interference electron microscopy set-up: spherical illumination.

Let us consider the schematic set-up for interference electron microscopy sketched in Figure 1.12. As before, the z axis of a Cartesian coordinate system is directed along the optical axis of an electron microscope and in the same direction as the electron beam, i.e. downwards. The position of the various planes perpendicular to z are indicated by a pedix, which is also used to characterize the two-dimensional coordinates $\mathbf{r} = (x, y)$ in the corresponding planes.

Let us start with the electron source, located in the origin of the source plane S at $z = z_s$, which is assumed to be an ideal point source illuminating the object plane O , at $z = z_o$, with a spherical wave centered on the axis. The specimen, inserted at the object plane, is characterized by a complex transmission function $T(\mathbf{r}_o)$, so that the wave-function transmitted by the object A.10 becomes:

$$\psi_o(\mathbf{r}_o, z_o) = \psi_{ill}(\mathbf{r}_o, z_o)T(\mathbf{r}_o) = \exp \left[i\frac{\pi}{\lambda} \frac{\mathbf{r}_o^2}{(z_o - z_s)} \right] T(\mathbf{r}_o) \quad (1.17)$$

where λ is the de Broglie electron wavelength, and the pedix O indicates the object plane.

The electron interferometer, a Möllenstedt-Düker electron biprism [19], is inserted at the selected area plane, which we will call the biprism plane z_b . The objective lens is switched off, the diffraction or intermediate lens, included in the projector lens system PS , acts as imaging lens and is used to focus the specimen plane in the recording plane RP .

The propagation between the object plane and the biprism plane can therefore be considered to take place in the field free space and the wave-function impinging at the biprism plane B at $z = z_b$ can be calculated in the paraxial approximation by means of the Kirchhoff-Fresnel's diffraction integral [11] between the planes z_o and z_b :

$$\psi_b(\mathbf{r}_b, z_b) = \frac{1}{i\lambda(z_b - z_o)} \int \psi_o(\mathbf{r}_o, z_o) e^{i\frac{\pi}{\lambda} \frac{(\mathbf{r}_b - \mathbf{r}_o)^2}{(z_b - z_o)}} d\mathbf{r}_o \quad (1.18)$$

By inserting equation (1.17), equation (1.18) can be rewritten as :

$$\psi_b(\mathbf{r}_b, z_b) = \frac{e^{i\frac{\pi}{\lambda} \frac{\mathbf{r}_b^2}{(z_b - z_o)}}}{i\lambda(z_b - z_o)} \int T(\mathbf{r}_o) e^{i\frac{\pi}{\lambda} \left[\frac{\mathbf{r}_o^2}{z_{eff}} - 2\frac{\mathbf{r}_b \cdot \mathbf{r}_o}{(z_b - z_o)} \right]} d\mathbf{r}_o \quad (1.19)$$

where z_{eff} is given by

$$\frac{1}{z_{eff}} = \frac{1}{z_b - z_o} + \frac{1}{z_o - z_s} \quad (1.20)$$

The wave-function after interaction with the biprism is given by:

$$T_b(\mathbf{r}_b)\psi_b(\mathbf{r}_b, z_b) \quad (1.21)$$

where T_b is given by Eq. A.16. The propagation from the biprism plane to the final recording plane can be carried out by applying the Glaser-Schiske integral and taking into account the microscope lenses [20]. However, referring all quantities to the object space, where the image plane I is conjugate to the final recording plane RP , it can be ascertained that the whole process is equivalent to the field-free propagation from the biprism plane z_b to the image plane I , having coordinate z_i .

Again using the Kirchhoff-Fresnel diffraction integral between the planes z_b and z_i , and taking into account that when the specimen is in focus the object plane O and the image plane I are the same, $z_i = z_o$, the equation is:

$$\begin{aligned} \psi_i(\mathbf{r}_i) = & \frac{e^{i\frac{\pi}{\lambda} \frac{\mathbf{r}_i^2}{(z_o - z_b)}}}{\lambda^2(z_b - z_o)^2} \int T_b(\mathbf{r}_b) e^{-\frac{2i\pi}{\lambda} \frac{\mathbf{r}_b \cdot \mathbf{r}_i}{(z_o - z_b)}} \cdot \\ & \cdot \left(\int T(\mathbf{r}_o) e^{i\frac{\pi}{\lambda} \left[\frac{\mathbf{r}_o^2}{z_{eff}} - 2\frac{\mathbf{r}_b \cdot \mathbf{r}_o}{(z_b - z_o)} \right]} d\mathbf{r}_o \right) d\mathbf{r}_b \end{aligned} \quad (1.22)$$

By introducing the projection factor γ defined as

$$\gamma = \frac{z_b - z_o}{z_{eff}} = \frac{z_b - z_s}{z_o - z_s} \quad (1.23)$$

and the new “dummy” variable

$$\mathbf{r}'_b = \frac{\mathbf{r}_b}{\gamma} \quad (1.24)$$

equation (1.22) can finally be written as:

$$\begin{aligned} \psi_i(\mathbf{r}_i) = & \frac{e^{-\frac{i\pi}{\lambda} \frac{\mathbf{r}_i^2}{\gamma z_{eff}}}}{\lambda^2 z_{eff}^2} \int T_b(\gamma \mathbf{r}'_b) e^{\frac{2i\pi}{\lambda} \frac{\mathbf{r}'_b \cdot \mathbf{r}_i}{z_{eff}}} \cdot \\ & \cdot \left(\int T(\mathbf{r}_o) e^{\frac{i\pi}{\lambda z_{eff}} (\mathbf{r}_o^2 - 2\mathbf{r}'_b \cdot \mathbf{r}_o)} d\mathbf{r}_o \right) d\mathbf{r}'_b \end{aligned} \quad (1.25)$$

By rearranging the exponents, eq.(1.25) can be recast in the form:

$$\begin{aligned} \psi_i(\mathbf{r}_i) = & \frac{e^{\frac{i\pi}{\lambda} \frac{\mathbf{r}_i^2}{z_o - z_s}}}{\lambda^2 z_{eff}^2} \int T_b(\gamma \mathbf{r}'_b) e^{-\frac{i\pi}{\lambda z_{eff}} (\mathbf{r}_i - \mathbf{r}'_b)^2} \cdot \\ & \cdot \left(\int T(\mathbf{r}_o) e^{\frac{i\pi}{\lambda z_{eff}} (\mathbf{r}_o - \mathbf{r}'_b)^2} d\mathbf{r}_o \right) d\mathbf{r}'_b \end{aligned} \quad (1.26)$$

in which the forward and backward propagators are explicitly shown.

The above equation clearly displays the scaling relation between spherical and plane illumination which can be obtained from the former in the limit $z_s \rightarrow \infty$, where $\gamma \rightarrow 1$, $z_{eff} \rightarrow z_b - z_o$ and $\mathbf{r}'_b \rightarrow \mathbf{r}_b$. Therefore the case of spherical illumination is identical to that of a plane wave impinging on a specimen at a distance z_{eff} , having radius $R_{eff} = R_b/\gamma$ and a deflection $\alpha_{eff} = \alpha_b \gamma$.

Since the FFT algorithm is numerically more efficient than the Frênel integral, it is convenient to treat the equation 1.26 in the Fourier space. It can be done by following the procedure (section 1.0.1) for both the forward and the backward Frênel propagator. If the considerations made in section 1.0.2 are also followed, so that the propagation scheme delineated in equation 1.7 is adopted, an equation identical to equation 1.8 is obtained, where $z_b - z_o$ and \mathbf{r}_b are replaced by $z_{eff} = (z_b - z_o)/\gamma$ and $\mathbf{r}'_b = \mathbf{r}_b/\gamma$.

2. Two-dimensional models for reverse biased p-n junctions

Dopant profile investigation is an important issue for the semiconductor industry, as the spatial distribution and the concentration of the dopant atoms are key factors in understanding device operation and validating device simulations. The need for a constantly increasing spatial resolution and sensitivity caused by the ever-diminishing feature sizes of modern semiconductor device structures has been faced, in the field framework of transmission electron microscopy, using two major approaches. The first, based on incoherent dark eld imaging in scanning transmission electron microscopy with a high angle annular dark field detector, has made it possible to distinguish the atomic columns on the basis of their content of dopant atoms [21, 22]. The high resolution is counterbalanced by the poor sensitivity, which is higher for the methods suitable to detect the electrical effects of dopants, such as phase contrast electron microscopy, whose modeling will be treated in this chapter and the next one.

The need to interpret TEM experiments and to extract useful information about the junction has for decades stimulated the development of increasingly sophisticated models [23, 24, 25, 26, 27], for the electric field around the junction. These model, however, are based on the one-sided step model describing the internal field. Unfortunately, when experiments were eventually carried out on diodes [28], the disagreement between theoretical expectations and experimental data was so striking, that it was necessary to reconsider the whole issue from the beginning and take a completely different approach. As the analytical-numerical models developed up to then were not able to take into account the real set-up within the electron microscope, the choice was made to use and adapt to our needs a professional software package developed for the semiconductor industry, the ISE-TCADsuite. In this chapter its main features will be described, in addition to how we built the model of our specimen in the TEM, and how we have interfaced the output to our programs based on Mathematica for simulating the TEM images.

Nowadays, many of the experimental data are carried out by different and accurate techniques. In this chapter, it will be also shown how experimental images in out-of-focus and interferometry of P-N junctions far from the edge are interpreted by two-dimensional numerical simulations. In particular it will

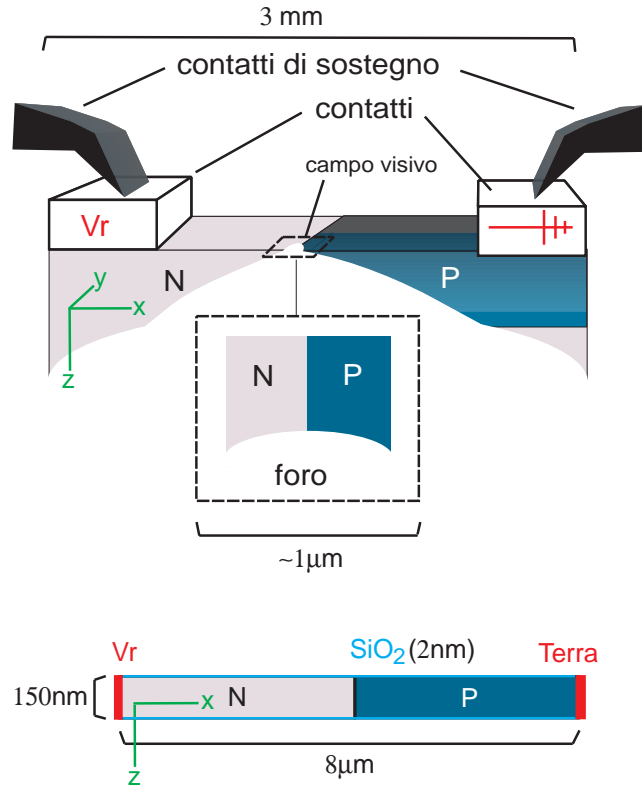


Fig. 2.1. Comparison between real (above) and simulation device (below).

be shown that the new method of electron interferometry substantially supports our hypothesis that suggests the charging of the oxide layers.

2.0.1 Device used in experiments.

Figure 2.1 shows the geometry of the device used in experiments for this thesis; i.e. diode made available by the IMM section (ex LAMEL) of CNR in Bologna. The p -zone was obtained by pre-diffusion and subsequent annealing of the boron ions in the silicon. The boron concentration is from about $1.5 \cdot 10^{19} \text{ cm}^{-3}$ to the surface, which eventually cancels itself out within the bulk. Similar to the result of thinning through the ionic beam, the thickness (in z) is not uniform and decreases to zero in the hole. The oxidation of the silicon surfaces, which determines the formation of a native oxide layer whose thickness is of the order of $1 - 2 \text{ nm}$ [29], must be kept in consideration: the positive charging of the oxide semiconductor interfaces, which results from the dynamical equilibrium between the electron-hole E - H pairs created by the effect of the electronic beam on the oxide layer and the transport of the generated charge, has a fundamental role in the generation of the electric field.

To take into account the effects that are neglected in the ideal P - N junction one-dimensional model, for the simulations that are described in this chapter the

development of a two-dimensional model has been retained sufficient (fig. (1.1) at the bottom): therefore the effect of the hole has not been taken into account [30], thus limiting the study to the part of the image that is far from the edge.

As has been done in previous works [31], and in agreement with measurements of thickness, we chose a uniform value of 150 nm. We proceeded similarly for the doping concentration, where we considered an average value, which had been calculated by the **SupremelV** simulations of Dr. S. Solmis group of the IMM. To avoid any perturbation of the regions of the junction that could be caused when contacts neared one another, we used a device with a length of 8 μm . Lastly, the native oxide layer with a hypothesized thickness of 2 nm was introduced.

In the next chapter it will be important to develop three-dimensional models. Any possible effects caused by the variation of the thickness and the presence of an edge can be studied only with a 3D simulation. The presence of an edge could give rise to phenomena of electrostatic induction that are not negligible, as has been briefly mentioned in the introduction. However, the studies that have thus far been conducted do not seem to show any disturbances by the edge in images that are far from it.

2.1 Numerical simulations of the Electrostatic Potential

Real p-n junctions observed in a TEM are inhomogeneous semiconductors thinned by ion beam, which damages the surfaces. Even if the specimen is not damaged, within a few minutes native oxides can grow and coat the whole device. Considering that the geometry is also strongly modified compared to the bulk case, it is not difficult to understand why there are not yet any analytic formulas for the electrostatic potential. It is possible to compute the electrostatic potential starting from first principles of electromagnetism by implementing the Poisson's equation and the continuity equation for electrons and holes:

$$\left\{ \begin{array}{l} V''(\mathbf{r}) = -\frac{q}{\epsilon}(\mathcal{N}(\mathbf{r}) + p_v(\mathbf{r}) - n_c(\mathbf{r})) \\ \frac{\partial}{\partial t}p(\mathbf{r}, t) - G'(\mathbf{r}, t) + U(\mathbf{r}, t) + \frac{1}{|e|}\nabla \cdot \mathbf{J}_p = 0 \\ \frac{\partial}{\partial t}n(\mathbf{r}, t) - G'(\mathbf{r}, t) + U(\mathbf{r}, t) - \frac{1}{|e|}\nabla \cdot \mathbf{J}_n = 0 \end{array} \right. \quad (2.1)$$

where V is the electrostatic potential, q the absolute value of the electron charge, ϵ the permittivity of Silicon, $p(\mathbf{r})$ and $n(\mathbf{r})$ the hole and electron concentrations, G' the density of hole-electron pairs generated per unit time, U the density of hole-electron pairs recombination per unit time, \mathbf{J}_p and \mathbf{J}_n the current density of electrons and holes, and $\mathcal{N}(\mathbf{r})$ the concentration of ionized dopants, given by [32, 33]:

$$\mathcal{N}(\mathbf{r}) = N_d(\mathbf{r}) \left[1 - \frac{1}{1 + \frac{1}{2} \exp\left(\frac{\varepsilon_d(\mathbf{r}) - \varepsilon_{fn}(\mathbf{r})}{kT}\right)} \right] + \frac{N_a(\mathbf{r})}{1 + 2 \exp\left(\frac{\varepsilon_a(\mathbf{r}) - \varepsilon_{fp}(\mathbf{r})}{kT}\right)} \quad (2.2)$$

where $N_d(\mathbf{r})$ e $\varepsilon_d(\mathbf{r})$ are the concentration and the energy level of the implanted donor impurities (i.e Phosphorus ions in Silicon), while $N_a(\mathbf{r})$ and $\varepsilon_a(\mathbf{r})$ are the concentration and the energy level of the implanted acceptor impurities (i.e Boron ions in Silicon), k and T are the Boltzmann constant and the Temperature, $\varepsilon_{fn}(\mathbf{r})$ and $\varepsilon_{fp}(\mathbf{r})$ are the quasi Fermi levels of electrons and holes respectively.

The ISE-TCAD software packages concerning the resolution of differential equations of physical origin work on discrete quantities. The discretization is performed on a mesh generated by the tool **Mesh**, and the values of the physical quantities are mapped on the nodes of the mesh.

It must be kept in mind that **DESSIS** is for discrete functions, therefore it is obvious that the discretization pace should be commensurated to the gradient of the computed functions, in our case the gradient of the electrostatic potential. The parameter that roughly indicates the potential variation in semiconductors is the extrinsic Debye length [34]. To obtain a sufficient precision the local discretization step should be smaller than the extrinsic Debye length. However, it will be shown that such ideal conditions are not always achievable, and in some cases regularizations must be introduced to avoid artifacts.

2.1.1 PDE's discretization

The so-called ‘‘box discretization’’ [35], is applied to discretize the partial differential equations (PDE) of the form

$$\nabla \cdot \mathbf{F} + R = 0 \quad (2.3)$$

. This method integrates the PDEs over a test volume such as that shown in figure (2.2), In general, ‘‘box discretization’’ discretizes each PDE of the form 2.3 into

$$\sum_{j \neq i} (d_{i,j}/l_{i,j}) \cdot F_{i,j} + \mu(\Omega_i) \cdot R_i = 0 \quad (2.4)$$

by applying the divergence theorem [36] to each node (i, j index the nodes).

For instance, in the case of the Poisson equation (the first of the system 2.1), $\mathbf{F}_{i,j}$ corresponds to $\epsilon \cdot (\mathbf{V}_i - \mathbf{V}_j)$ and \mathbf{R}_i corresponds to the charge density ρ_i . If the continuity equation for holes is also implemented (the second of the system 2.1), \mathbf{R}_i indicates the term $\frac{\partial}{\partial t} \mathbf{p}_i - \mathbf{G}'_i + \mathbf{U}_i$ and $\mathbf{F}_{i,j}$ indicates the current density $\frac{1}{|e|} \cdot J_{i,j}$.

However, because of numerical stability issues, **DESSIS** always uses as independent variables the electrostatic potential and the dopant concentrations. In

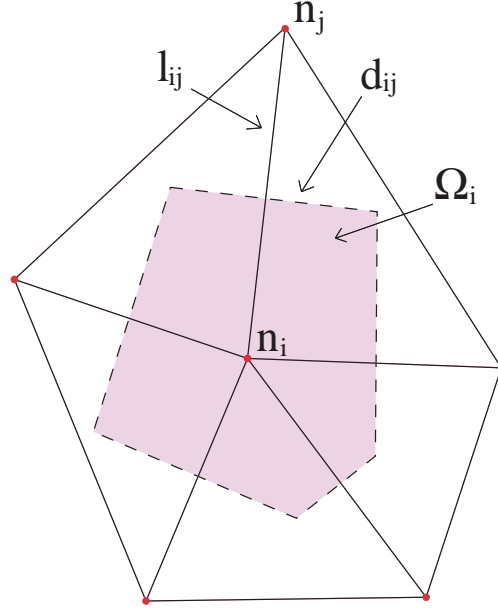


Fig. 2.2. Single box of a triangular mesh in 2D: n_i and n_j are nodes (red); l_{ij} is the distance between the i -th and the j -th node; d_{ij} , Gauss' surface element (it is a line in 2D, which is the axis of $l_{i,j}$; Ω_i , volume element of the node n_i .

fact, in the case of continuity equations (the second and the first equation of the system 2.1), the density currents \mathbf{J}_p e \mathbf{J}_n are given as functions of the electrostatic potential V and of the carrier density p ed n [35].

One special feature of DESSIS is that the actual assembly of the non-linear equations is performed element-wise [37], that is:

$$\sum_{i \in \text{Element}(e)} \left\{ \sum_{j \in \text{Vertice}(e), j \neq i} \{ (d_{i,j}/l_{i,j}) \cdot F_{i,j} \} + \mu(\Omega_i) \cdot R_i \right\} = 0 \quad (2.5)$$

This expression is equivalent to (Eq. 2.4) but has the advantage that some parameters (ϵ , μ_n , μ_p). can be handled element-wise. This is advantageous for numerical stability and physical exactness [37].

2.1.2 Boundary conditions

Charge neutrality and equilibrium are assumed at the electrodes for ohmic contacts:

$$\begin{aligned} n_0 - p_0 &= N_D - N_A \\ n_0 p_0 &= n_{i,eff}^2 \end{aligned} \quad (2.6)$$

where n_0 , p_0 are the electron and hole equilibrium concentrations. Equations (2.6), together with

$$\Psi = V_{appl} + \frac{kT}{q} \operatorname{asinh} \left(\frac{N_D - N_A}{2n_{i,eff}} \right) \quad (2.7)$$

give the Electrostatic Potential Ψ at the ohmic contacts.

If the electron or hole recombination velocity ($\mathbf{U}_e, \mathbf{U}_h$) is specified, it converts the conditions stated above to the following current boundary conditions:

$$\begin{aligned} \mathbf{J}_n \cdot \mathbf{n} &= |e| \mathbf{U}_e (n - n_0) \\ \mathbf{J}_p \cdot \mathbf{n} &= -|e| \mathbf{U}_h (p - p_0) \end{aligned} \quad (2.8)$$

where $\mathbf{U}_e, \mathbf{U}_h$ are the electron or hole recombination velocities; e is the electron charge.

All other boundaries are treated with reflective [37] (also called ideal Neumann) boundary conditions:

$$\begin{aligned} \nabla V \cdot \mathbf{n} &= 0 \\ \mathbf{J}_n \cdot \mathbf{n} &= 0 \\ \mathbf{J}_p \cdot \mathbf{n} &= 0 \end{aligned} \quad (2.9)$$

where \mathbf{n} is the normal to the boundaries, $V, \mathbf{J}_n, \mathbf{J}_p$ are the electrostatic potential and the conduction currents (sec. 2.1).

2.1.3 Validation of the 2D numerical computations

Two criteria have been followed in order to obtain reliable simulations. The first aims at a thinner discretization where the electrostatic potential slope is steeper. The discretization step is defined by the user in the input file (filename.cmd) of the ISE-TCAD meshing tools, by means of the definition of rectangular regions, called “refinement”, in which the value of the discretization step can approximately be preassigned in each coordinate direction. The criterion proceeds in the following manner: first a rough model is drawn as a way to understand where the potential is steeper. Then refinements that have a smaller discretization step are added and extended until a stationary result is obtained within some preassigned error (e.g. in order to have an error smaller than the experimental sensibility). Figure 2.3 shows an example of the adopted procedure.

The second criterion aims to check the electrostatic potential at discontinuities between materials and between regions at different doping concentration by analytical models when possible. In some cases, as is the case for the dopant concentration, the only solution is to smooth the discontinuity. Figure 2.4 shows the DESSIS solution for the electrostatic potential across an abruptly doped junction, the spike corresponding to the doping concentration step is clearly an artifact produced by the numerical method. On the other hand real dopant concentrations are never abrupt. The depletion layer width ranges from 5 nm to 100 nm and it is necessary to introduce a smooth dopant profile. A complementary error function has been implemented to perform this task.

We have also checked the band bending at the material discontinuity between Silicon and Silicon-oxide surface layer when the interface is charged. An analytical

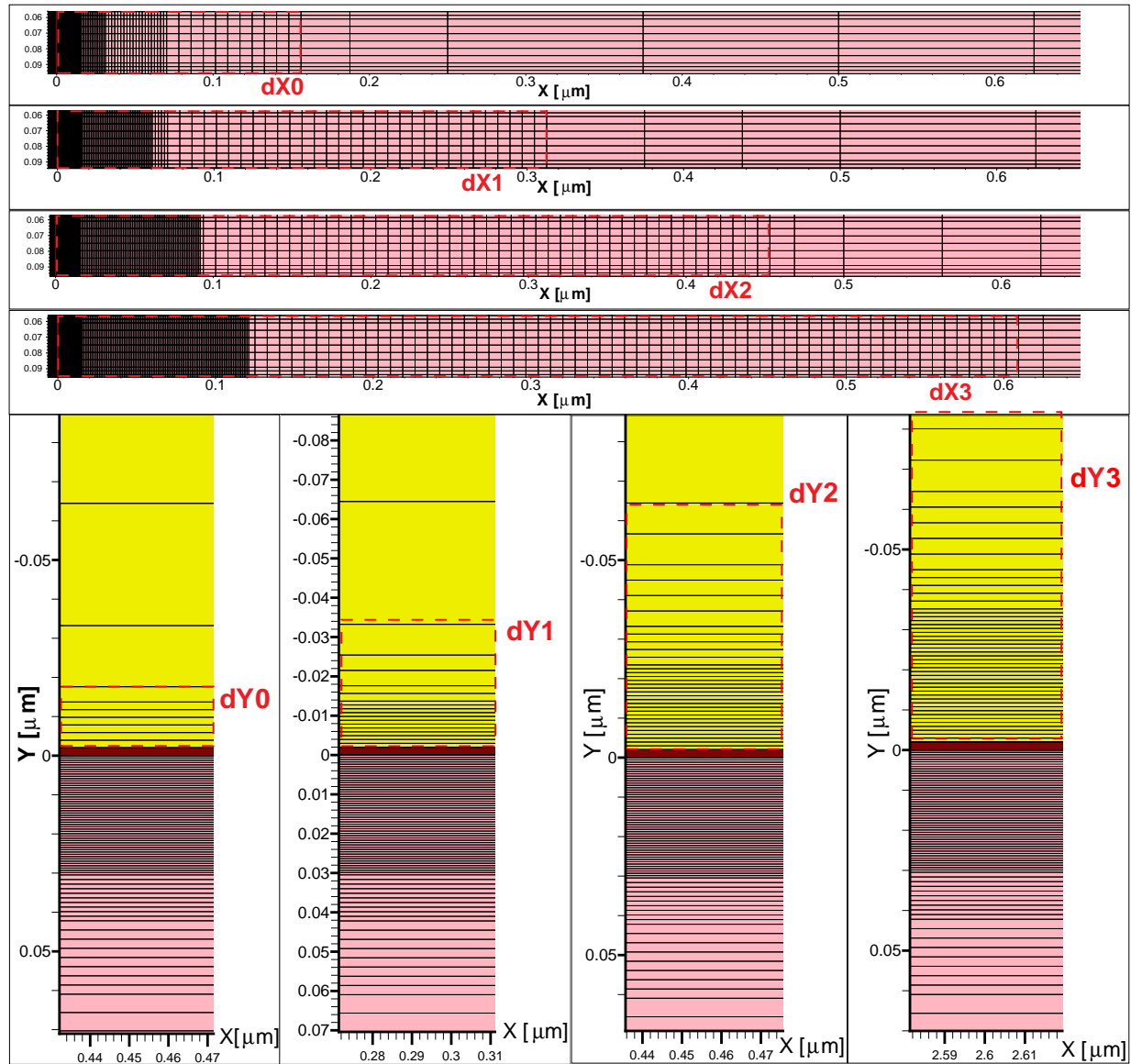


Fig. 2.3. Mesh development by refinement variation: ($dX0$, $dX1$, $dX2$, $dX3$) are the increments orthogonal to the junction (dopant profiling direction), sotto ($dY0$, $dY1$, $dY2$, $dY3$) are the increments that aim to a good resolution of the fringing field around the edge

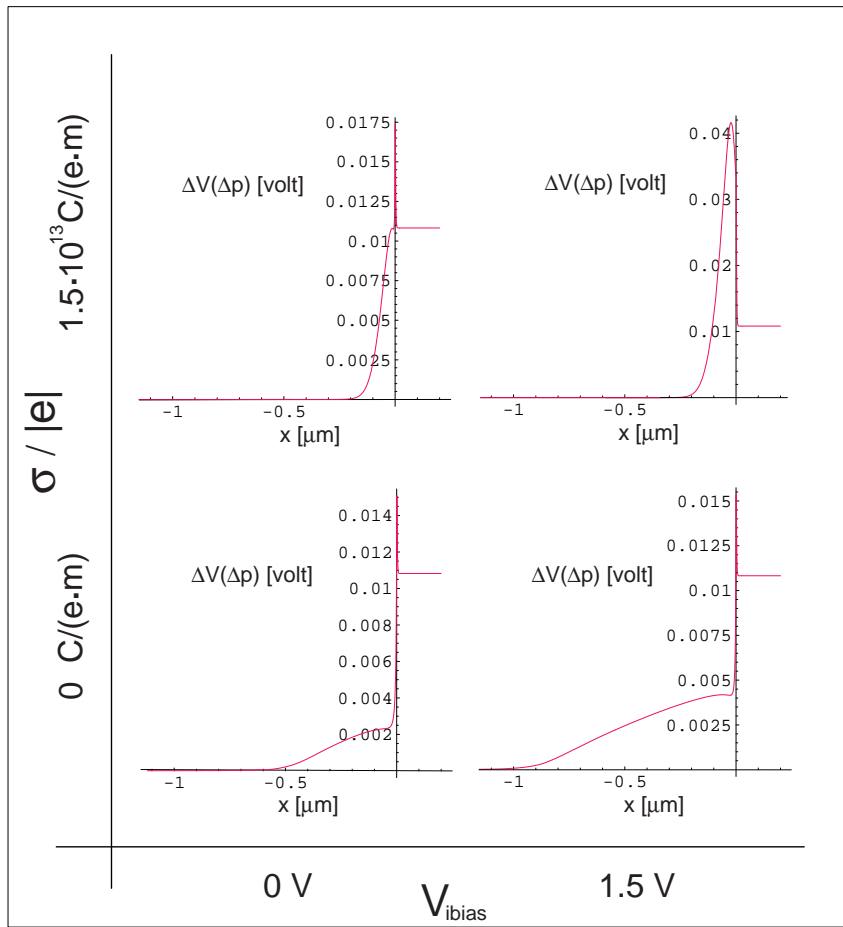


Fig. 2.4. Variation of the electrostatic potential with respect to the p-doping concentration (n_{Boro} , for $x > 0$) (axial section: $z = 0.075 \mu\text{m}$). $\Delta p = 2 \cdot 10^{19} \cdot \text{cm}^{-3} - 1 \cdot 10^{19} \cdot \text{cm}^{-3}$.

approximated model [34], which allowed us to compute the surface band bending far from the junction, has been implemented in order to assess the reliability of DESSIS on this kind of discontinuity. We found that in this case the numerical method shows no problems provided that the discretization is not wider than 1 nm around the charged interfaces.

In 3D simulations (sec.3.1.1) we also checked the software on the contact-contact discontinuity by an analytical model for the abrupt junction at the edge [26, 30].

2.1.4 Mathematica and the ISE-tCad

In this section the problem of the interface between the softwares used for simulations will be discussed. The ISE-TCAD (v8.0) suite provides tools for device simulations from device fabrication to electric computations. We used the software **Mathematica** for the wave-optical numerical analysis of the image formation (and also for analytical models), on the Electrostatic potential computed by DESSIS. In **Mathematica** “Everything is a list” - as the manual states - and the intrinsic function **Interpolation** works only on data in matricial form, i.e. on discrete functions defined on “rectangular” meshes (for instance the output data of a finite difference simulations). On the other hand, the ISE-TCAD meshing tools **Mesh** and **Mdraw** are not equipped with options that force the algorithm to generate these kinds of meshes. For this reason, one of the most demanding issues of image simulations is to make the meshing tools to generate “rectangular” meshes. This can only be done by manually adjusting the refinements (sec.2.1.3) of the files used as input for **Mesh** and **Mdraw**. Such a job must be done proceeding by trial and error and how much experience the operator has plays an important role in how quickly the desired adjustment is achieved.

The second, although not minor issue, is how to handle output data format [38] and to convert them in order to have a **Mathematica**-readable input, i.e. a list of 4-tuples, as for example $((x_1, y_1, z_1, V_1), (x_2, y_2, z_2, V_2), \dots, (x_N, y_N, z_N, V_N))$. This task has been carried out for 2D simulations by a GUI application written in Java by Dr. P. F. Fazzini, while 3D data extraction has been performed by a less manageable FORTRAN software.

2.2 2D mixed numerical-analytical computations for the interpretation of the TEM images far from the edge.

In this section the interpretation of out-of-focus (1.0.1) and interferometric (sec.1.0.2) images of a thinned reverse biased straight p-n junction, obtained at the IMM by the field emission microscope Tecnai F20, will be discussed. Although the specimen is edge ended, the junction is straight, and the region under consideration is far enough from the edge so that the one-dimensional phase object approximation can be adopted (i.e. the phase shift introduced by the specimen

only depends on the direction orthogonal to the straight junction and to the electron beam). In this case, a two-dimensional model for the electrostatic potential is sufficient, while the interpretation of the whole field image, including also the edge, requires three-dimensional modeling (Chapter 3).

At first, observations of reverse-biased p-n junctions in a transmission electron microscope by means of the out-of-focus method have shown that an agreement between experiment and theoretical interpretation can be reached assuming that the native oxides are charged under the action of the electron beam [8]. It is possible to distinguish between this assumption and the case of uncharged specimen, or the dead layer model [39], because qualitatively different predictions are given over a range of defocuses and reverse biases, in spite of the fact that the out-of-focus method is a rather poor imaging technique from a quantitative point of view [40].

A more quantitative approach is represented by electron interferometry observations, carried out by inserting an electron biprism at the level of the intermediate aperture (sec. 1.0.2). Inasmuch as the observed P-N junctions can be considered as a one-dimensional phase object, the image is a parametric representation of the phase difference between interfering points [41]. These results are therefore more directly and easily interpreted than the former out-of-focus observations [1] and more convincingly support our considerations about the existence and the role of the charged layer.

A mixed numerical-analytical approach has been developed in order to take into account the equation for inhomogeneous semiconductors (Poisson, Electron, Hole), simultaneously and to keep the boundary conditions of numerical computations under control (sec.2.2.2).

2.2.1 Dopant implantation simulation

The observed device, a P-N junction obtained by Boron deposition and annealing on a Phosphorous substrate has been simulated through the ISE technological CAD [38] obtaining the profile of both internal and external fields. The doping concentration in the substrate is known while the profile of the diffused species has been fitted with an error function profile by comparison with an ATHENA [42] process simulation.

2.2.2 Potential and phase computation.

Numerical simulations, performed with the tool DESSIS of the ISE-TCAD suite, were used to compute the electrostatic potential. The domain of the simulation and the corresponding electrostatic potential, are shown in figure 2.5. Due to the distortion of the equipotential lines at the boundaries, due to the reflective conditions 2.9 imposed by DESSIS, we did not use the numerical fringing field to obtain the electron optical phase shift. The phase shift due to the fringing field has been directly obtained from the surface potential (in this case a line potential),

by solving the Laplace's equation by means of the Fourier method [27]. The inner phase has been obviously calculated by numerical integration of the DESSIS potential. Such a mixed analytical-numerical model also reduces the effect of the reflective boundary conditions, which determine an array of parallel junctions with periodicity equal to the domain simulation width. In fact, since the inner and surface potential do not depend on the direction orthogonal to the junction, the numerical solution can be prolonged in this direction in order to increase the periodicity of the array and then reducing its effect. Therefore, the fringing field results closer to the one of a single junction and images with a wider field of view can be obtained. In our case phase functions over a domain of 16 and 32 μm have been obtained from a 8 $\mu m \times 8 \mu m$ potential simulation, to keep under control this degree of freedom.

In order to unravel the physical mechanism that reduces the external field starting from first principles, we surmised a charging of the native oxide under the action of the electron beam. Simulations have been performed with a fixed surface charge, used as a parameter that must be fit by comparison between experimental and theoretical images. Such a charge strongly influences the internal field: the depletion layer width is shrunk by an order of magnitude and comparing it with experiments confirms, at first just qualitatively in the out-of-focus case, and then more quantitatively in the interference case, the hypothesis that surfaces are charged during TEM observations.

2.2.3 Experimental results

Referring to figure (1.6), the part of the image where the biprism crosses the junction, $\simeq 3\mu m$ far from the edge, will be considered. Figure 2.6 shows how the variation of the interference fringes across the junction depends on the applied inverse bias, $(0 \pm 0.01) V$ (b) , $1.56 V \pm 1\%$ (c), $3.13 V \pm 1\%$ (d): figure (a) shows the fringe system in the absence of the specimen. In particular, besides the deformation of the fringe system whose spacing varies point by point , it can be noticed that, mainly in (d), also the intensity varies and diminishes in the A region, where the fringes are more spaced.

Finally, figure (2.7) shows out-of-focus images of the junction at the same bias and for opposite values of the out-of-focus distance.

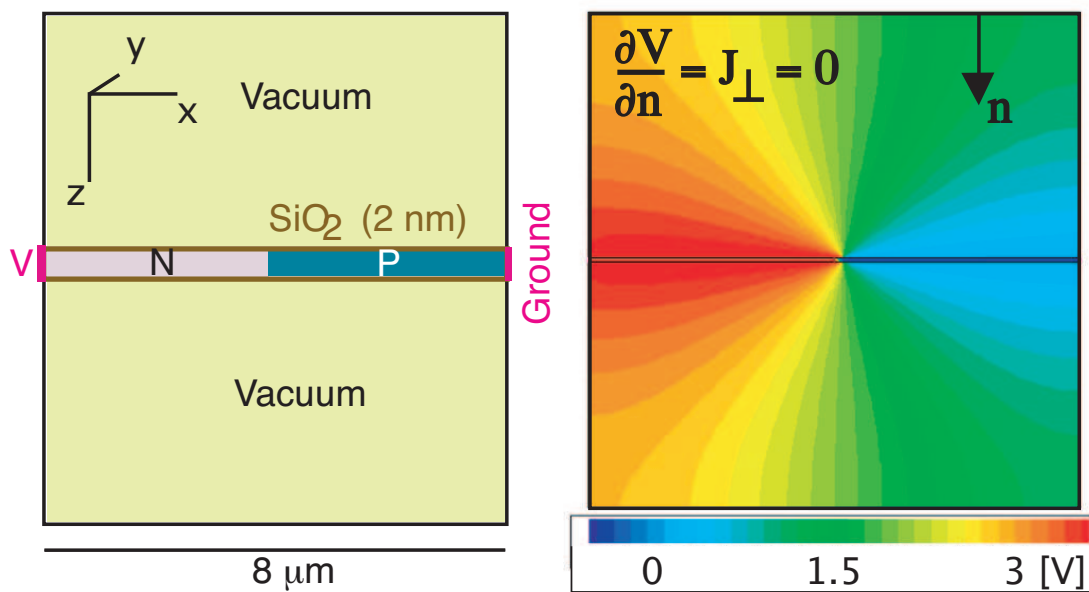


Fig. 2.5. Left: geometry used for numerical computations of the electrostatic potential. In yellow the vacuum, in pink and in blue the Silicon n - and p^+ -doped respectively, in brown the Silicon oxide ($0.002\mu\text{m}$ thick) and in red the contacts. The specimen thickness is out of scale, so that the oxide is visible. Right: the Electrostatic Potential is distorted at the boundaries, so that the vacuum must be taken large enough to avoid perturbations in the specimen potential.

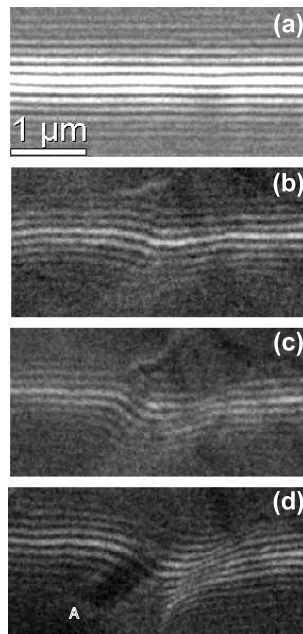


Fig. 2.6. (a); image without specimen. (b), (c), (d); local images of the junction in interferometry. The inverse bias takes the following values: $(0 \pm 0.01) V$ (b) , $1.56 V \pm 1\%$ (c), $3.13 V \pm 1\%$ (d)

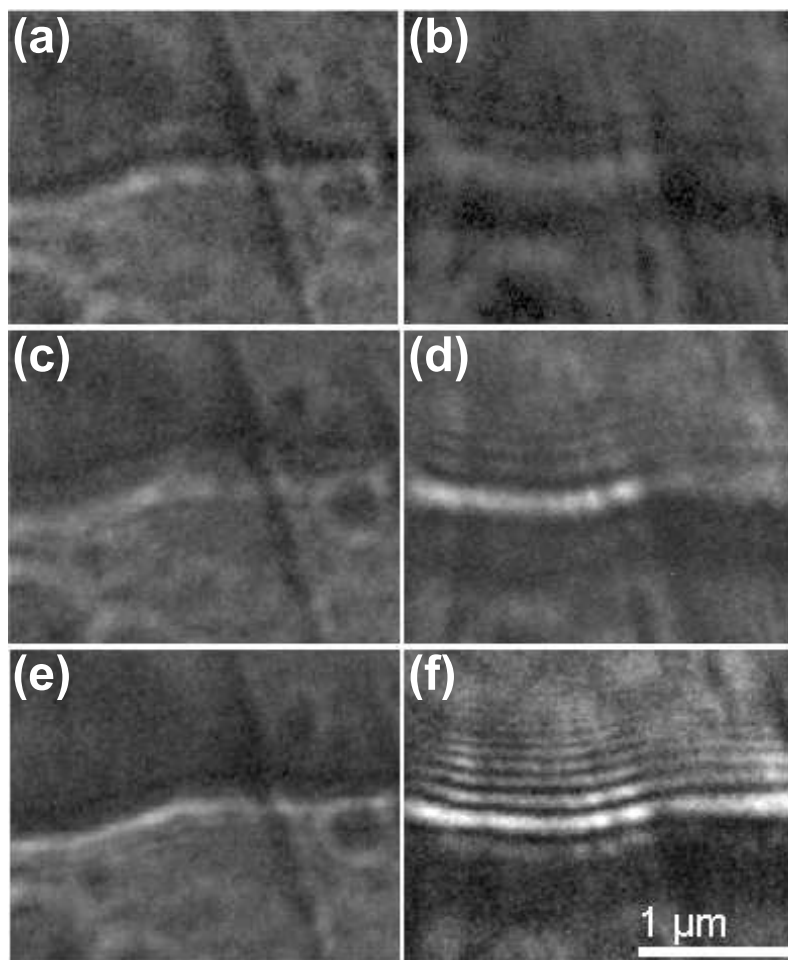


Fig. 2.7. Local images of the junction in out-of-focus: in (a), (c), (e) the defocus is $\Delta z = (-13 \pm 3) \text{ mm}$; in (b), (d), (f) it is $\Delta z = (40 \pm 2) \text{ mm}$. The inverse bias takes the following values: in (a) e in (b) $V_{\text{bias}} = (0 \pm 0.01) \text{ V}$, in (c) a in (d) $V_{\text{bias}} = 1.56 \text{ V} \pm 1\%$, and in (e) and (f) $V_{\text{bias}} = 3.13 \text{ V} \pm 1\%$

2.2.4 Interpretation of experimental images.

As stated in section (sec. 1.0.1) once the phase has been calculated from the electrostatic potential (app. A.1), it is possible to calculate the out-of-focus images by evaluating the Kirchoff-Fresnel (K-F) integral [2]. While, starting from the object wave function, the interference image can be calculated with two Fresnel propagations from the object plane to the biprism plane and vice versa, with the biprism effect in between (sec. 1.0.2) the two propagations, that is described by the transmission function (Eq.A.16). Obviously, spherical illumination was taken into account (sec. 1.1).

It is clear that the contrast phenomena critically depend on the object wave function and thus on the electrostatic potential associated with the junction. At this point the simulation of the device becomes crucial.

Let us first consider our simulations with a charge of zero, which is equivalent to a standard model of a one-dimensional junction, with the exception of a finite thickness of 150 nm and the doping profile Erfc rather than abrupt.

Figure (2.8) shows the trend of the internal potential and the surface potential, from which it is possible to calculate the external potential [27]: it should be noted that regarding what has just been stated concerning the contour conditions, the potential does not depend on z . Applying equation (A.12) it is possible to obtain the respective contributions to the phase.

If we then apply the algorithms of the calculation of the images to this model, we obtain results for the two series of images (interferometry and out-of-focus), where effects of partial coherence have not been introduced and thus are much more contrasted and detailed) that concord at least qualitatively with individual images but not with the entire series (figg. 2.9, 2.10).

This indicates that the standard junction model is not capable of interpreting experimental data, and thus it is necessary to introduce new elements to the model.

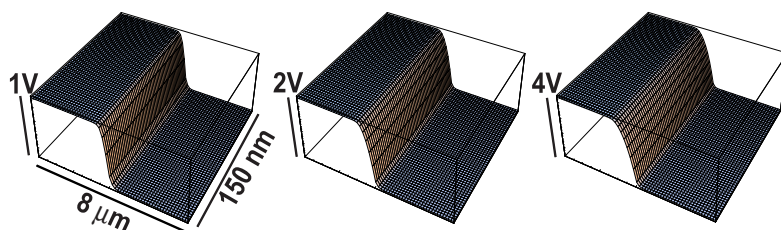


Fig. 2.8. Simulations of electrostatic potential with an oxide charge of $0|e|/cm^2$: from left to right the reverse polarization V_{bias} of the specimen is $0V$, $1.5V$ e $3V$.

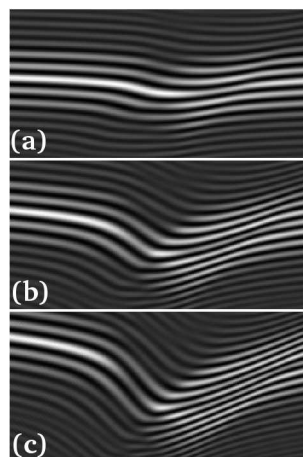


Fig. 2.9. Simulations of interferometric images with an oxide charge of $0|e|/cm^2$: in (a), (b) e (c) the values of the reverse polarization of the junctions are respectively: 0 , 1.5 e $3V$. The biprism has a potential of $5V$.

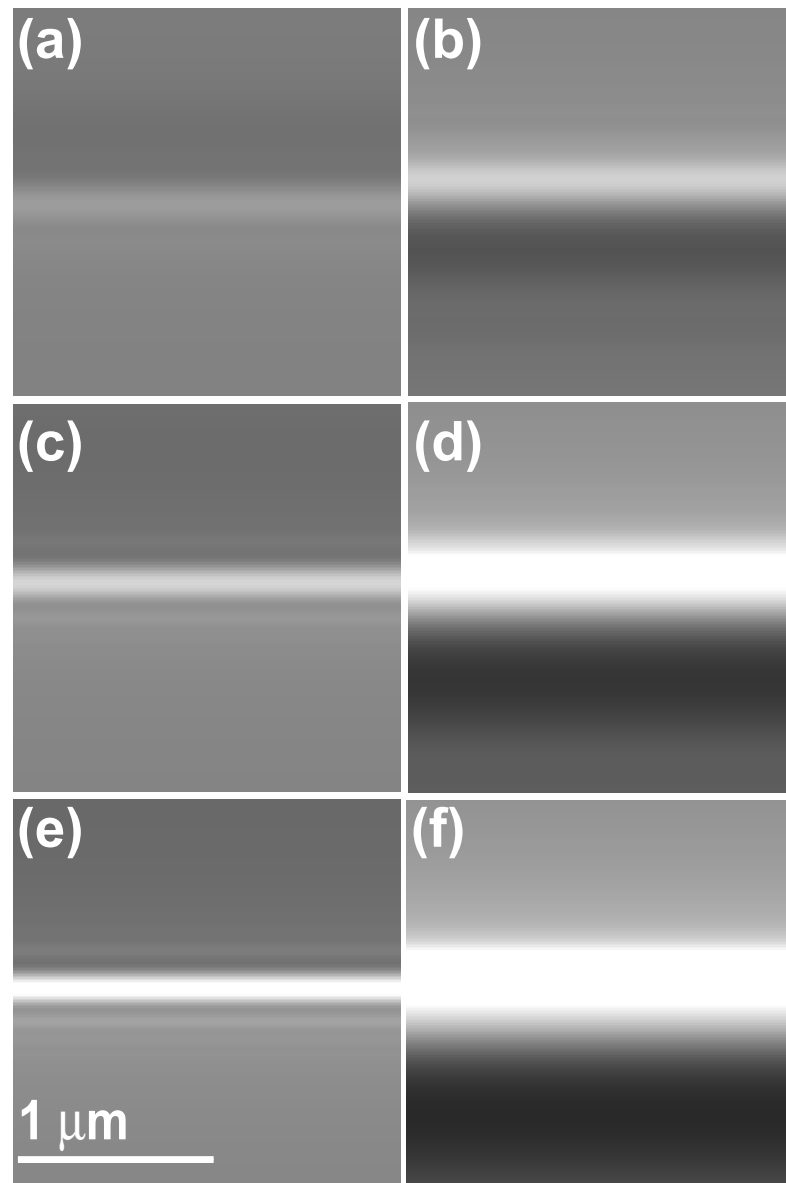


Fig. 2.10. Simulations of out-of-focus images with an oxide charge of $0|e|/cm^2$: on the right $\Delta z = 4cm$, on the left $\Delta z = -13mm$; from the top to the bottom $V_{bias} = 0, 1.5$ e $3V$ respectively.

As we have explained in the introduction of this chapter, in recent years the analysis of this problem has singled out the charging of the surface oxides as the possible and plausible origin of the observed effects.

Figure (2.11) shows the potential trend within the sample and at the surface for a density of a superficial charge on the two sides of $7.5 \cdot 10^{12} |e|/cm^2$. It should be noted that in addition to the variation of the field at the surface, which influences the field and the external phase displacement, the internal field is also heavily modified, particularly by the reduction of the width of the depletion layer.

The calculation of both the interferometric (Fig. 2.12) and out-of-focus images (fig. 2.12) show a much better agreement, thus indicating the validity of the proposed model.

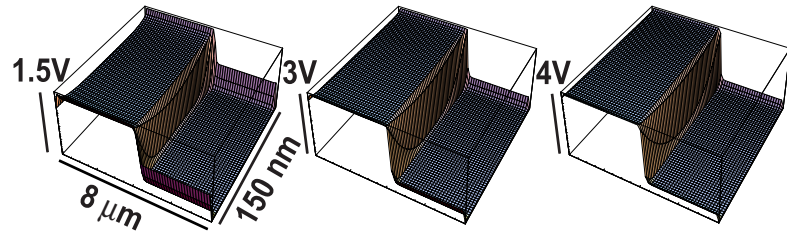


Fig. 2.11. Simulations of electrostatic potential with an oxide charge of $7.5 \cdot 10^{12} |e|/cm^2$: from the left to the right the values of the reverse polarization are 0, 1.5 e 3 V respectively.

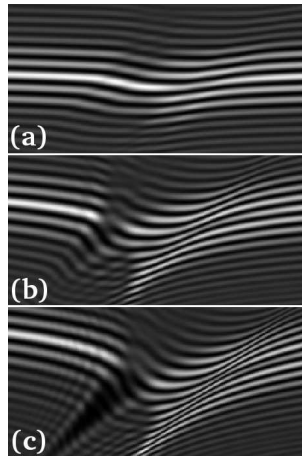


Fig. 2.12. Simulations of interferometric simulations with an oxide charge of $7.5 \cdot 10^{12} |e|/cm^2$: in (a), (b) and (c) the values of the reverse polarization of the junction are 0, 1.5 e 3 V respectively. The biprism has a potential of 5 V.

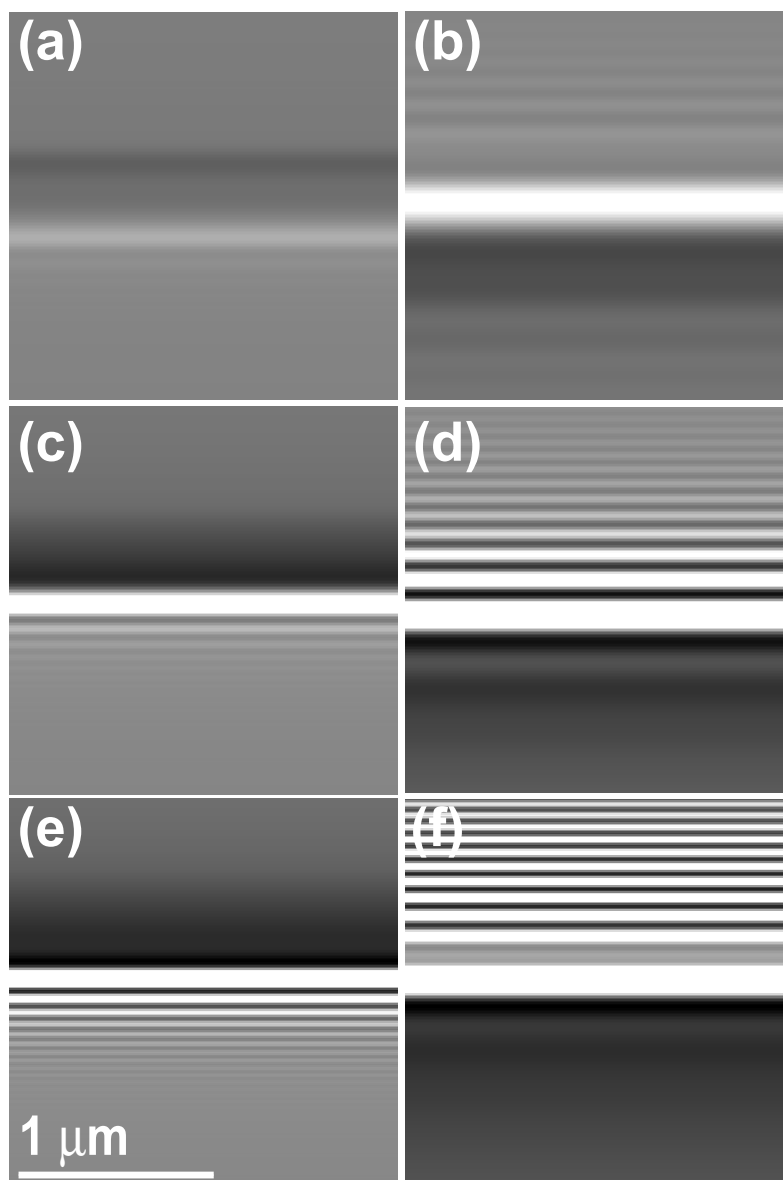


Fig. 2.13. Simulations of out-of-focus images with an oxide charge of $7.5 \cdot 10^{12} |e|/cm^2$: on the right $\Delta z = 4cm$, on the left $\Delta z = -13mm$; from the top to the bottom $V_{bias} = 0, 1.5$ e $3V$ respectively.

If the surface density charge is increased to the value of $2.5 \cdot 10^{13} |e|/cm^2$ (fig. 2.14), the electrostatic field variation at the surface is further reduced, becoming nearly zero, affecting the phase shift, as shown in the following figures (fig. (2.15), (2.16)). The comparison with the experimental data once again shows a notable disagreement, as was the case with the standard model.

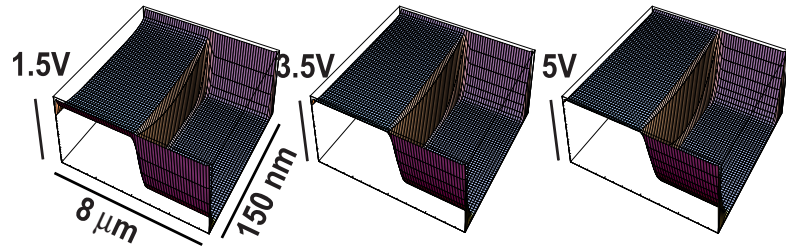


Fig. 2.14. Simulations of electrostatic potential with an oxide charge of $2.5 \cdot 10^{13} |e|/cm^2$: from the left to the right the values of the reverse polarization are 0, 1.5 e 3 V respectively.

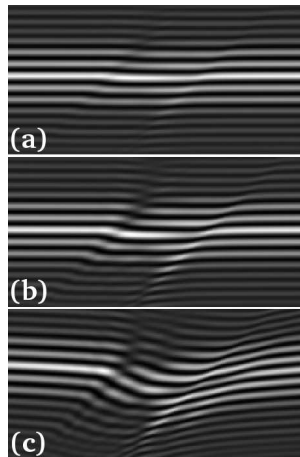


Fig. 2.15. Simulations of interferometric simulations with an oxide charge of $2.5 \cdot 10^{13} |e|/cm^2$: in (a), (b) and (c) the values of the reverse polarization of the junction are 0, 1.5 e 3 V respectively. The biprism has a potential of 5 V.

More accurate simulations around the value of $7.5 \times 10^{12} e.c./cm^2$, show that the accuracy is of $\pm 1 \times 10^{12} e.c./cm^2$.

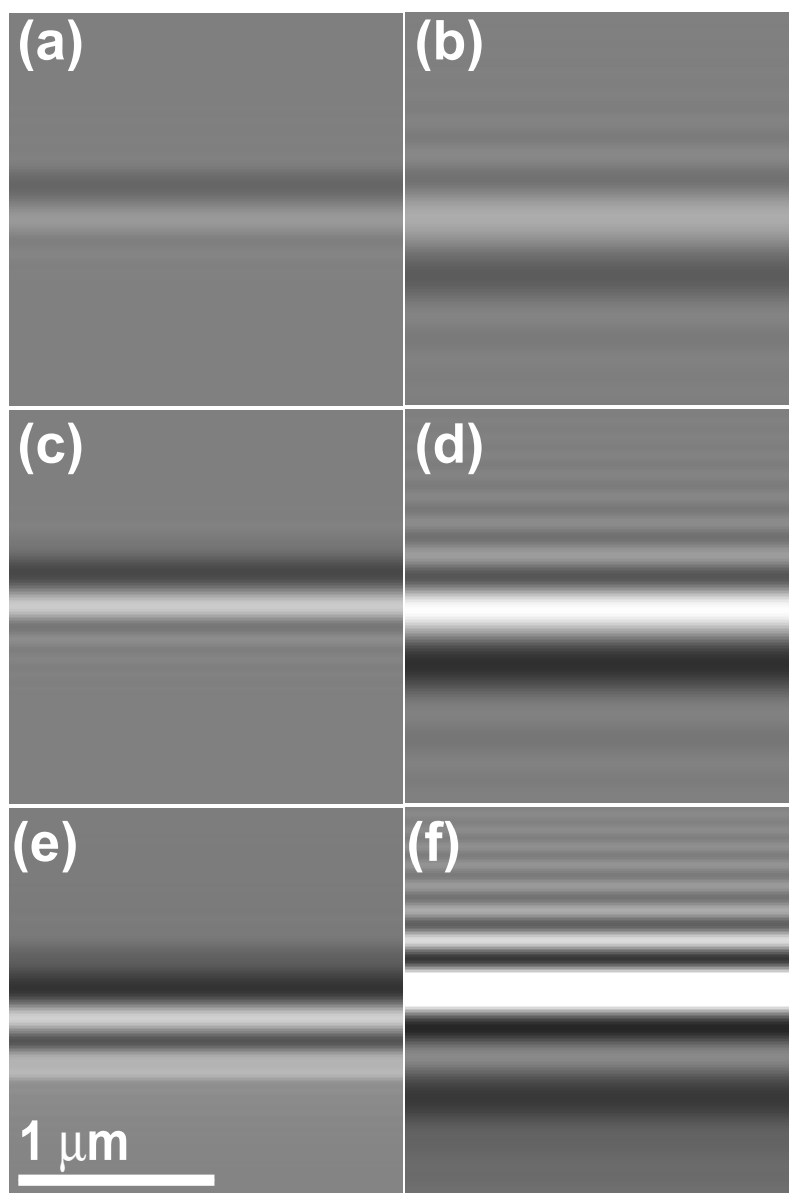


Fig. 2.16. Simulations of out-of-focus images with an oxide charge of $2.5 \cdot 10^{13} |e|/cm^2$: on the right $\Delta z = 4cm$, on the left $\Delta z = -13mm$; from the top to the bottom $V_{bias} = 0, 1.5$ e $3V$ respectively.

3. Three-Dimensional Field Models for Reverse Biased p-n Junctions.

In the previous chapter experiments on P-N junctions interpreted with two dimensional models for electrostatic potential, i.e. for one-dimensional phase-object, were discussed. Here the general observations made in the presence of an edge in the specimen will be considered. The problem becomes three-dimensional as the thin (~ 100 up to 500 nm) foil specimen is now bounded by an edge, so that the electrostatic potential is no longer constant along the direction of the junction, which is orthogonal to the edge. It will be possible to interpret the shadow and edge interferometry images shown in the first chapter (sec. 1.0.3), provided that the hypothesis of the charging of the surface oxides under the action of the electron beam is still undertaken.

Moreover, the presence of an edge is also typical of the geometry of the off-axis holography set-up (sec.1.0.4), where the electron wave transmitted by the specimen, and around its edge, is brought to interfere with the reference wave transmitted by the vacuum, that in most cases is perturbed by the fringing field generated by the specimen itself. If such a perturbation is significant, the reference wave can not be considered a plane wave, so that the reconstructed hologram is no longer truly representative of the object phase. Therefore, three-dimensional models are important in computing the whole field surrounding the specimen, allowing us to take into account all the perturbations and thus to perform image simulations that enable us to accurately recover the phase shift, and correctly interpret the experimental results.

The increase in dimension from a 2D to a 3D computation, along with the need to keep the simulation domain wide enough in order to avoid the perturbation produced by boundary conditions, leads to an effective limitation in the precision of simulations (if the machine used is equipped with an ordinary CPU) and to an exponential increase of time machine (section 3.1). In order to deal with these problems, a mixed numerical-analytical approach 3.2 has been followed, in addition to full 3D numerical computations.

This approach is similar to the one used for two dimensional simulations 2.2, since it uses the specimen potential to recover the external phase shift. The development of the mixed approach and its use can be synthesized as follows. First, the Three-Dimensional numerical computation was assessed in the case of an abrupt junction of zero thickness, constituted by two laminar contacts kept

at opposite potential (e.g. $-1 V$ $+1 V$), which can be modeled exactly with an analytical formula. Second, a finite thickness was added to the abrupt junction: there is no exact analytical solution in this case, so that the exact solution at $z = 0$ plane (the specimen plane) has been prolonged in order to obtain an approximated solution for the finite thickness case. The difference between such an approximated solution and the full 3D computation is less than 2%, reaching its maximum value in the vacuum region close to the edge. Then, the method of using the analytical formula for thick specimens was adapted to the real junction: a two-dimensional numerical computation is prolonged and patched to recover the inner electrostatic field, while the outer field is computed analytically from the numerical potential at the edge. Since the external field is diminished by the surface charging, the maximum error (2%) of the abrupt case in the vacuum region close to the edge has been considered as an upper limit at first. However, because of the more complex dynamics of semiconductors, the 2% error limit is overcome for some values of surface charging and doping concentration. Finally, experimental images in out-of-focus, interferometry and holography have been interpreted using the mixed model, as the full three-dimensional model, which is quite heavy from the computational point of view, has only been used in a few cases in order to assess the limit of validity of the mixed model. Limitations of the mixed model are discussed in section 3.2.1.

3.1 Full three-dimensional model

The full three-dimensional model used for the interpretation of the edge images of P-N junctions, is based on numerical simulations of the electrostatic potential, performed by means of the tool DESSIS of the ISE-TCAD suite. From this point of view, its features, shown in figure 3.1, are clearly the same of the two-dimensional model (chapter 2). But contrary to the 2D case, here no exact analytical formula for the external field is available. Therefore the external potential computed numerically has to be used for phase recovery. Hence the dimensions of the simulation domain become critical, as not only the specimen must not be perturbed by boundary conditions, but neither must the vacuum, which is useful for observations. For this reason, using a normal personal computer equipped with a RAM card of about 1 GB, computations with a sufficient precision are time consuming ($\sim 2days$) in the case of the interferometry, and quite impossible for out of focus simulations, which are more sensitive to the imperfections due to a poor sampling of the grid. The increase in dimension (2D \rightarrow 3D) strongly contributes to the increase in the necessary points to achieve a sufficient precision. For the sake of simplicity, if the same number of nodes is set for each dimension, the law $N = N_{x_i}^d$ can be used to compute the number of nodes (section 2.1.1) of a d -dimensional simulation with N_{x_i} nodes per dimension. For instance, with $N_{x_i} = 50$, it can be easily verified that a 2D simulation of 2500 nodes is equivalent, in precision, to a 3D simulation of 125000 nodes. But, in the case of the machine used for this thesis, the 2D simulation takes 10 minutes compared to

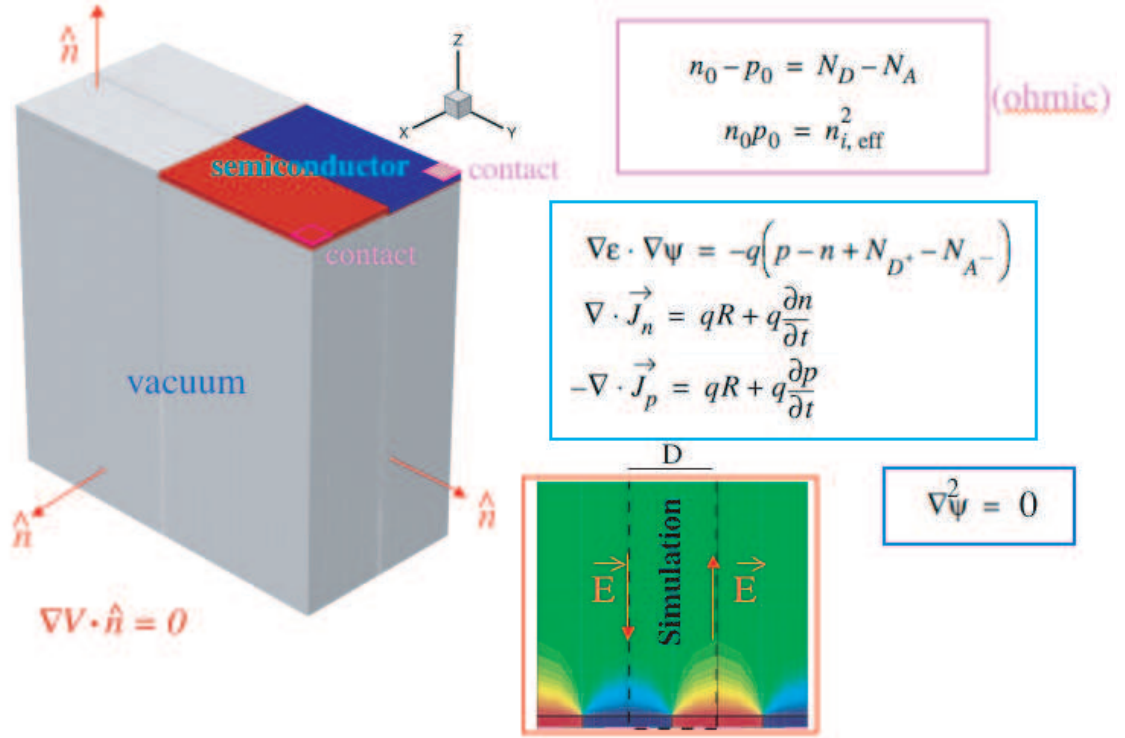


Fig. 3.1. The full three-dimensional model. (a). (b). (c). (d). (e).

the 2-3 days of the 3D simulation. Since a good 2D simulation has got at least 10000 nodes, it is clear that a super-computer or a parallel processing system with ordinary CPU would be necessary to easily perform a reliable 3D simulations. The CPAC model developed in section 3.2 is of some help in this case.

3.1.1 Validation of the 3D numerical computations

The only way to assess the reliability of a finite-element numerical software package is to vary the parameters until a stationary result is obtained within some preassigned error (sec.2.1.3). In our case, the availability of an analytical model allows us to reduce the arbitrariness and to evaluate better the accuracy of the numerical approach. Therefore, we first applied the ISE-tCad suite to simulate the case of an abrupt p-n junction in a very thin specimen and compared the results to the analytical calculations for the field and the integrated potential (proportional to the electron optical phase shift, which is the important quantity for the simulations of TEM observations). To this end, the simulation domain was extended independently in z and y , the sampling density across the junction has been increased until the electrostatic and the integrated potential showed negligible modifications in the region of interest (Fig. 3.2). The variation along the x direction is not considered because it is directly related to the periodicity of

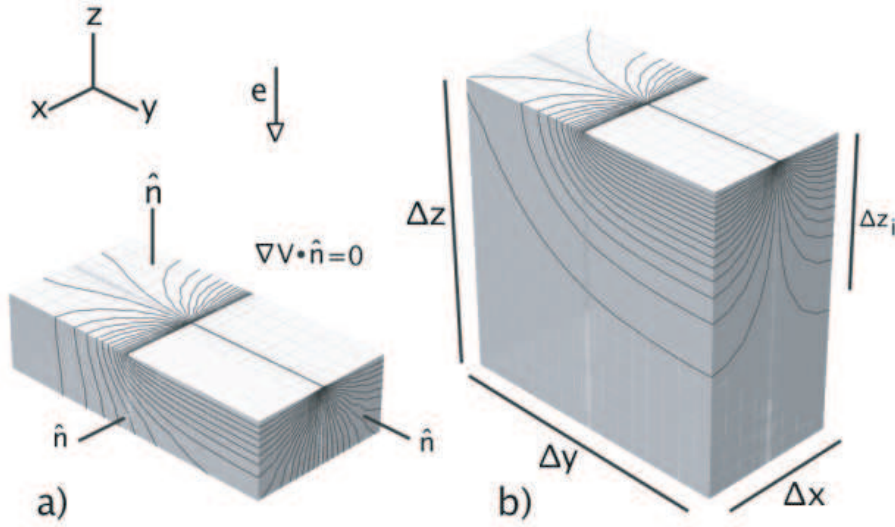


Fig. 3.2. Equipotential surfaces of a step junction ($\pm 1V$) with negligible thickness; $\Delta x = 4\mu m$, $\Delta y = 8\mu m$. a) $\Delta z = 2\mu m$; the simulation domain is too small along z , and artifacts introduced by the boundary condition $\nabla V \cdot \hat{\mathbf{n}} = 0$ are evident when the potential topography is compared to b, where the simulation domain was extended to $\Delta z = 8\mu m$: in this case, the electrostatic potential is well contained in the simulation domain, vanishing before z reaches the domain edge. Note also that the choice of Δz affects the equipotential surfaces also along y , as visible by comparing the stray field potentials in the vacuum region ($y < 0$). In b Δz_i denotes the range of the integration of the potential used to evaluate the phase shift associated with the junction.

the array (see section 2.1.2 for the boundary condition implemented in numerical simulations).

The comparison of numerical results with those obtained by calculating the analytical expressions through Mathematica [43] shows that we determined the appropriate domain size and sampling resulting in a maximum relative error of 0.001 in the potential and of 0.02 in the integrated potential calculated over the whole vertical length (Fig. 3.3), where the phase shifts are calculated for 200 keV electrons.

It is interesting to note that this error decreases to 0.01% if the potential is integrated only up to half the simulation domain Δz . This effect is due to the distortion of the electrostatic potential near the simulation edges induced by the boundary conditions used in the numerical computation. These results show that the numerical evaluation of the phase shift is more strongly affected by the choice of the boundaries than by the potential, and in order to have reliable results we have to “waste” numerical resources to include the empty space around the specimen. These resources may be better utilized in the device simulation if the external field and phase shift are calculated whenever possible using the analytical results. Since, however, real specimens are most likely thick objects, we have to account for their finite thickness. To this end, we employ a mixed

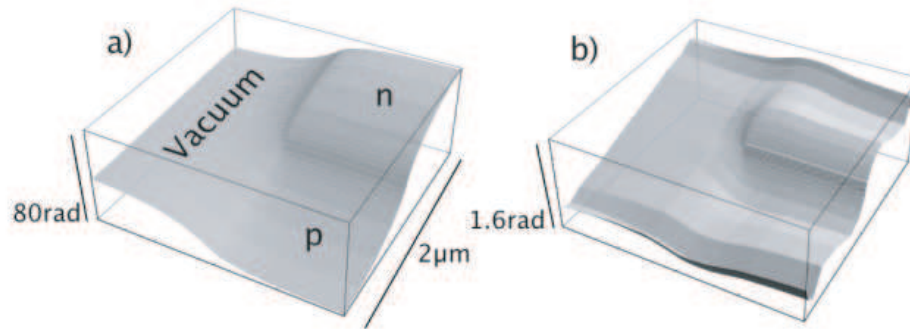


Fig. 3.3. a) Phase shift obtained by numerical integration along z of the ISE-TCAD potential of a $-1V(p) + 1V(n)$ step junction. b) its difference with the analytical phase shift of the same junction. The absolute difference decreases down to $0.8rad$ by adjusting the range of integration Δz_i to half Δz (see Fig. 3.2)

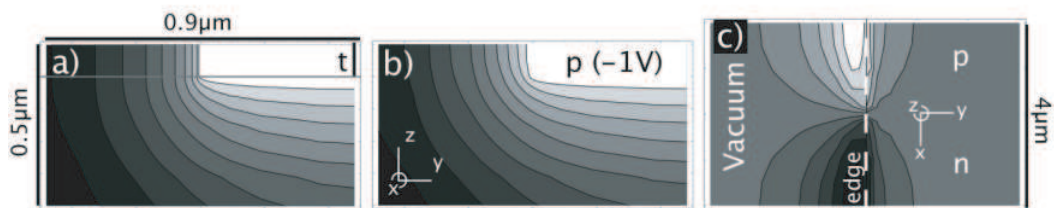


Fig. 3.4. a) Vertical section of the potential at $0.5\mu m$ from a $200nm$ thick junction obtained by prolonging the $z = 0$ plane potential along the specimen thickness. This procedure results in straight equipotential lines over the thickness t . b) the fully 3D simulation over the same region, showing small differences with respect to a. c) phase difference contours between the models a and b; the largest error is of 2.5%, and becomes 4% at $300nm$ thick. However, the error lies mainly outside the region of interest, across the junction.

numerical-analytical approach that consists of taking the analytical model for the zero-thickness step junction (Fig. 3.4a) and prolonging its $z = 0$ plane potential along z over the thickness t . This approximate potential is then compared to the fully three-dimensional model (Fig. 3.4b): the equipotential lines look very similar for both cases and the comparison between the phase shifts confirms that the “prolonged” model is affected by a maximal relative error of about 0.04%. The error, however, lies mainly outside the region of interest across the junction.

3.2 The CPAC Model for the semiconductor junction

To improve our 3D model, we extended the former considerations to a realistic semiconductor junction, and introduced the CPAC model (Cut, Paste, Analytical Computation). This approach consists of building a 3D potential by cutting, pasting and prolonging with analytical computations parts of a 2D simulation.

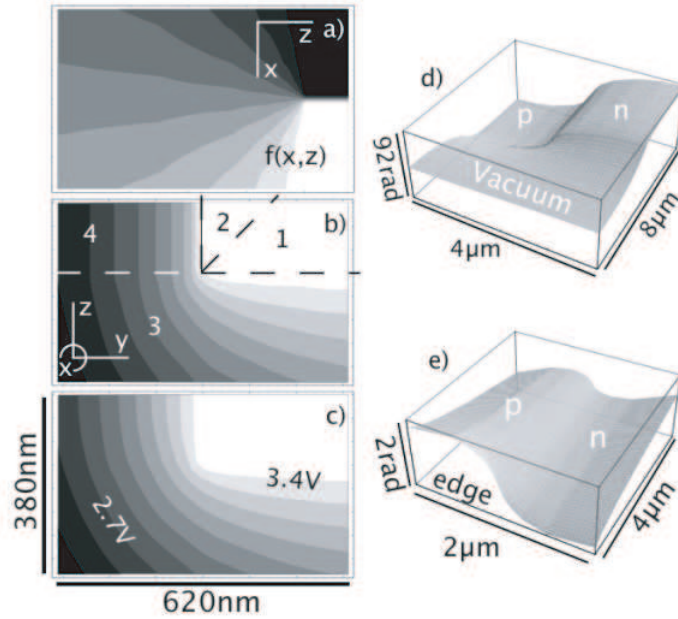


Fig. 3.5. The CPAC model of a Sb-B junction at 3V reverse bias: a) $f(x, z)$ is the 2D potential. b) the CPAC 3D model; region 1: the potential is $V(x, y, z) = f(x, z)$; region 2: $V(x, y, z) = f(x, y)$; region 3: analytical computation from the 2D surface line; region 4: constant prolongation from region 3. c) numerical 3D model to be compared with the CPAC. d) phase shift associated to the numerical 3D model. e) phase difference between the two models over the specimen: the relative error is less than 3%

The way of cutting, pasting and prolonging the potential is suggested by the similarity between the prolonged potential, as discussed above, and the fully 3D simulated potential. First, a 2D simulation is taken (Fig. 3.5a), and its surface potential is utilized to compute the potential in the region 3 of Fig. 4b by using the analytical formula [26, 30], while the inner potential is cut and pasted with a 45 degrees pattern to recover the 3D specimen potential. The choice of this particular patching angle (45°) is somewhat arbitrary, and most likely depends on the thickness. In fact, while it is certainly reasonable that in the limiting case when the specimen thickness is very large, the symmetry dictates the same potential topography as a function of y and z , for thin specimens it is conceivable that other patching angles may be more appropriate. Also, it is not clear whether patching should occur along a straight line rather than along a more general curve. However, for very thin specimens, the smaller relative contribution of the internal field topography to the total potential may minimize the effects of choosing a different patching procedure.

Finally, the analytical potential of region 3 is extended over the thickness in front of the specimen with a constant z prolongation to recover the potential of the region 4. Such a model is a good approximation for a real device if the full 3D surface potential doesn't vary appreciably in the directions orthogonal to the

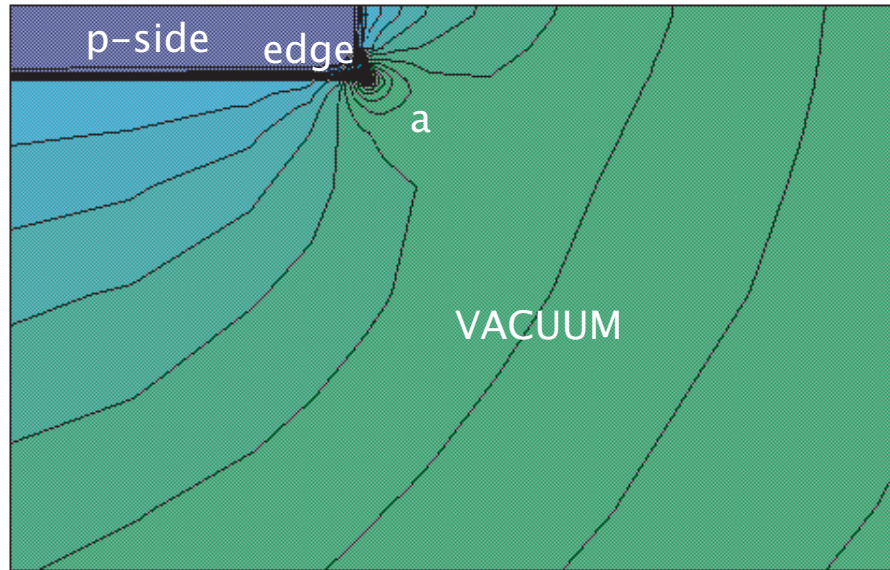


Fig. 3.6. Vertical section of the electrostatic equipotential contour lines of a Full 3D simulation of a 300 nm thick Sb-B doped Si P-N junction. In “a” is visible the perturbation on the potential by the tip effect due to the sharp edge

junction, i.e. y and z . Fig. 3.5c shows the equipotential lines of a 3D numerical simulation: the condition of constant surface potential along the y and z directions is satisfied. The comparison with the corresponding CPAC simulations (Fig. 3.5d) shows that the two models look very similar: the relative differences between phase shifts do not exceed 0.03 over the specimen (Fig. 3.5f).

3.2.1 Further considerations on 3D simulations - CPAC versus full 3D

As discussed in previous sections (3.2,3.1), the CPAC model differs from the Full 3D computation in that it assumes that the Electrostatic Potential inside the specimen and at its surface is constant in every plane parallel to the junction. However, the full three-dimensional computation is performed assuming a fixed uniform charging of the oxide under the electron beam. A vertical section of the edge potential is shown in Fig. 3.6. The full 3D model discussed here should be more accurate in predicting the behaviour of the junction at the edge, and the CPAC should be considered an approximation. But the situation is more complex than expected. Indeed, since our 3D simulations have always been performed on a square grid in order to avoid the problems concerning data transfer from the ISE-TCAD format to a format readable by Mathematica, the 3D junction is modeled by a parallelepiped with a very sharp edge. This can be considered a rather rough approximation, as such a feature is not perfectly traced in the geometry of real specimens, and tip effects on the external field are usually strongly dependent on the radius of curvature (it is zero in our 3D simulations). This is mainly true for perfect conductors, and high doped semiconductors of junctions modeled

in this thesis can be considered good conductors. Real edges are more or less rounded so that the CPAC is probably more suitable for the interpretation of some experiments. In the future, the next step in simulations will be to control this further parameter. The discrepancy between the models depends on the presence of the surface charge, as shown in figure 3.7.

3.3 Interpretation of the Experimental results in out-of-focus and interferometry.

In this section the image interpretation of the Argon milled specimens prepared and observed at the IMM/LAMEL section of the CNR in Bologna will be discussed. The 3D model allows us to simulate the whole field of out-of-focus and interferometry images obtained by P. F. Fazzini by the Philips CM 30 TEM. The simulation of these images in their entirety becomes rather challenging from the numerical point of view, if the machine used for computations is a normal personal computer (see sec. 3.1). In fact, the large field of view ($\simeq 15 \mu\text{m}$) and the long range electrostatic field generated by the junction, mainly at higher values of the reverse bias, impose a simulation domain of at least the same dimensions, in order to include the main features of the image without perturbing them by the boundary conditions. In addition, despite the low resolution of such images, if compared to the holography images recorded by the HREM group of Cambridge before 2007, the mesh used for simulations must have a discretization step not larger than the order of the nanometer in regions where the electrostatic potential shows sharp variations (Silicon-oxide interface), in order to avoid systematic errors that propagate and affect the whole solution.

3.3.1 Out-of-focus

3D models make the simulation of large field images in out-of-focus (Fig.3.8) possible. Previous works about microscope calibration [3] are fundamental to obtain the correct values for the magnification and particularly for the out-of-focus distance used in simulations, from which the fringe trend related to the edge and the junction depends. However, the agreement between experimental and simulated images is not reached (compare Fig. 3.8 to Fig. 1.8), due to the poor sampling of the Full 3D model. The fringe trend is roughly similar to that obtained in the experiments, but the difference in some details is noticeable. As discussed in section 3.2.1, the Full 3D model and the CPAC model are not consistent and the CPAC was not used. In this case, to perform Full 3D a super-computer or a parallel processing system with ordinary CPU is necessary. The shadow images at the edge of the specimen require a simpler analysis, as the step height mainly depends on the external eld and as it is a geometric optical effect, it is a linear function of the defocus [30]. The amount of the edge deformation is in agreement with experiments.

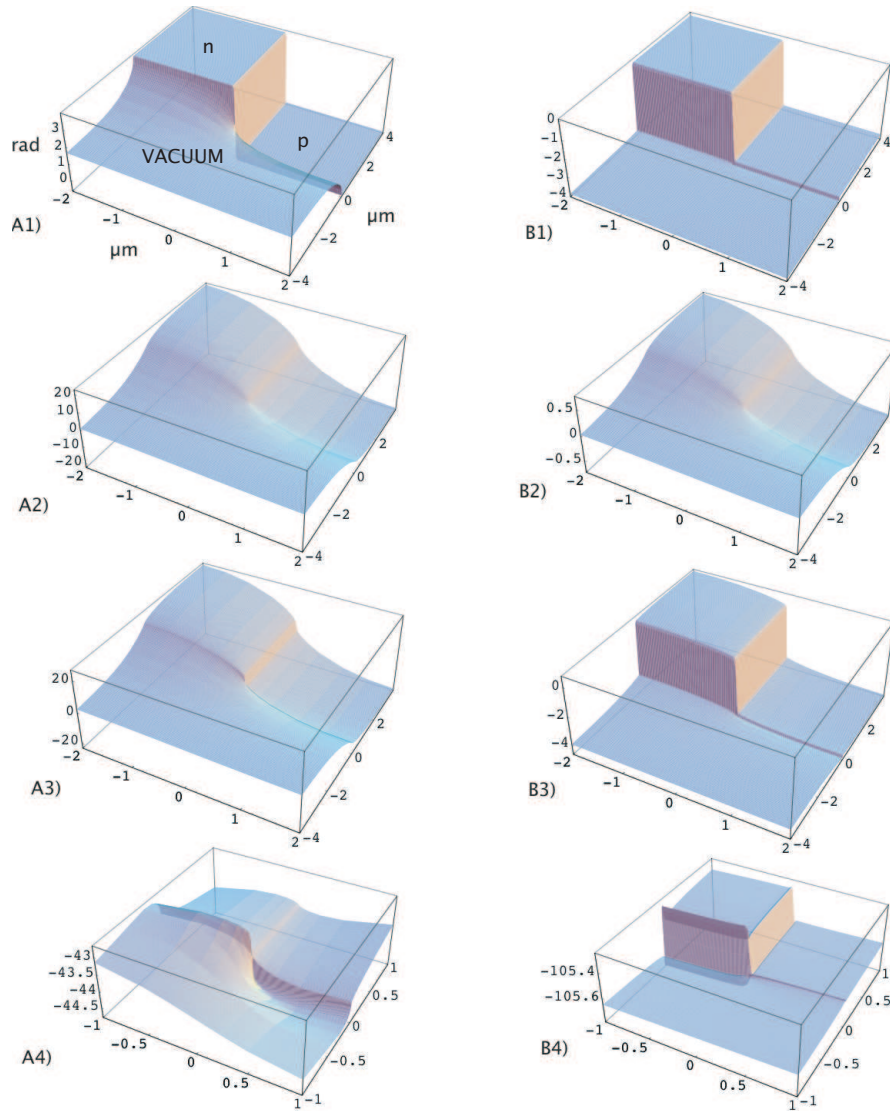


Fig. 3.7. Comparison between the phases obtained by CPAC and Full 3D model (electron beam energy 200 keV), for an abrupt (the dopant concentration is modeled by an error function with $\sigma = 5$ nm layer is $\simeq 5$ nm) Sb-B reverse biased (3 V) Si p-n junction (300 nm thick specimen). Left: no surface charge (“bulk approximation”). Right: Surface charge of $1.5 \times 10^{13} e.c./cm^2$. A1,B1) Phase contribution of the specimen “layer”. A2,B2) external phase. A3,B3) total phase. A4,B4) Difference between the CPAC and the Full 3D phase. Contrary to our expectations, in this case, the discrepancy between models does not shrink when surface charge is present: the agreement gets better for the fringing field, but it gets worse in the specimen, introducing an additional bias to the junction. This is due to the abruptness of the junction.

3.3.2 Interferometry

The large field interferometry images (see for example figure 1.6) have been simulated thanks to the 3D Electrostatic potential obtained by means of the 3D models. The field of view is large (μm), and the Full 3D model is not sufficient

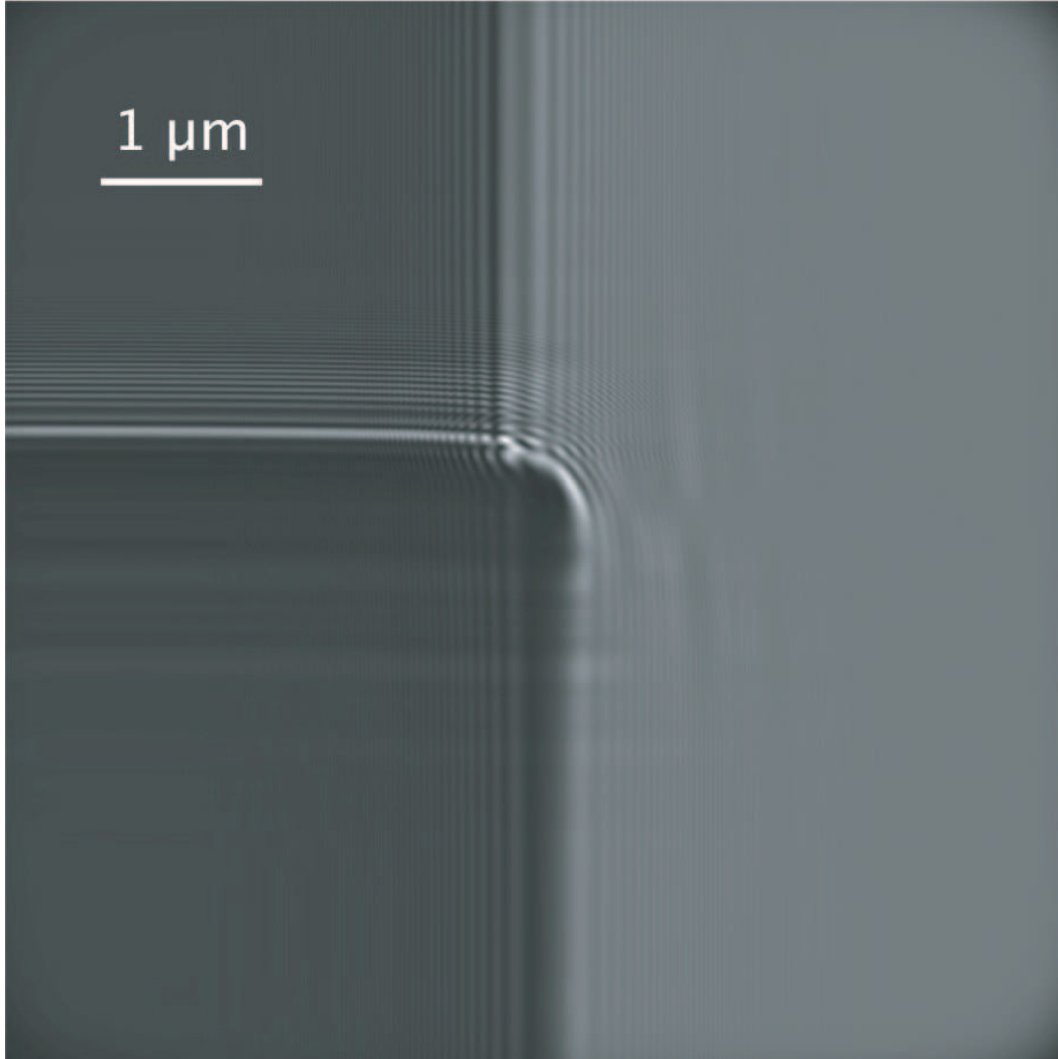


Fig. 3.8. Image simulation of a reverse biased p-n junction observed in out-of-focus: the defocus distance is $z_{eff} \simeq 40mm$. p-dopant concentration: $1 \times 10^{19} e.c.cm^{-3}$. n-dopant concentration: $1 \times 10^{15} e.c.cm^{-3}$. Reverse bias: 5V. Surface charging concentration imposed: $7.5 \times 10^{12} e.c.cm^{-2}$. The conditions are the same of the experimental image shown in figure 1.8. However, the simulated image does not fit the experiment, because of the poor sampling of the full 3D model (fringes appear in correspondance of the the mesh steps).

to simulate the whole image. Hence the CPAC model (sec.3.2) has been used, in spite of its limitations. Let us consider the images with a reverse bias of 3V, that show the most peculiar features. The whole field of view of interferometry experiments is recovered (Fig.3.9): the characteristic bending in the fringes of the biprism when it crosses the junction is still present. It is consistent with the approximation undertaken in 2D simulations, i.e. the region where the biprism crosses the junction can be considered at a distance $\simeq \infty$ from the edge. When the surface charge is brought to $2.5 \cdot 10^{13} e.c.cm^3$ (Fig.3.10), the fringe trend is perfectly straight, which means that no external field is present. Only a smaller

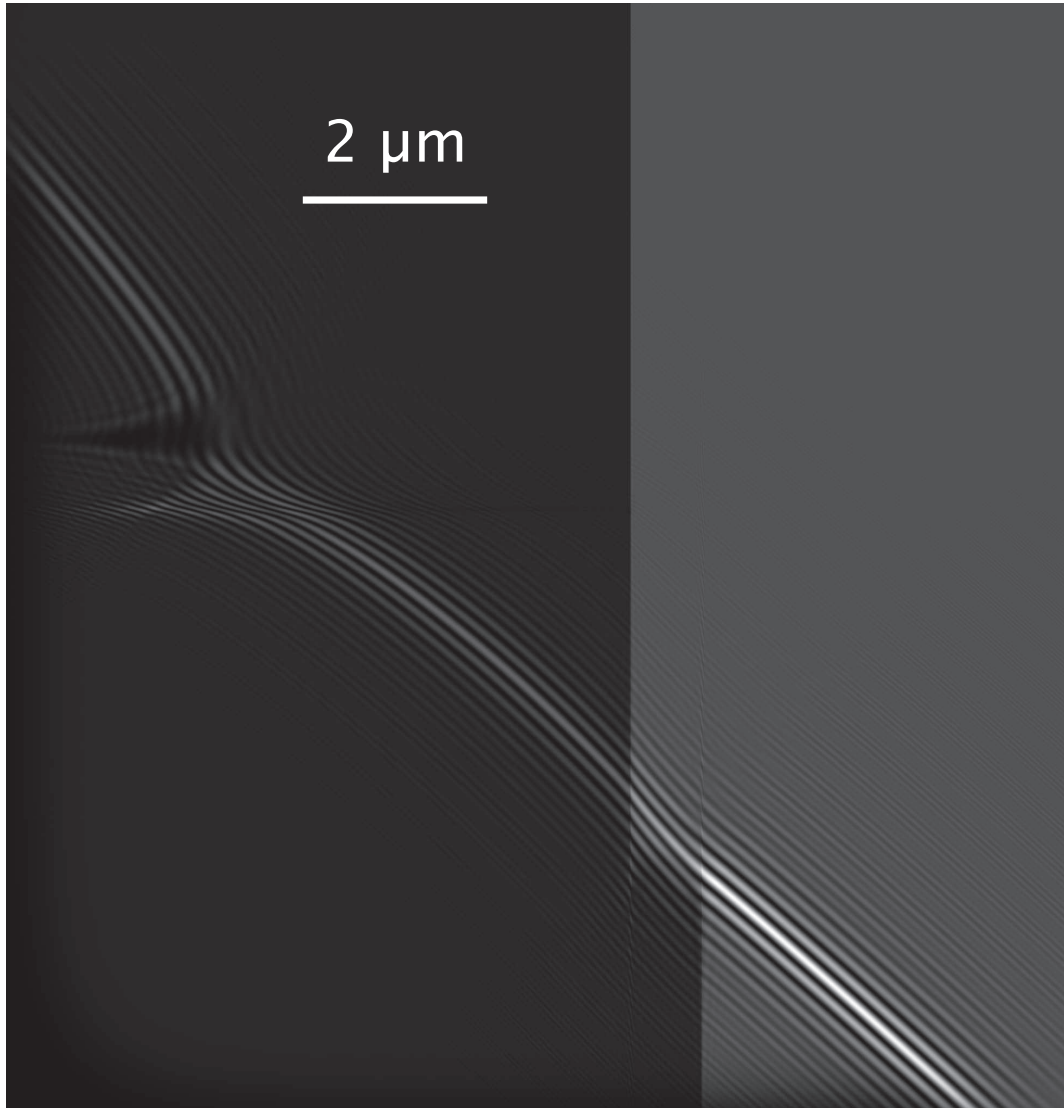


Fig. 3.9. Large field images of the junction in interferometry. Reverse bias: 3V. Surface charging concentration imposed: $7.5 \cdot 10^{12} e.c.cm^{-2}$.

lateral displacement across the junction caused by the influence of the internal field is present, contrary to the experimental images that are fit by simulations performed at a value $7.5 \cdot 10^{12} e.c.cm^{-2}$. On the other hand, such a value of the charge cannot be shrunk further, as the junction width increases producing a different slope across the biprism intersection (in figure 3.11 the case of zero surface charge is shown).

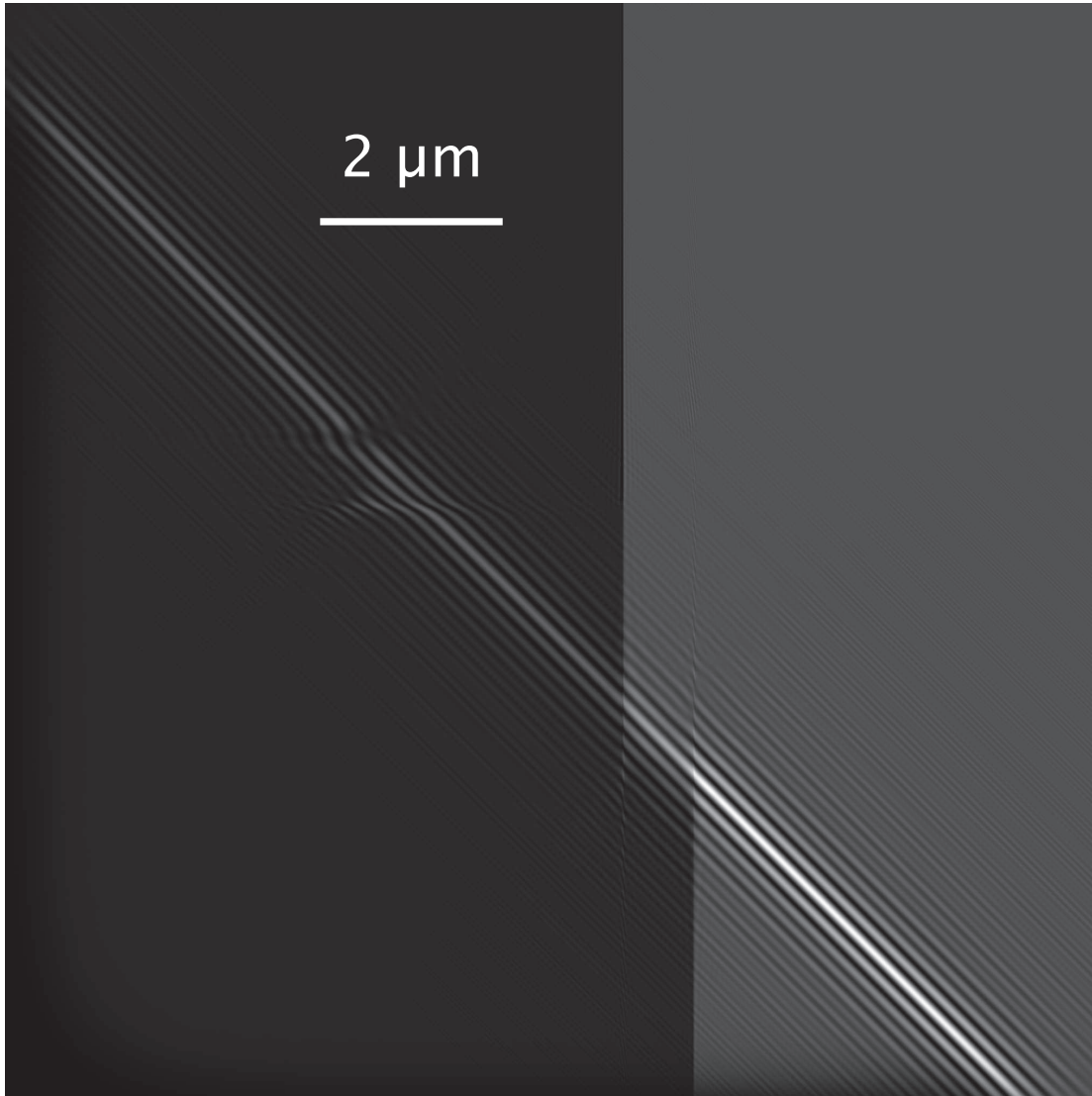


Fig. 3.10. Large field images of the junction in interferometry. Reverse bias: 3V. Surface charging concentration imposed: $2.5 \cdot 10^{13} e.c.cm^{-2}$

3.3.3 Holography

A 3D model is necessary to compute the external field protruding in the vacuum in front of the edge. These kinds of computations, in general, are of great importance in the case of electron holography simulations, as the fringing field may perturb the reference wave so that it can not be assumed as a plane wave. If this is the case (see also chapter 4), the reconstructed hologram is no longer truly representative of the object phase. In this section a holographic image of an abrupt (Erfc dopant concentration: $\sigma = 5$ nm) Sb-B doped ($4 \times 10^{18}/cm^{-3}$) symmetric p-n junction is modeled by means of the CPAC model. The specimen, milled by

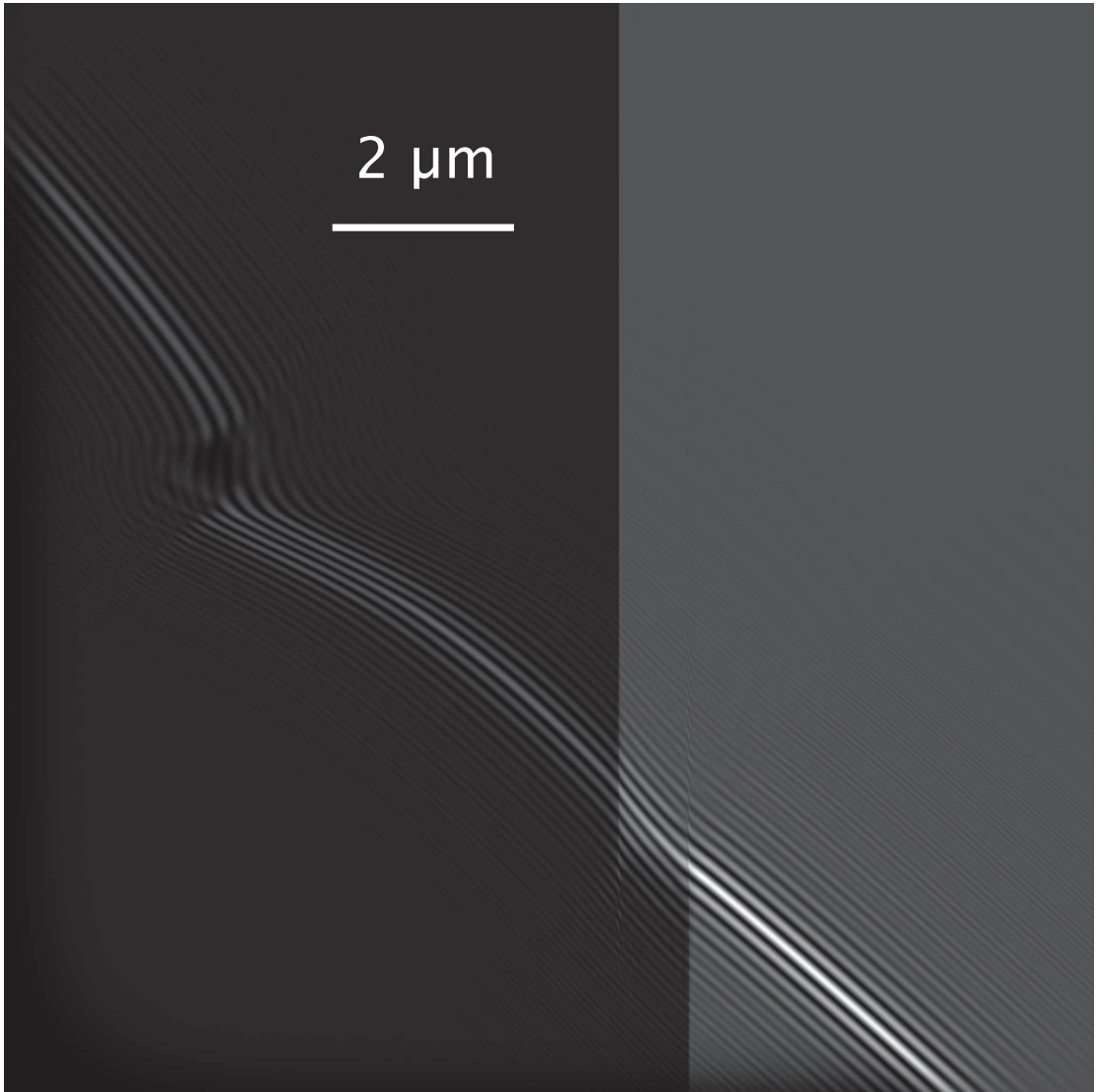


Fig. 3.11. Large field images of the junction in interferometry. Reverse bias: 3V. Surface charging concentration imposed: $0e.c.cm^{-2}$

a Gallium FIB, with a thickness of $\sim 500nm$, has been prepared and observed by the HREM group at the University of Cambridge. An intensity image shows the oxide surface layer produced during the FIB milling (Fig. 3.12:2a). FIB milling causes severe damage to the crystal lattice close to the specimen surfaces [44]

In addition to the oxide surface layer, another layer due to the FIB milling is present between the former and the bulk. These layers contribute to the most interesting feature of the contour map image (Fig 3.12B): the strong phase wrapping that corresponds to these “electrically altered” layers. Another effect that is linked to the phase wrapping is the cancellation of the fringing field, which would be present if the standard bulk approximation were valid.

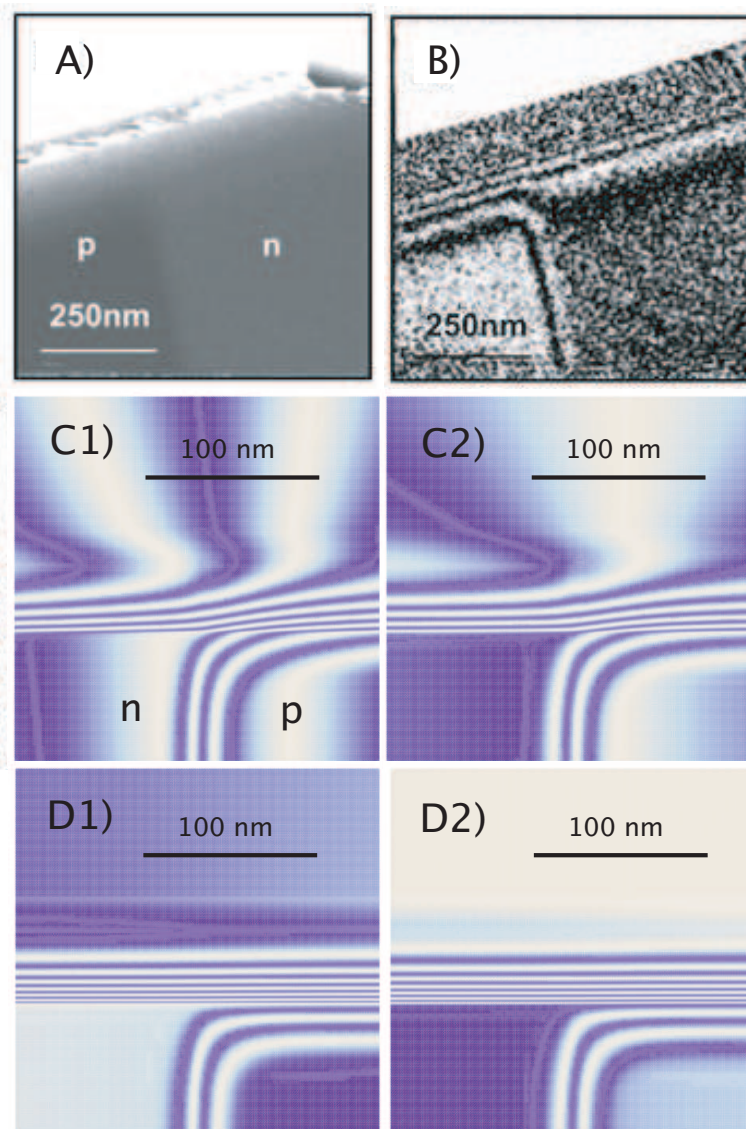


Fig. 3.12. A), B): Experimental images of a Sb-B symmetric doped p-n junction. The doping concentration is $4 \cdot 10^{18} e.c./cm^3$. The specimen thickness is $\sim 500nm$ plus $\sim 30nm$ of amorphous surface layers. A) A reconstructed phase image of the junction. B) Cosine of the phase (Contour map) revealing the presence of an “electrically altered” layer on the sample surface. It is very interesting to notice the strong phase wrapping on this “electrically altered” layer, which is modeled by a volume fixed charge due to the beam interaction (secondary electron emission) with the insulating layer of the specimen. The bulk is a semiconductor so that the excess charge can flow toward the contacts. C1), C2), D1), D2): Holography simulations of a Sb-B symmetric doped P-N junction using the CPAC model. The doping concentration is $4 \cdot 10^{18} e.c./cm^3$. The specimen thickness is $500nm$ plus $30nm$ of uniformly charged insulating layer. The uniform charge is $3.3 \cdot 10^{18}$ in C1) and C2) and $5 \cdot 10^{18}$ in D1) and D2). In C2) and D2) the perturbation on the reference wave is taken into account.

To take into account both the phase wrapping and the cancellation of the fringing field, it is sufficient to make the hypothesis that the electron beam charges

the surface layers. Indeed, the CPAC (sec. 3.2) simulations are made with a fixed volume charge of the amorphous surface layer (30 nm) (Fig. 3.12A), implemented in the numerical solver as an insulating material. It turns out that the phase wrapping can be interpreted by adopting this hypothesis, and also, the intensity of the fringing field is diminished by the increase of the oxide charge 3.12. The experimental contour map image (Fig. 3.12A) shows that the phase wrapping is extended under the amorphous layer towards the bulk, due to a layer of about 30 nm is present between the 30 nm amorphous layer and the bulk. It is possible to model the effect of this layer by imposing a fixed charge, but studying the specimen preparation mechanism and its effects is preferred in order to develop a more accurate model.

4. Electron Holography of a Metal-Oxide-Semiconductor specimen.

In this chapter, the behavior of Metal-oxide-semiconductor MOS specimen [45] observed by off-axis electron holography in a Philips CM200-ST FEG TEM is considered. The experimental images are interpreted by comparing them to simulated images obtained by elaboration of the 3D electrostatic potential computed by the commercial software ISE-TCAD tools Mesh and DESSIS. Such a software allows us to take into account all the specimen features such as geometry, dopant concentration, permittivity etc. and numerically solve the electrostatics problem inside the specimen and the surrounding vacuum by implementation of Poisson's equation (that becomes Laplace's equation in the vacuum) and continuity equations for electrons and holes (see also sec. 2.1.1). The transistor was prepared for observation using conventional 'trench' FIB milling in an FEI FIB 200 workstation [45]. Specimen preparation can avert the device from its ideal behavior and affect its electrical properties. In particular, focused ion beam (FIB) milling can modify the surfaces, resulting in physical damage and in ion implantation. It will be shown that this issue seems not to be as effective as in the case of the P-N junction (sec. 3.3.3). Indeed the hypothesis that the oxides are charged by the electron beam, is sufficient to interpret the experimental results.

4.1 Specimen description and experimental results

A bright-field image of the transistor is shown in Figure 4.1a for a specimen of nominal thickness of 400 nm. Off-axis electron holograms of this region were recorded at 200 kV using a Philips CM200-ST FEG TEM equipped with a Lorentz lens and an electron biprism. Figure 4.1b shows eight-times-amplified phase contours obtained from region '1' in Figure 4.1a. Surprisingly, elliptical contours are visible in each oxide region, and a fringing field is present outside the specimen edge. Both the elliptical contours and the fringing field are associated with the charging of the oxide as a result of secondary electron emission from the specimen during electron irradiation. Figure 4.1c shows a similar image obtained after coating the specimen on one side with 20 nm of carbon. The effects of charging are now either absent or present only inside, there is no fringing field outside the specimen edge, and the contours in the specimen follow the

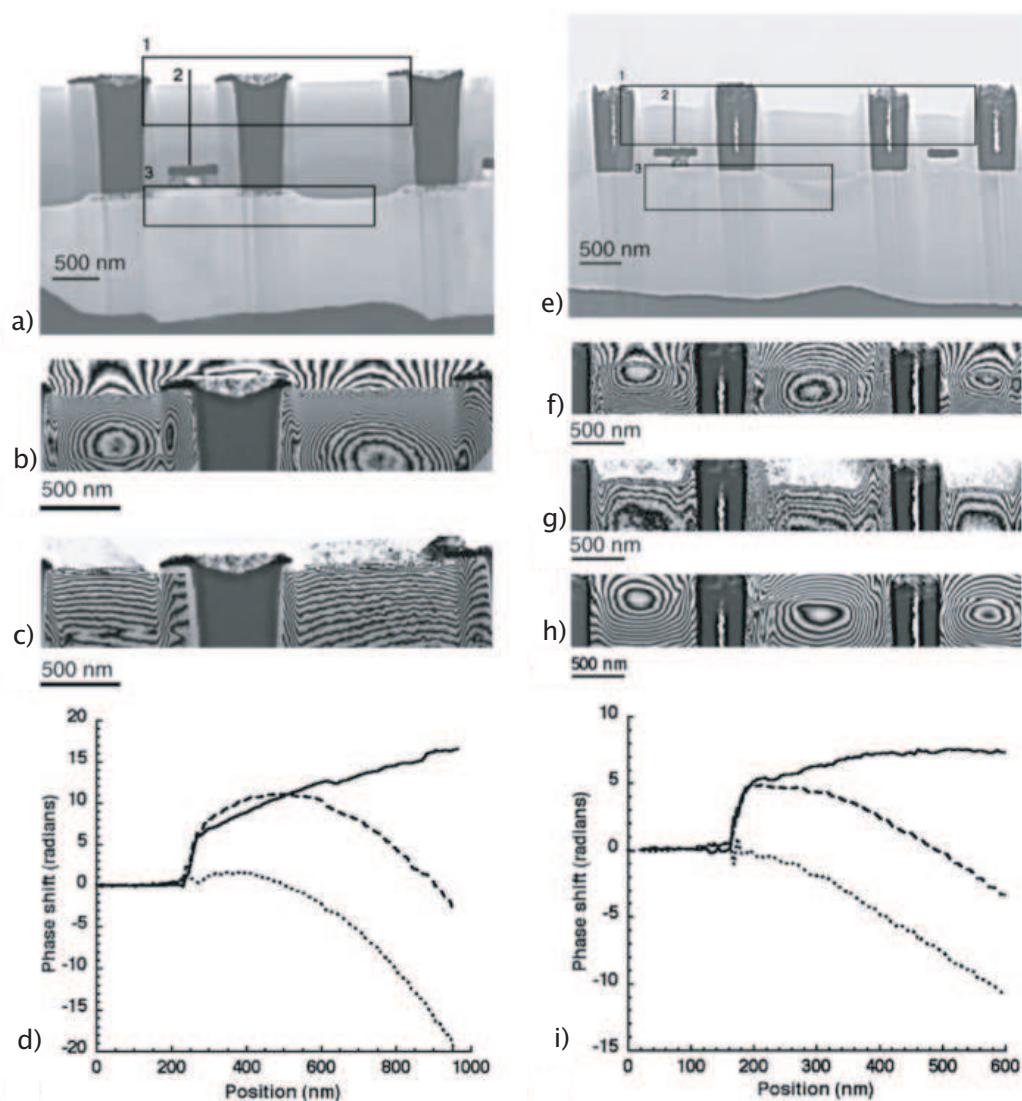


Fig. 4.1. Results obtained from the “trench” specimen of nominal thickness 400 nm (Left) and 150 nm (Right). (a,e) Bright-field TEM image of the PMOS transistors, indicating the locations of the regions analyzed in more detail in the subsequent figures. (b,f) Eight times amplified phase contours, calculated by combining phase images from several holograms obtained across the region marked “1” in (a) and in (e) for the 400 nm thick and the 150 nm thick specimen respectively. Specimen charging results in the presence of electrostatic fringing fields in the vacuum region outside the specimen edge, as well as elliptical phase contours within the Si oxide layers between the W contacts. (c) and (g) Show equivalent phase images obtained after coating the specimen on one side with approximately 20 nm of carbon to remove the effects of charging. The phase contours now follow the expected mean inner potential contribution to the phase shift in the oxide layers, and there is no electrostatic fringing field outside the specimen edge. (h) Shows the difference between phase images acquired before and after coating the specimen with carbon for the 150nm thick specimen, again in the form of eight times amplified phase contours: since there is no appreciable difference compared to (f), then the thickness can be considered constant. (d) Shows one-dimensional profiles obtained from the phase images in (b) and (c) along the line marked “2” in (a). Similarly, (i) Shows one-dimensional profiles obtained from phase images along the line marked “2” in (e). The dashed and solid lines were obtained before and after coating the specimen with carbon, respectively. The dotted line shows the difference between the solid and dashed lines.

change in specimen thickness in the oxide. Phase profiles were generated from the images used to form Figures 4.1b and 4.1c along line '2', and are shown in Figure 4.1d. The dashed and solid lines correspond to results obtained before and after coating the specimen with carbon, respectively, while the dotted line shows the difference between these lines. If the charge is assumed to be distributed throughout the thickness of the specimen, then the electric field in the oxide is 2×10^7 V/m [45], just below the breakdown electric field for thermal SiO₂ of 10^8 V/m, while numerical 3D simulations, that take into account the fringing field, give a slightly lower value of 1.5×10^7 V/m. The effect of specimen charging on the dopant potential in the source and drain regions of the transistors is just as significant. The phase gradient in Figure 1d continues into the Si substrate, and the dopant potential is always undetectable before carbon coating, whether or not a phase ramp is subtracted from the recorded images. Surprisingly, after FIB milling the specimen from the substrate side of the wafer ('back-side milling'), carbon coating is not required to prevent specimen charging, presumably because of the sputtering and subsequent redeposition of Si onto the oxide layers during milling.

4.2 Geometry and boundary conditions of the numerical model

The geometry of the model is shown in Fig. 4.2 The boundary conditions of DESSIS impose the Electric Field lying in the planes framing the simulation domain. Such planes are therefore reflection symmetry elements of the problem, and the simulation turns out to be equivalent to an infinite array of Si oxide trapezoids (or parallelepipeds in the constant thickness case) that alternate W silicide parallelepipeds, all on an infinite Si layer. The y and z dimensions are critical, and must be kept large enough to avoid the perturbation of the Electrostatic Field due to the mirror devices present on the score of the reflection symmetry. The z dimension in particular must include almost the entire Field, that must become negligible before the end of the domain. In fact the electron optical phase used for image simulations is obtained by integration of the Electrostatic potential along the z direction.

4.3 Interpretation of the experimental images

The experimental images are interpreted by comparing them to simulated images obtained by elaboration of the electrostatic potential computed by means of 3D numerical simulations. The integration of the electrostatic potential along z , the electron beam direction, gives, in the POA approximation (appendix A.1), the phase shift:

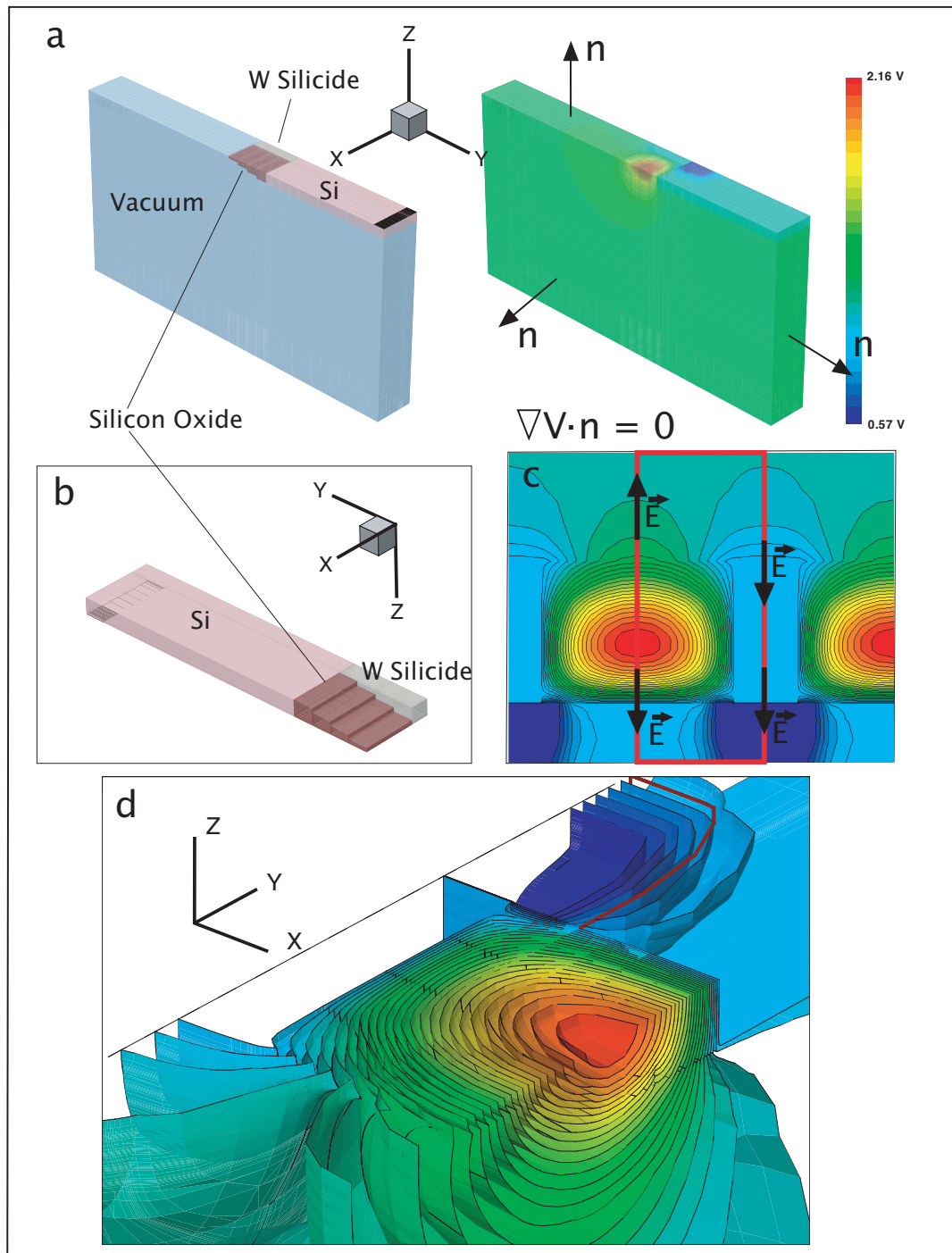


Fig. 4.2. Simulation geometry and boundary conditions. a: The whole simulation domain. On the left the geometry of the model is displayed, on the right the boundary conditions for the Electrostatic Potential computation: the equipotential surfaces are orthogonal to the boundaries (Eq.2.9). b: The trapezoidal shape of the Si oxide is modeled with a step shape. c: The effect of the boundary conditions: the domain boundaries are reflection symmetry planes so that an infinite array of MOS is modeled. d: An equipotential surface plot shows that the problem is intrinsically three-dimensional and the fringing field contribution is important especially under (and above) the specimen:

$$\phi(x, y) = C_E \int V(x, y, z) dz \quad (4.1)$$

where C_E is $7.3 \text{ rad } V^{-1} \mu\text{m}^{-1}$ for an electron beam of 200 keV , has been performed, as well as the image simulations in holography, by means of the software **Mathematica5.2** [43]. The hypothesis that the oxides are charged by the electron beam is useful for electric field simulations and image interpretation. It will be shown that the agreement with the experimental images is reached by making the assumption that the Silicon oxide is uniformly charged. This is implemented in simulations by imposing a fixed charge to be used as a fitting parameter. Then, according to the experimental procedure, the contour map (Eq. 1.16) images are computed with an eight time amplified phase.

4.3.1 Image simulations

The oxide is modeled as an insulator with a fixed uniform charge that must be fit by comparing simulations and experiments. Such a charge is positive as the main contribution to the beam-specimen interaction is the secondary electron emission. The mean inner potential, the specimen thickness and the distance of the perturbed reference wave from the edge can also be considered somehow as fitting parameters, even if we have an experimental estimate of them. Initially only a constant thickness model was used. Early holography simulations for the “trench” of nominal thickness 400 nm showed circular fringes as in experiments, but the center of such circles was always too close to the edge for any chosen values for the MIP, the distance of the reference wave and the oxide charge, (in a physical sensible range). Such is the case for the constant thickness simulations that models the thinner specimen (Fig. 4.3.1).

The variable thickness oxide of last simulations, acting as an electron prism, make the circle move down and gives a fringe pattern that is in better agreement to the experiments (Fig. 4.3.1).

Fig. 4.3.1 shows simulations of contour map images for the case of the “trench” specimen of nominal thickness 400 nm , but without taking into account the MIP or the perturbation of the reference wave, or both. These two parameters are necessary to fit the experiments. In any case the circular fringe pattern on the oxide is always present, generated by the uniform charge distribution induced by the electron beam. Such a pattern is due to the the strong external field produced by the charged oxide (Fig. 4.3.1)

The maximum value of the oxide electrostatic field obtained in **DESSIS** simulations is below the breakdown electric field for thermal SiO_2 of 10^8 V/m . Its value of $1.5 \times 10^7 \text{ V/m}$ is rather in agreement with the estimated value of 2×10^7 given in a previous work [45].

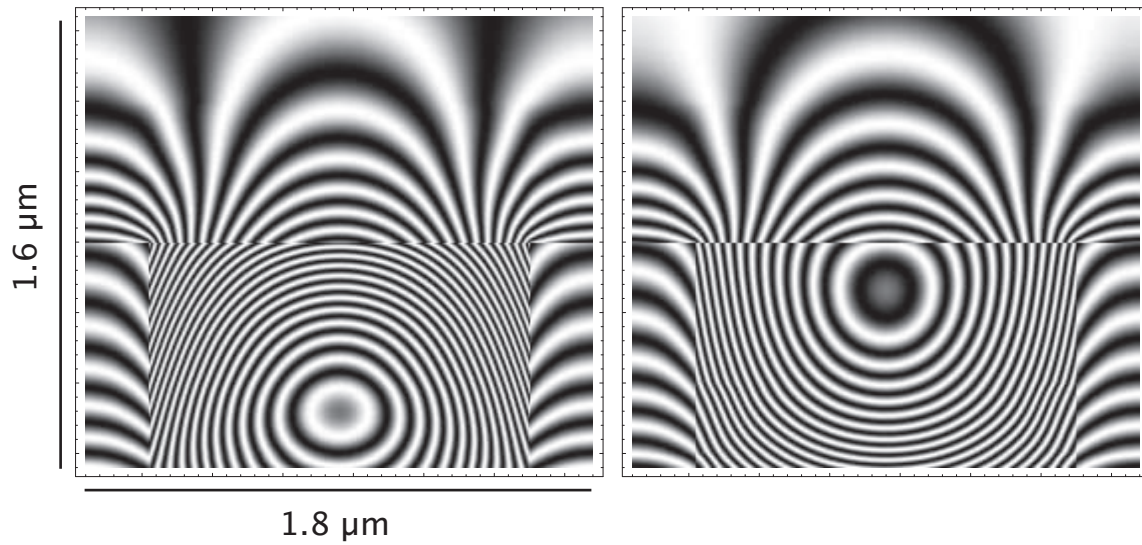


Fig. 4.3. Simulations of eight times amplified phase contours. Left: the image models the “trench” specimen of nominal thickness 400 nm. Right: the image models the specimen of nominal thickness 200 nm. Both simulations have been made by imposing a uniform oxide charge density of $5 \times 10^{15} e.c./cm^3$, a MIP of 10 V, and a distance of $2 \mu m$ from the reference wave.

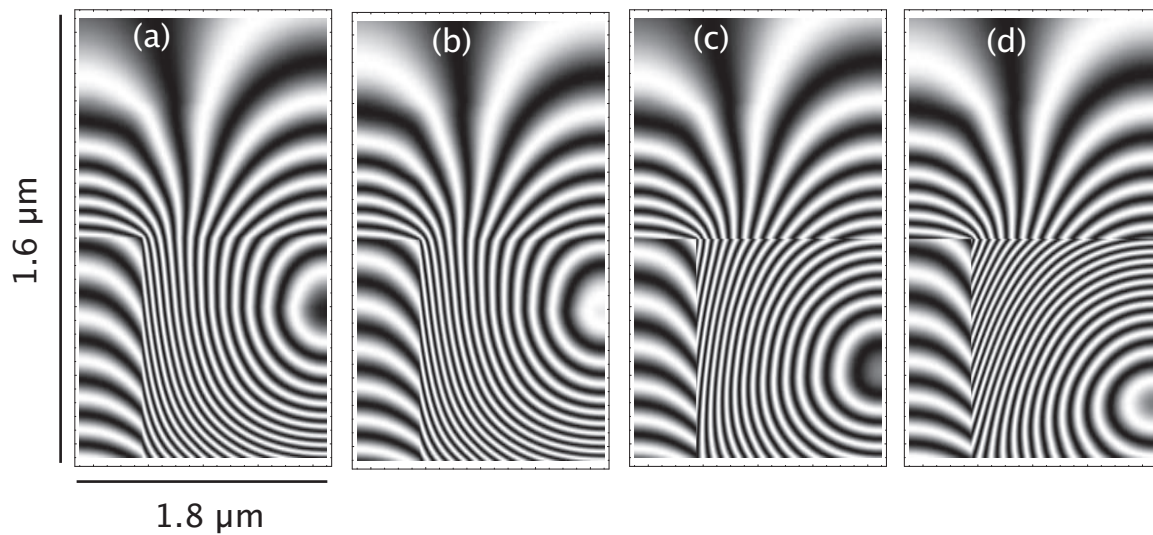


Fig. 4.4. Simulations of the “trench” specimen of nominal thickness 400 nm. (a): neither reference wave perturbation nor MIP are not taken into account. (b): the reference wave perturbation weakly changes the fringe pattern when the MIP is not considered. (c): MIP has been included in computations, but the absence of reference wave perturbation makes the fringe pattern different from (d), where both the MIP and the reference wave perturbation are taken into account.

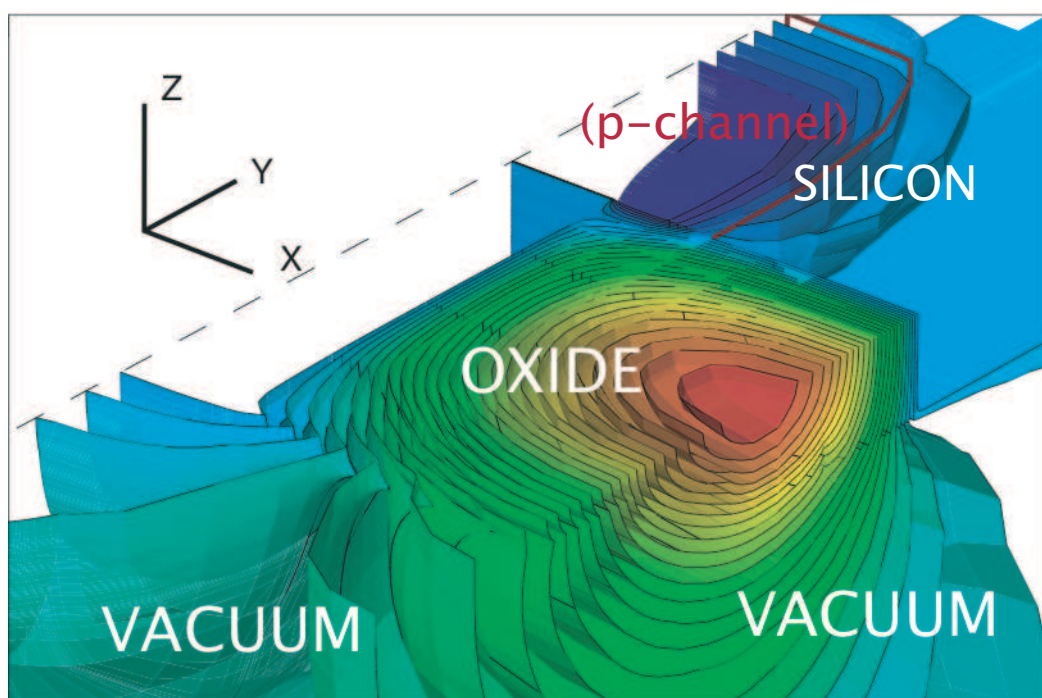


Fig. 4.5. The external field produced by the oxide charged under the effect of the electron beam, which is responsible for the circular fringes obtained in holography.

5. 3D field simulations of phase contrast images of field emitting CNTs.

In this chapter out-of-focus and contour map images of multi-walled carbon nanotubes (CNTs) will be presented and interpreted. CNTs are allotropes of carbon with a nanostructure that can have a length-to-diameter ratio as large as 28,000,000:1 [46], which is unequalled in any other material. These cylindrical carbon molecules have novel properties that make them potentially useful in nanotechnology, electronics, optics and other fields of material science, as well as in architectural fields. Here we are interested in their electrical properties, due to the peculiar geometry and to the good conductivity, that, for instance, make them good candidates as Field Emission Guns (FEGs). Full 3D numerical simulations are necessary in order to interpret the experiments, so that the computational resources of the machine used for DESSIS simulations have been fully exploited. However, the geometry of the problem together with the boundary conditions is of some help in reducing the number of nodes (sec.2.1). Indeed, only a quarter of the nanotube and of the surrounding vacuum is considered in computations (sec.5.3). It will be shown that the numerical simulations give the typical wings observed in out-of-focus experiments, and that such a fringe pattern is due to the strong increase of the slope of the polarization charge at the tip (tip effect [36]). These results can not be achieved by analytical approaches such as modeling the nanotube by charged conducting prolate spheroids (sec.5.2). A further advantage of the numerical approach is that it starts with the physical equations without introducing arbitrary boundary conditions and ad hoc hypotheses on the electric field and on the shape of the nanotubes. The interpretation of the experimental results is then free from any additional hypotheses.

5.1 Specimen description and experimental results

The off-axis electron holograms that are presented below were all acquired at an accelerating voltage of 300 *kV* using a Philips CM300ST field emission gun TEM equipped with a “Lorentz” lens, an electron biprism, a GatanTM imaging filter and a 2048 pixel charge-coupled-device (CCD) camera, at the Department of Materials Science and Metallurgy by the HREM group of the University of Cambridge. The holograms were acquired with the conventional microscope

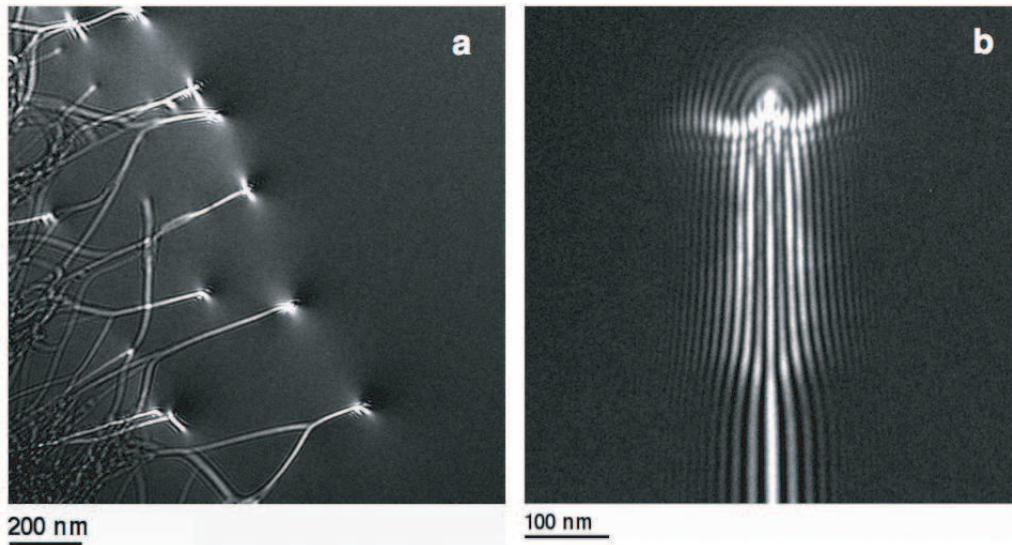


Fig. 5.1. a) Defocused bright-field image of a sample of bundles of single-walled carbon nanotubes, with a voltage applied between the tubes and a gold needle that was brought to within $1 \div 2 \mu\text{m}$ of them. b) Higher magnification defocused bright-field image of the end of an individual nanotube bundle.

objective lens switched off and the sample located in magnetic-field-free conditions. Reference holograms were used to remove distortions associated with the imaging and recording system of the microscope. A TEM specimen holder that allows samples to be nanopositioned and examined under an applied bias has been used as a way of applying a strong electric field in situ between the tubes and a gold electrode placed in front of them [47]. The nanopositioning specimen holder is useful in measuring the electrostatic fields at the ends of nanowires and nanotubes, with the aim of understanding the details of field emission on a nanometer scale. Figures 5.1 and 5.2 show preliminary results obtained from a sample containing bundles of single-walled carbon nanotubes. Defocused bright-field images (Fig. 5.1) show a diffraction pattern, similar to that formed by an electron biprism with variable fringe spacing. However, a very interesting feature of the out-of-focus images is the fringe pattern present at the top of the nanotube, as it provides significant information about electric field.

5.2 Linear charge analytical model

The simplest description of the electric field around field emitting microtips relies in modelling the tip and the anode by hyperboloid surfaces of revolution and obtaining the exact, full 3D solution in the prolate spheroidal coordinate system [48, 49, 50]. However, it is worthwhile to note that we obtain the same solution when a linear density charge distribution is assumed on a line segment of length $2a$ [51].

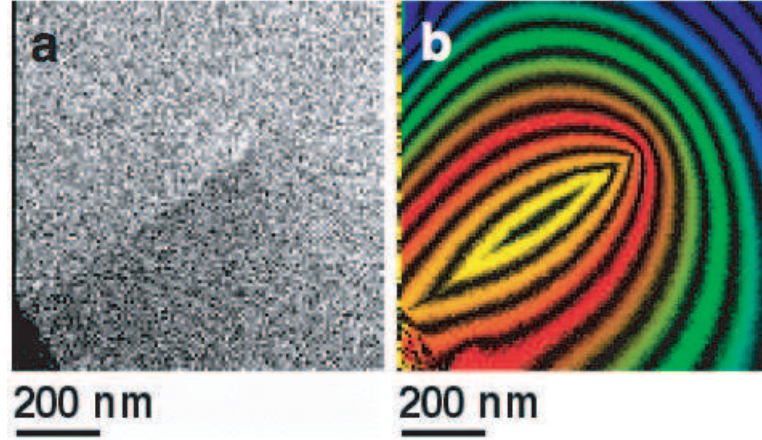


Fig. 5.2. a) Amplitude and b) contour phase images, respectively, obtained from an off-axis electron hologram of a carbon nanotube bundle that has a voltage applied to it in situ in the TEM.

In fact, if we integrate between 0 and a the following expression,

$$V(x, y) = C \int_0^a y_0 \left(\frac{1}{\sqrt{x^2 + (y - y_0)^2}} - \text{nonumber} \frac{1}{\sqrt{x^2 + (y + y_0)^2}} \right) dy_0 \quad (5.1)$$

we obtain the potential of a linearly increasing charge density apart from a constant C dependent on the unit system and on the amount of charge. Fig. 5.3 reports the trend of the potential distribution in the $z = 0$ plane.

$$V(x, y)/C = \sqrt{x^2 + (-a + y)^2} - \sqrt{x^2 + (a + y)^2} - y \log(-y + \sqrt{x^2 + y^2}) - \\ y \log(y + \sqrt{x^2 + y^2}) + y \log(a - y + \sqrt{x^2 + (-a + y)^2}) + \\ y \log(a + y + \sqrt{x^2 + (a + y)^2}) \quad (5.2)$$

If we add a linear term $-Ey$, corresponding to a constant electric field, the potential distribution changes as shown in Fig. 5.4, where the potential at 0 V is reported. It can be seen that the shape is that of a hyperboloid of revolution mimicking the tip shape.

As for the case of the constant phase density [52], it is now also possible to obtain the electron optical phase shift in closed analytical form. It is sufficient to integrate the phase shift associated with the two opposite unit charges at $\pm y_0$

$$-\log(x^2 + (y - y_0)^2) + \log(x^2 + (y + y_0)^2) \quad (5.3)$$

taking into account the linear trend of density charge. From

$$\varphi(x, y) = C_\varphi \int_0^a [-\log(x^2 + (y - y_0)^2) + \log(x^2 + (y + y_0)^2)] y_0 dy_0 \quad (5.4)$$

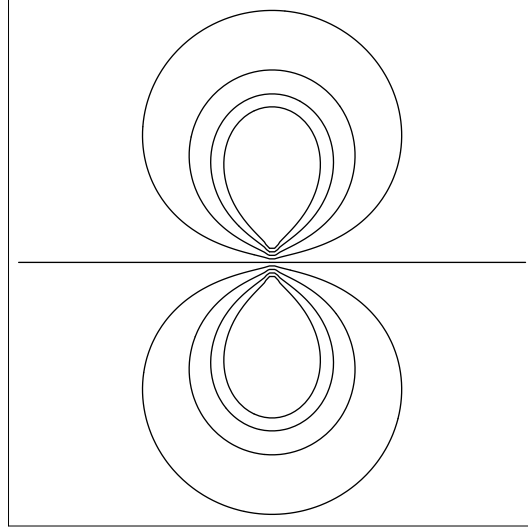


Fig. 5.3. Potential distribution around a linearly increasing charge density.

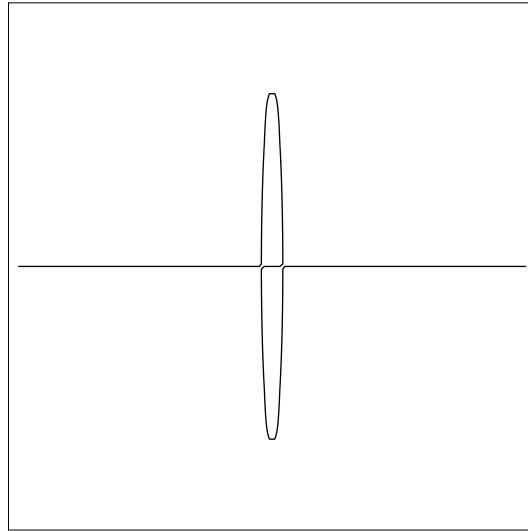


Fig. 5.4. Zero potential distribution around a linearly increasing charge density with a constant field added.

it turns out, apart from a multiplicative constant C_φ ,

$$\begin{aligned} \varphi(x, y) = C_\varphi & \left(4ay - 2ixy \log\left(\frac{-ia + x - iy}{x}\right) + 2ixy \log\left(\frac{ia + x - iy}{x}\right) - \right. \\ & \left. 2ixy \log\left(\frac{-ia + x + iy}{x}\right) + 2ixy \log\left(\frac{ia + x + iy}{x}\right) - \right. \\ & a^2 \log(a^2 + x^2 - 2ay + y^2) - x^2 \log(a^2 + x^2 - 2ay + y^2) + \\ & y^2 \log(a^2 + x^2 - 2ay + y^2) + a^2 \log(a^2 + x^2 + 2ay + y^2) + \\ & \left. x^2 \log(a^2 + x^2 + 2ay + y^2) - y^2 \log(a^2 + x^2 + 2ay + y^2) \right) \end{aligned} \quad (5.5)$$

If values for the various parameters are chosen in such a way as to fit the experimental data, we obtain the following image for the phase distribution around a nanotip (in black) that should be compared to the experimental one.

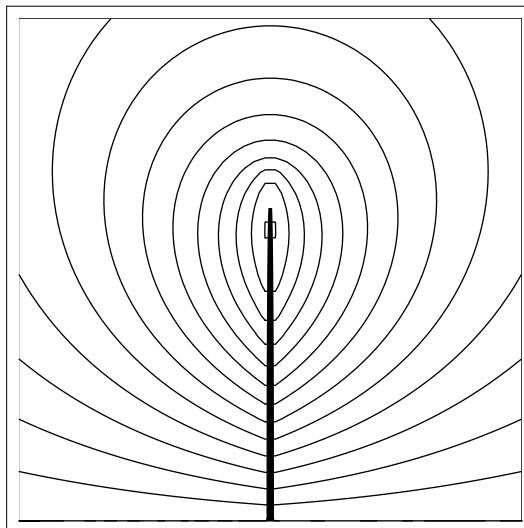


Fig. 5.5. Phase contour line around a nanotube (black).

Also the out-of-focus image can be calculated, and the result (Fig. 5.6)

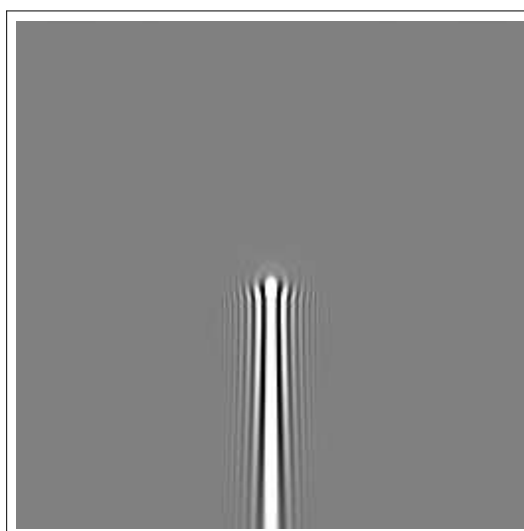


Fig. 5.6. Out-of-focus image of the phase associated to the nanotube.

shows both the predicted fringe spacing variation along the nanotube dependent on the linear increase of the charge density, and the lack of the wings at the top.

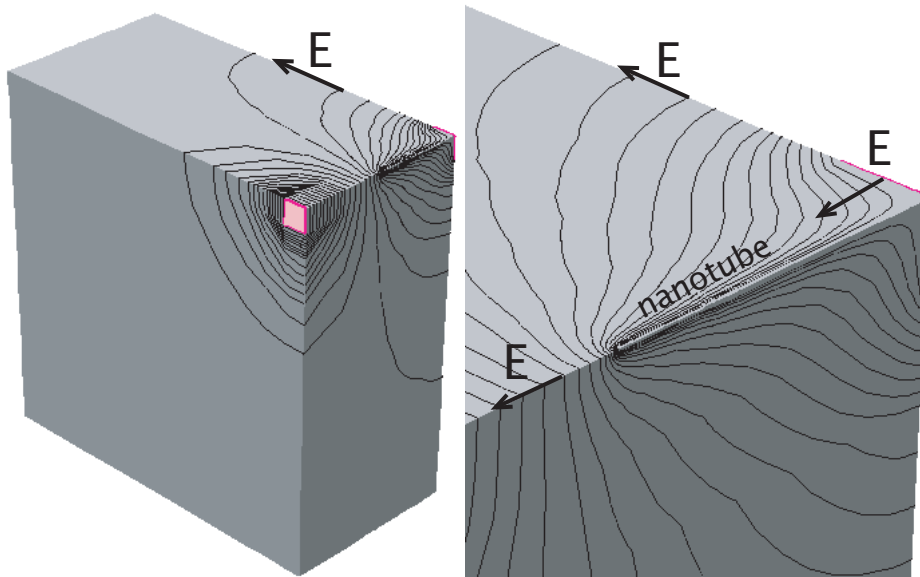


Fig. 5.7. Geometry of the model used in numerical device simulations of nanotubes. Equipotential lines are shown at the boundaries. The Electric Field is orthogonal to boundaries with contact (Von Neumann conditions) and parallel to boundaries in the other cases. These are all reflective conditions, which make boundaries as reflection symmetry planes. In this case the geometry of the nanotube allow us to exploit the boundary conditions in order to save computational resources. Indeed it is sufficient to simulate only a quarter of nanotube.

5.3 Numerical computation of the electrostatic potential

The geometry of the model is shown in Fig. 5.7. It exploits the boundary conditions of the ISE-tCad solver DESSIS to shrink the number of nodes by a factor 4. In fact the electrostatic potential is computed under the constraint that its gradient, the electric field, lies on the boundaries of the simulation domain (Reflective Von Neumann conditions, Eq. 2.9). Also in boundaries with contacts the conditions are reflective: in this case the electric field is naturally orthogonal to the boundaries. Therefore the simulation domain is bound by reflection planes. This, together with the fact that the simulation domain is a parallelepiped, makes it sufficient to simulate only a quarter of nanotube (Fig. 5.7). It must be noted that, though the problem is static as in the MOS case, the Poisson equation is not sufficient to model correctly the physics of the carriers at the interfaces between different materials. Therefore, if the catalyst is included in simulations, the problem must be implemented with fully coupled Poisson and continuity equations.

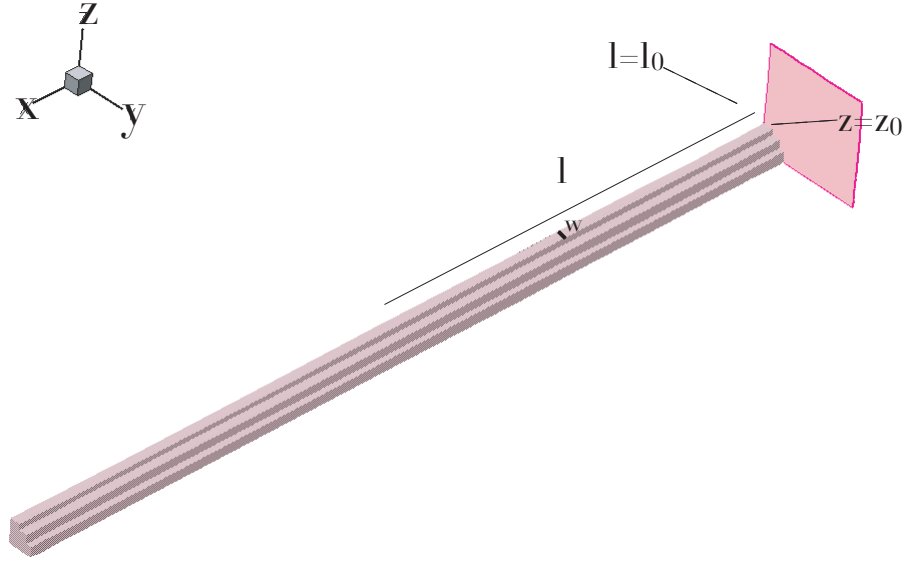


Fig. 5.8. Variables involved in the reduction from a surface to a line charge.

5.4 Charge density

The first step in setting up our model is to compare our computations with those carried out in sec. 5.2. An ISE-tCad simulation in the case of a conducting nanotube gives us a surface charge density, as the tube is of finite dimensions. We reduced such a surface charge to the equivalent line charge density, which allowed us to compare it to line charge distributions available in literature. The reduction to a linear charge density is performed by the integral:

$$\lambda(l) = R \epsilon_0 \partial_l \left(\int_{-|w/2-\eta|}^{w/2-\eta} \left(\int_{l_0}^l \partial_z V(x, y, z)|_{z=z_0} dx \right) dy \right), \quad (5.6)$$

derived from the Gauss' theorem of the electrostatics [36], where, see Fig(5.8), V is the Electrostatic potential, z_0 the coordinate of the lower side face of the nano tube, l_0 the coordinate of the base contact, l the length abscissa of the nanotube, w the width of the surface considered in this computation, η a small length to avoid the wedge discontinuity, ϵ_0 the vacuum permittivity and the factor $R = C/w$ is the ratio between the nanotube circumference C and w .

In numerical computations performed by DESSIS the charge is the result of the calculation of the Poisson and continuity equations, not an ad hoc function imposed as boundary condition.

In the simulations that we conducted there was always a linear increase of the charge along the nanotube, and a step increase of the charge at the end of it (Fig. 5.9). Such a feature, qualitatively consistent with the well known electrostatic tip effect, can be considered responsible for the “wing” pattern of

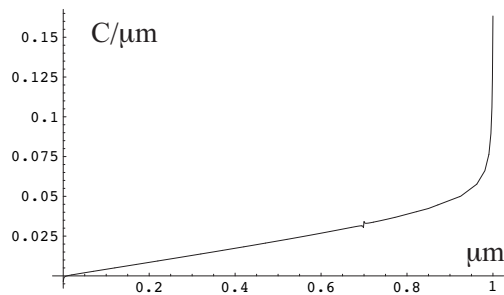


Fig. 5.9. Line charge distribution computed by the Eq.5.6 from a DESSIS simulation. The slope is linear over almost all the nanotube, except for the end of the tip where it increases strongly.

the Fresnel fringes, as analytical simulations performed on the hypothesis of a simply linear charge do not yield to this peculiar pattern (see fig. 5.6).

5.5 Image simulations

5.5.1 Holography

Our model for CNTs shows that the fringing field, and its influence on the reference wave, provides the most relevant contribution to the phase. This issue is rather obvious, as the specimen is so thin that in practice only the fringing field is present, but it is also very important as its intensity and its distribution strongly depends on the shape and the extension of the contacts. In this sense the 3D numerical computations are more valuable than the analytical ones, since we can choose contact dimensions and the problem is not affected by ad hoc hypotheses. Fig.5.10 shows the influence of the contact shape on the phase and the contour map images. It is interesting to notice that the phase (A1,B1) is completely different from the contour map (A2,B2), where the perturbation of the nanotube is evident. In fact the nanotube is strongly biased ($10 - 20 \text{ V}/\mu\text{m}$) and the linear ramp is the main contribution to the external field. However, the contour map is given by the cosine of the phase difference between the electron wave transmitted by the nanotube region, and the electron wave transmitted by a region where the only field ramp is present (sec.1.16). Therefore, in this case, the contour map has the property to cancel the linear ramp. This is an example where the perturbation on the reference wave is not a “perturbation” strictly speaking, but it helps in cancelling from the image the main contribution, which carries no information and hides the useful component of the field. When the contacts are wider (A) ($8\mu\text{m} \times 8\mu\text{m}$), the linear ramp contribution is stronger than when the contacts are narrower (B) ($8\mu\text{m}(x) \times 8\text{nm}(z)$). This is reflected on the phase and the contour map. In the case of wide contacts the phase contour-lines indicate that the field is almost linear (A1), while the contribution of the nanotube is no more negligible in the case of narrow contacts (B1). The linear ramp is canceled

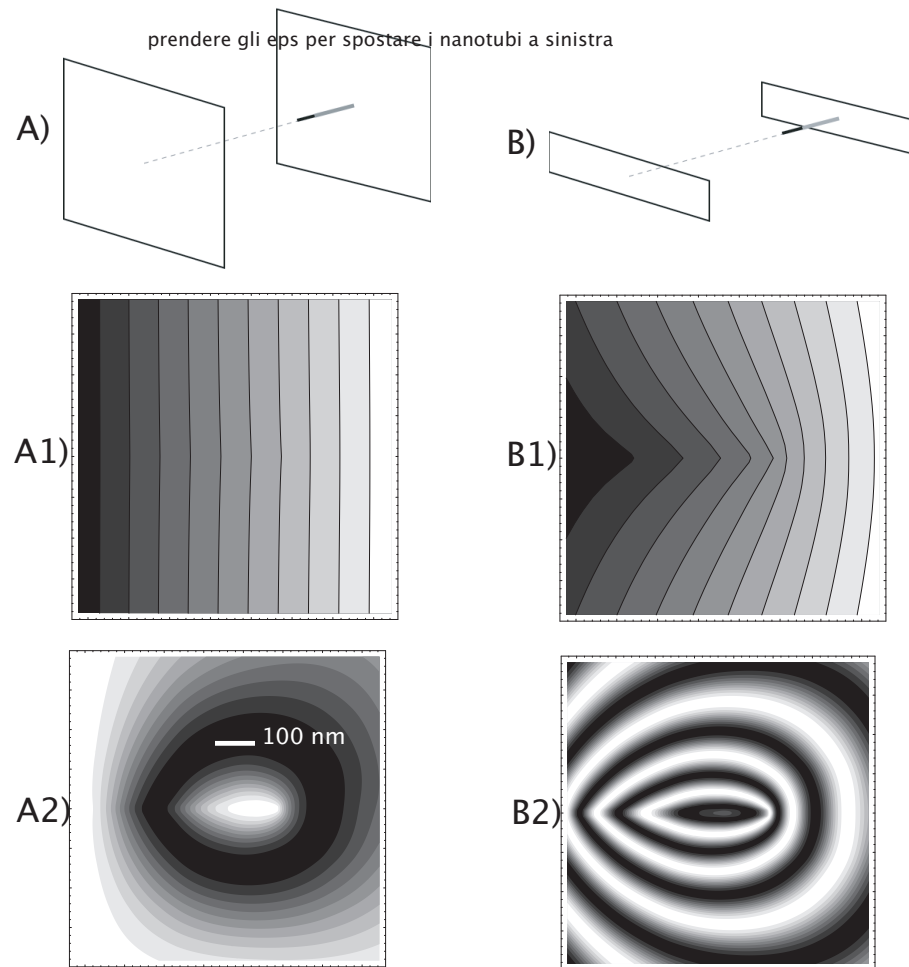


Fig. 5.10. Effect of the contact extent on the contour map. In A) the contacts are $8\mu \times 8\mu$ wide, while in B) the contacts are narrower in the z direction ($8\mu \times 8nm$): the bias is $10V/\mu m$ for both cases, but when the contacts are wider, the contribution of the CNT on the field is lower. In fact the nanotube contribution to the phase for the geometry A) is almost negligible (A1). In B1) the phase contour-lines for the geometry B) are shown. In A2 and B2 the respective contour map images, where for the narrow contact (B2) the fringe spacing is reduced.

in the contour map image simulations. Ovoidal fringes appear (A2) despite the fact that the phase does not show any significant structure (A1). The fringe spacing becomes smaller (B2) in the case of narrow contacts, indicating a more marked structure of the field around the nanotube.

The choice of the position of the reference wave also strongly influences the trend of the holographic fringes. Fig.5.11a) and b) shows contour map images under the same conditions, but with the reference wave in different positions. In a) the reference wave is taken in front of the nanotube, near the opposite biasing contact. In b) the reference wave is taken beside the nanotube, close to the contact connected to the nanotube. The shape of the fringes is noticeably different in the two cases; in a) the contours follow the nanotube geometry, while in b) the

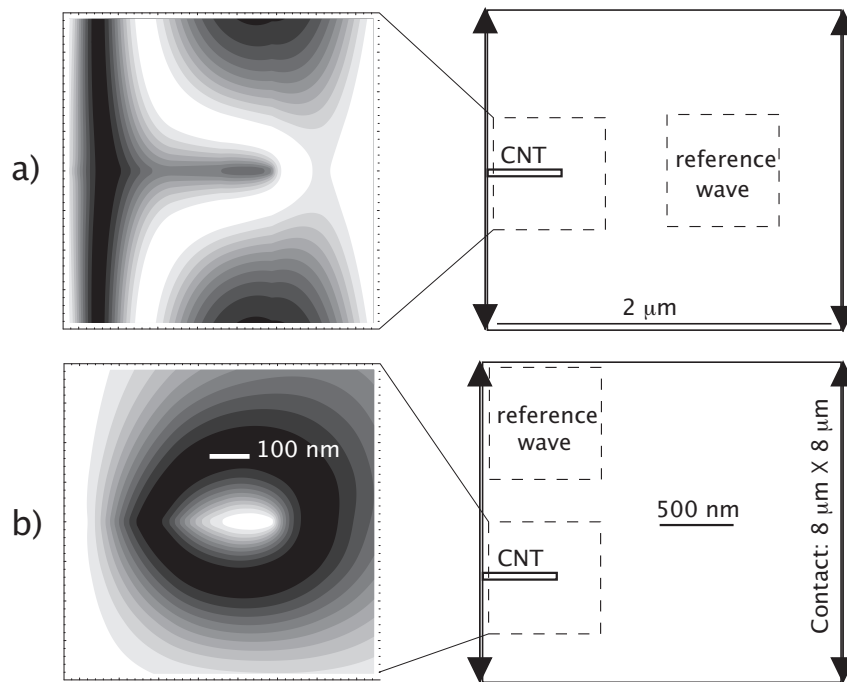


Fig. 5.11. Effect of the reference wave position on the contour map. a) b)

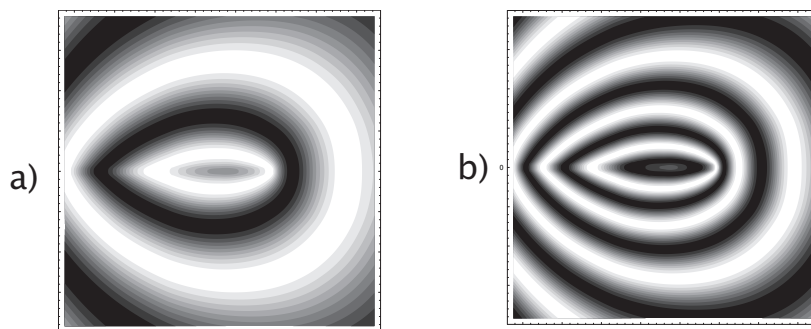


Fig. 5.12. Effect of the bias on the contour map. In a) the field is $10V/\mu m$, while in b) it is $20V/\mu m$

contours are ovoidal and centered on the tip. The position of the reference wave is yet another important fitting parameter, showing the importance of external field modelling.

The bias at the contacts influences the fringe spacing. Figure 5.12 shows that the fringes become denser when the potential difference at the contacts is increased.

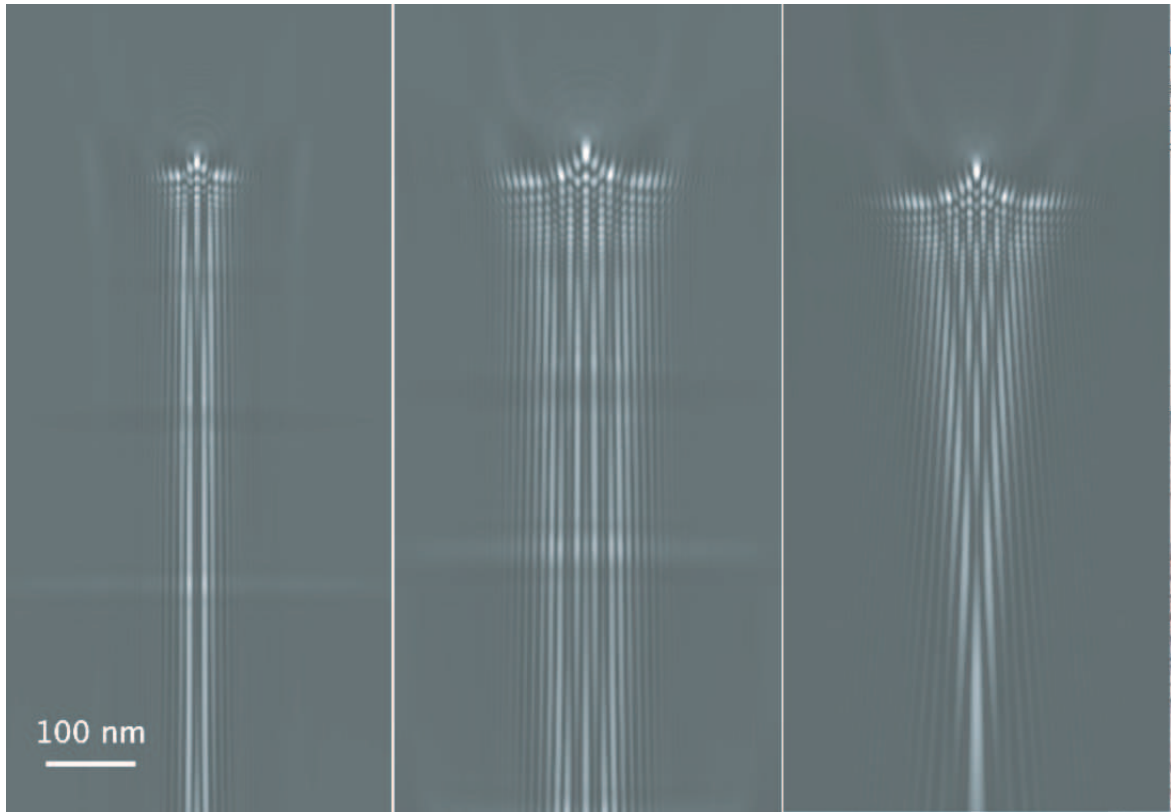


Fig. 5.13. The out-of-focus distance is increased from 0.2mm (Left) to 0.4mm (Center). When the contact area increases the parallel fringes become oblique (Right): the out-of-focus distance is always 0.4mm .

5.5.2 Out-of-focus

The out-of-focus images are less sensitive to the contact shape (Fig.5.13). The parallel fringes along the nanotube become oblique when the contact area increases (or better the ratio contact area/nanotube length). The peculiar trend of Fresnel fringes at the top of the nanotubes in the experimental images is obtained in simulations by a field of $200\text{V}/\mu\text{m}$ in a 1μ long and 15nm wide nanotube.

The effect of the MIP has also been taken into consideration (Fig.5.14). The only additional influence is that the out-of-focus distance must be increased, with respect to simulations of thinner multi-walled nanotubes where the MIP is less influent, in order to obtain again a fringe pattern similar to the experimental ones (Fig.5.14).

We have also tried to model the change in the fringe spacing at 300nm from the end of the nanotube (Fig.5.1), which we are still working on as we have not yet achieved a good fitting of the experimental images. We are investigating the effect of the presence of two different materials, the effect of thickness variation, and the perturbation of the contacts.

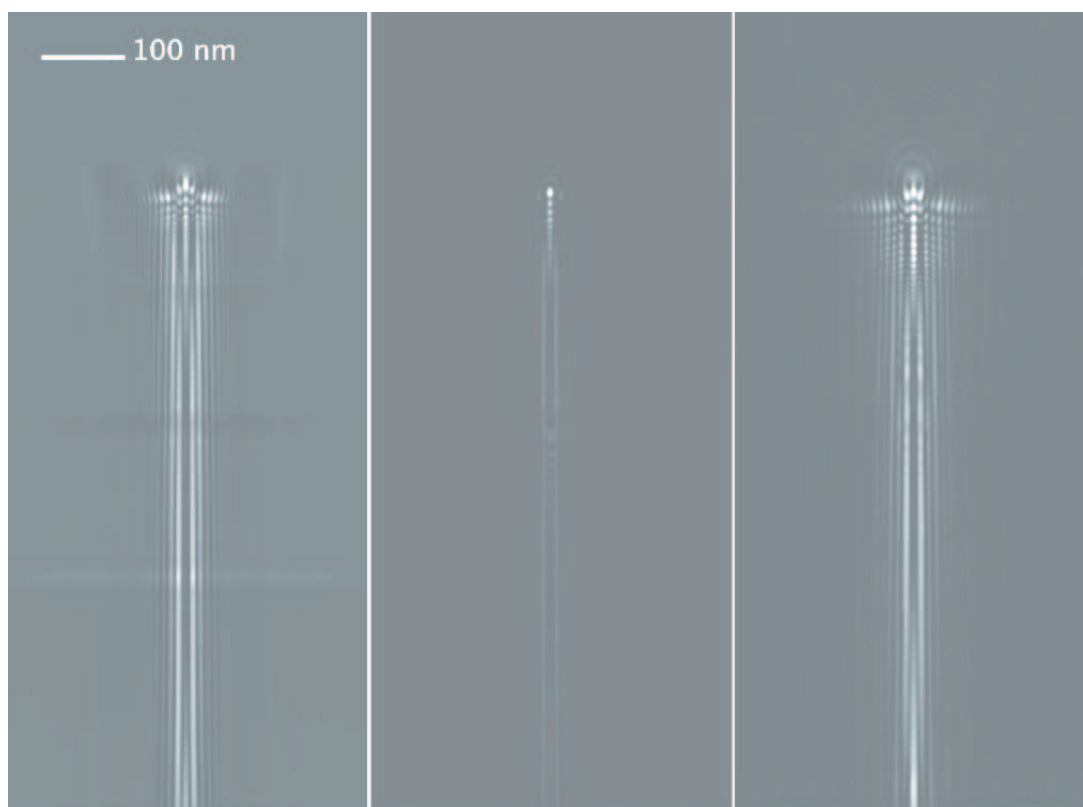


Fig. 5.14. The MIP becomes more influent in the out-of-focus images when the nanotube is thicker. Left: nanotube thickness is 15nm and out-of-focus distance is 0.2mm . Center: nanotube thickness is 45nm and out-of-focus distance is 0.2mm . Center: nanotube thickness is 45nm and out-of-focus distance is 0.4mm . However, the fringe pattern characterized by wings is recovered by increasing the out-of-focus distance.

Conclusions

The ever increasing improvements of the latest instruments allow the experimenters to obtain ever more detailed information from the images. The analytical models are no longer able to provide the interpretation of the experiments. Therefore, the development of more accurate models that take into account accurately the physics of the problem becomes necessary. In particular, it is fundamental to simulate the geometry of the specimen and its behaviour when it is observed in a TEM. The physical equations of semiconductors must be implemented together with hypotheses that take into account the effect of the electron beam, which is not a neutral probe but plays a relevant role in perturbing the ideal electrical behaviour of the sample. Indeed the electron beam has the effect of positively charging the sample because of secondary electron emission.

In this thesis it was shown that TEM experiments can be interpreted by means of suitable numerical methods that allow us to solve physical equations. It has been pointed out that in the case of three-dimensional problems a “normal” computer is not sufficient to provide precise and accurate computations. Therefore, parallel to increasing of performances of new instruments, it is necessary to increase the computing power for simulations.

Acknowledgments

I wish to thank Prof. Giulio Pozzi and Dr. Pier Francesco Fazzini for their generous and expert assistance in this work. Grateful thanks are also due to Dr. Rafal Dunin Borkowski, Dr. Takeshi Kasama and Dr. Marco Beleggia for their essential contribution and experience, and especially to Dr. Vittorio Morandi for the necessary support in setting up and managing the machine that made possible device simulations.

This work has been partially supported by FIRB funding, contract number RBAU01M97L.

A. Beam-specimen interaction

A.1 Phase object approximation

After describing the general function of the electronic microscope and the features of the specimens, it is necessary to observe how the investigation tool (probe) (the microscope's electron beam) interacts with the object investigated (electric field associated to the junction) and the microscope's optical components (lenses and possibly biprisms). The TEM working conditions and the features of the specimens allow us to establish three initial hypotheses for the theoretical analysis of the interaction:

- The electrostatic potential V of the junction and/or biprism may be considered a slight disturbance to the kinetic energy E_k of the incident electrons; thus, to a first approximation, the energy of the impinging beam is equal to the beam transmitted.
- Since the specimen is thinned, the absorbing/stopping effect and the wide-angle deflection of the electrons can be neglected. (As the absorption can be considered uniform and the high angle scattered electrons are intercepted by diaphragms, the specimen can be described as a phase object.)
- The magnetic specimens are not taken into consideration because the study is mainly focused on the p-n junctions. The only magnetic fields present in the experiments are the lenses which simply form the image.

Taking into account these approximations, interactions are described as elastic scattering of electrons by the potential V . According to the wave treatment, each electron of the impinging beam is drawn by a wave function which satisfies the Schrödinger equation not perturbed by the potential V (electron propagating in the empty space); the wave that propagates along the z axis is of the following type:

$$\Psi^0(z) = \exp(ikz) \tag{A.1}$$

where k is the wave vector [53]:

$$k = \frac{2\pi}{\lambda} = \frac{2\pi}{h} \sqrt{2m_0|e|U \left(1 + \frac{|e|U}{2m_0c^2}\right)} \quad (\text{A.2})$$

where λ is the electron wavelength, h is the Planck constant, m_0 is the electron rest mass, c is the speed of light, and U the electron accelerating potential. The equation (A.2) is relativistically corrected. The problem can be solved by solving the Schrödinger equation:

$$\left[\frac{1}{2m} \left(\frac{\hbar}{i} \nabla_{\mathbf{r}} + e\mathbf{A}(\mathbf{r}, z) \right)^2 - |e|\mathcal{V}(\mathbf{r}, z) \right] \Psi = 0\Psi \quad (\text{A.3})$$

where \mathbf{A} and \mathcal{V} are the electromagnetic potentials, $\mathbf{r} = (x, y)$ the vector lying on the plane orthogonal to the optical axis z and Ψ the wave function. The potential is given by:

$$\mathcal{V} = U + V \quad (\text{A.4})$$

where U and V are the accelerating potential and the specimen potential. The arbitrary constant in the energy is chosen in order to have zero for the value of the mechanical energy. Let us chose $\mathbf{A} = 0$, and let focus our attention on the electrostatic field. The electron wave outgoing from the specimen (or from the biprism) can be determined by solving the Schrödinger equation, perturbed by the potential V :

$$\nabla_{\mathbf{r}}^2 \Psi = -\frac{2m|e|}{\hbar^2} \mathcal{V}(\mathbf{r}, z) \Psi \quad (\text{A.5})$$

where $m = m_0(1 + eU/m_0c^2)$ is the electron mass relativistically corrected [53]. On the ground of the hypothesis ($E_k \gg V$) it is possible to write the solution of the equation A.5 in the form [54]:

$$\Psi(\mathbf{r}, z) = \exp(ikz)T(\mathbf{r}, z) \quad (\text{A.6})$$

Since the kinetic energy of the electrons is $E_k = \frac{\hbar^2 k^2}{2m}$, with k always computed by means of the equation (A.2), the condition $E_k \gg V$, which means that $E_k \simeq -U$, implies that V must slowly vary on a distance equal to the wavelength λ . Since the function $T(z)$ stands for the the perturbation on the impinging wave due to V , it must have the same property. By replacing the equation (A.6) in the equation (A.5), it turns out:

$$\nabla^2 T(\mathbf{r}, z) + 2ik \frac{\partial}{\partial z} T(\mathbf{r}, z) = -\frac{2m|e|}{\hbar^2} V(\mathbf{r}, z) T(\mathbf{r}, z) \quad (\text{A.7})$$

The equation (A.7) is solvable if the high energy approximation is adopted. Since the $T(\mathbf{r}, z)$ variation is slow with respect to λ , the term $\frac{\partial}{\partial z} T(\mathbf{r}, z)$ is dominant with respect to $\nabla^2 T(\mathbf{r}, z)$, and so this last term can be neglected. In this case the equation (A.7) becomes:

$$\frac{\partial}{\partial z} T(\mathbf{r}, z) = \frac{im}{\hbar^2 k} V(\mathbf{r}, z) T(\mathbf{r}, z) = \frac{i\pi}{\lambda E_k} V(\mathbf{r}, z) T(\mathbf{r}, z). \quad (\text{A.8})$$

On the ground of the second hypothesis back-scattering effects can be neglected. Therefore the boundary condition $T(-\infty) = 1$ can be imposed. It turns out:

$$T(\mathbf{r}, z) = \exp \left\{ -\frac{i\pi}{\lambda E} \int_{-\infty}^z V(\mathbf{r}, z) dz \right\} \quad (\text{A.9})$$

and

$$\Psi(\mathbf{r}, z) = \exp \left\{ ikz - \frac{i\pi}{\lambda E} \int_{-\infty}^z V(\mathbf{r}, z) dz \right\} \quad (\text{A.10})$$

It can be noted (Eq. A.10) that the transmission function $T(\mathbf{r}, z)$ only act on the phase of the impinging wave: the junction potential modifies the phase of the electron wave. Therefore, in electron microscopy, $V(\mathbf{r}, z)$ is considered a phase object, while $T(\mathbf{r}, z)$ is called object transmission function. The transmitted wave propagates beyond the specimen and is perturbed by the fringing field. In general, the total effect of $T(\mathbf{r}, z)$ is considered as due to the only specimen plane, and the propagation after the specimen is considered as free propagation. In in this case equation (A.9) simplifies in:

$$T(\mathbf{r}, z) = A(\mathbf{r}) \exp \left\{ -\frac{i\pi}{\lambda E} \int_{-\infty}^{\infty} V(\mathbf{r}, z) dz \right\}, \quad (\text{A.11})$$

where the amplitude factor $A(\mathbf{r})$ has been added to take into account the fact that electrons can either be stopped by a thick specimen or scattered by the specimen atoms at large angles and subsequently intercepted by the microscope apertures. The term

$$\phi(\mathbf{r}) = \frac{\pi}{\lambda E} \int_{-\infty}^{\infty} V(\mathbf{r}, z) dz \quad (\text{A.12})$$

corresponds to the phase shift between the impinging and the transmitted wave.

A.1.1 The Möllenstedt-Düker biprism

A TEM equipped with a Möllenstedt-Düker biprism makes “off-axis” electron holography and interferometry observations possible. The biprism consists of a biased conducting wire, placed between two conducting plates at 0V, replacing one of the selected-area apertures.

Let us consider the electrostatic potential generated from an infinite wire of density charge σ , lying on the y direction, placed between two infinite conducting plates of equation $x = a - b$, $x = -b$ [51]:

$$V_B(x, z) = -\frac{\sigma}{2\pi\epsilon_0} \ln \left\{ \frac{\cosh \left[\frac{\pi z}{a} \right] - \cos \left[\frac{\pi(x-b)}{a} \right]}{\cosh \left[\frac{\pi z}{a} \right] - \cos \left[\frac{\pi(x+b)}{a} \right]} \right\} \quad (\text{A.13})$$

where σ , the linear density charge of the wire, is given by

$$\sigma = -\pi\epsilon_0 V_W \left[\ln \left\{ \frac{\frac{\pi r_0}{2a}}{\sin\left(\frac{\pi b}{a}\right)} \right\} \right]^{-1}, \quad (\text{A.14})$$

r_0 and V_W are the radius and the potential of the wire respectively. By introducing (A.13) in (A.12), the phase shift results linear in x , the distance from the wire on the biprism plane, so that the biprism behavior as it is known in light optics is confirmed:

$$\phi(x) = \begin{cases} \frac{\pi}{\lambda U \epsilon_0} \frac{\sigma}{\epsilon_0} x(a-b)/a ; & \text{per } 0 \leq x \leq b \\ \frac{\pi}{\lambda U \epsilon_0} \frac{\sigma}{\epsilon_0} (a-x)b/a ; & \text{per } b \leq x \leq a \end{cases} \quad (\text{A.15})$$

If the plates are symmetric with respect to the wire, the transmission function becomes:

$$T_b(x, y) = \begin{cases} \exp\{ik\alpha|x|\} ; & \text{per } |x| > r_b \\ 0 ; & \text{per } |x| < r_b \end{cases} \quad (\text{A.16})$$

where $k = \frac{2\pi}{\lambda}$, and $\alpha = \frac{\sigma}{4U\epsilon_0}$ is the deflection angle between the incoming and outgoing asymptotic trajectories.

Acronyms

2D	<i>2 (two) Dimensional</i>
3D	<i>3 (three) Dimensional</i>
CCD	<i>Charge Coupled Device</i>
CPAC	<i>Cut Paste Analytical Computation</i>
CNT	<i>Carbon Nano Tube</i>
CPU	<i>Central Processing Unit</i>
e-h	<i>electron hole (pair)</i>
FEG	<i>Field Emission Gun</i>
FFT	<i>Fast Fourier Transform</i>
FIB	<i>Focused Ion Beam</i>
GUI	<i>Graphic User Interface</i>
ISE	<i>Integrated System Engineering</i>
ITRS	<i>International Technology Roadmap of Semiconductors</i>
K-F	<i>Kirchhoff Fresnel (integral)</i>
HREM	<i>High Resolution Electron Microscopy</i>
MIP	<i>Mean Innner Potential</i>
MOS	<i>Metal Oxide Semiconductor (device)</i>
p-n	<i>positive negative (junction)</i>
POA	<i>Phase Object Approximation</i>
SIA	<i>Semiconductor Industry Association</i>
tCAD	<i>technological Computer Aided Design</i>
TEM	<i>Trasmission Electron Microscope</i>

Bibliography

- [1] M. Beleggia, P.F. Fazzini, P.G. Merli, and G. Pozzi. *Phys. Rev. B*, 67:045328, 2003.
- [2] J. W. Goodman. *Introduction to Fourier Optics*. McGraw Hill, 1968.
- [3] P. F. Fazzini, P. G. Merli, and G. Pozzi. *Ultramicroscopy*, 99, 2004.
- [4] G. Pozzi and G.F. Missiroli. *J. Microsc.*, 18:103, 1973.
- [5] S. Martelli, G. Matteucci, and M. Antisari. *Phys. Stat. Sol.*, 49, 1978.
- [6] M.A. Schofield, M. Beleggia, Y. Zhu, and G. Pozzi. *Ultramicroscopy*, 108, 2008.
- [7] P.G. Merli, G.F. Missiroli, and G. Pozzi. *Journal de Microscopie*, 21:11, 1974.
- [8] P. F. Fazzini, P. G. Merli, G. Pozzi, and F. Ubaldi. *Physical Review B*, 2005.
- [9] P. F. Fazzini, L. Ortolani, G. Pozzi, and F. Ubaldi. *Ultramicroscopy*, 106, 2006.
- [10] W. Glaser. *Grundlagen Der Elektronenoptik*. Springer Verlag, Vienna and Berlin, 1952.
- [11] M. Born and E. Wolf. *Principles of Optics*. Pergamon Press, 1989.
- [12] G. Pozzi. *Optik*, 42:97, 1975.
- [13] G. Pozzi. *Optik*, 56:2423, 1980.
- [14] G.V Spivak, G.V. Saporin, N.N. Sedov, and L.F. Komolova. *Bull. Acad. Sci. USSR: Ser. Phys. (USA)*, 32:1046, 1968.
- [15] A. Tonomura. *Electron Holography*. Springer, Berlin, 1993.
- [16] R.P. Ferrier. In R. Barer and V. E. Cosslett, editors, *Advances in Optical and Electron Microscopy*, volume 3, pages 155–217. Academic Press, New York, 1969.

-
- [17] L. Reimer and H. Kappert. *Z. Angew. Phys.*, 27(3):165, 1969.
- [18] L.M. Reimer. *Transmission Electron Microscopy: Physics of Image Formation and Microanalysis*. Springer-Verlag, 1984.
- [19] G.F. Missiroli, G. Pozzi, and U. Valdrè. *J. Phys. E: Sci. Instrum.*, (14):649, 1981.
- [20] G. Pozzi. *Advanc. Imag. Electron. Phys.*, 93:173, 1995.
- [21] P.M. Voyles and et a. *Nature*, (416):826, 2002.
- [22] P.M. Voyles, J.L. Grazul, and D.A. Muller. *Ultramicroscopy*, 96:251, 2003.
- [23] C. Capiluppi, P.G. Merli, and G. Pozzi. *Optik*, 51:39, 1978.
- [24] G. Pozzi. *Optik*, 53:381, 1979.
- [25] M. Vanzi. *Optik*, 68:319, 1980.
- [26] C. Capiluppi, A. Migliori, and G. Pozzi. *Microsc. Microanal. Microstruct.*, 6:647, 1995.
- [27] M. Beleggia, P.F. Fazzini, and G. Pozzi. *Ultramicroscopy*, 96:93, 2003.
- [28] M. Beleggia, D. Cristofori, P. G. Merli, and G. Pozzi. *Micron*, 31:231, 2000.
- [29] A.S. Grove. *Physics and technology of semiconductor devices*. Wiley: New York, 1967.
- [30] M. Beleggia, R. Capelli, and G. Pozzi. *Phil. Mag. B*, 80:1071, 2000.
- [31] P.F. Fazzini. "Osservazione al TEM e simulazione numerica di giunzioni p-n polarizzate inversamente". Dipartimento di Fisica A. Righi, Università di Bologna: tesi di laurea, dicembre 2000.
- [32] J.S. Blakemore. *Semiconductor statistics*. Pergamon Press, 1962.
- [33] K.W. Boer. *Survey of Semiconductor Physics*. Van Nostrand Reinhold, 1990.
- [34] K. Seeger. *Semiconductor physics*. Springer, 1999.
- [35] W.Fichtner R.E.Bank, D.J.Rose. *IEEE Trans.Elec.Dev.*, 30(9):1031, 1983.
- [36] J.D. Jackson. *Classical Electrodynamics*., Prentice Hall, Englewood Cliffs, 1968.
- [37] *ISE Part 11: DESSIS*.
- [38] Ise-tcad release 8.0 manuals. PDF Document.

-
- [39] M.A. Gribelyuk, M.R. McCartney, J. Li, C.S. Murthy, P. Ronsheim, B. Doris, J.S. McMurray, S. Hedge, and D.J. Smith. *Phys.Rev.Lett.*, 89:025502–1, 2002.
- [40] J.N. Chapman. *J. Phys. D*, 17:623, 1984.
- [41] G. Missiroli, M. Matteucci and G. Pozzi. *Adv. Imaging Electron Phys.*, 99:171, 1997.
- [42] Athena, process simulation framework. web-site.
- [43] Mathematica 5.2. Wolfram Research Inc., 2005.
- [44] S. Rubanov and P. R. Munroe. Fib-induced damage in silicon. *Journal of Microscopy*, 214, June 2004.
- [45] R.E. Dunin-Borkowski, S.B. Newcomb, T. Kasama, M.R. McCartney, M. Weyland, and P.A. Midgley. *Ultramicroscopy*, (103):67–81, 2005.
- [46] L.X. Zheng and et a. *Nature Materials*, 3:673, 2004.
- [47] T. Kasama, Y. Antypas, R.K.K. Chong, and R.E. Dunin-Borkowski. In *Mater. Res. Soc. Symp. Proc.*, volume 51, 2005.
- [48] J.D. Nordgard. *J. Appl. Phys.*, 48(7), 1977.
- [49] J.D. Zuber and et a. *J. Appl. Phys.*, 91(11), 2002.
- [50] D.G. Walker and et a. *J. Vac. Sci. Technol. B*, 48(3), 2004.
- [51] E. Durand. *Electrostatique*. Masson, 1964.
- [52] G.F. Missiroli, M. Muccini, and G. Pozzi. In *Atti del XVIII Congresso di Microscopia Elettronica.*, number 2, 1991.
- [53] P.W. Hawkes and E. Kasper. *Principles of electron optics*, volume 3. Academic Press, 1994.
- [54] R.J. Glauber. In W.E. Brittin and L.G. Dunham, editors, *Lectures in Theoretical Physics*, pages 315–414. Interscience, 1959.